

**A Novel Lab-on-chip System for
Counting Particles/Cells Based on
Electrokinetically-induced Pressure-
driven Flow and Dual-wavelength
Fluorescent Detection**

by

Hai Jiang

A thesis

presented to the University of Waterloo

in fulfillment of the

thesis requirement for the degree of

Doctor of Philosophy

in

Mechanical Engineering

Waterloo, Ontario, Canada, 2013

©Hai Jiang 2013

AUTHOR'S DECLARATION

I hereby declare that I am the sole author of this thesis. This is a true copy of the thesis, including any required final revisions, as accepted by my examiners.

I understand that my thesis may be made electronically available to the public.

Abstract

For the past two decades, flow cytometry has been widely used as a powerful analysis tool for the diagnosis of many diseases due to its ability to count, characterize and sort cells. However, conventional flow cytometers are often bulky, expensive and complicated because sophisticated fluidic, electronic and optical systems are required to realize the functions of flow cytometry. The high cost and the complexity in operation and maintenance associated with flow cytometers as well as the large size have limited its use. In recent years, the rapid development of microfluidics-based lab-on-a-chip technology has created a new pathway for flow cytometry. Microfluidic devices allow for the integration of multiple liquid handling processes required in the diagnostic assays, such as pumping, metering, sampling, dispensing, sequential loading and washing. These lab-on-a-chip solutions have been recognized as an opportunity to bring portable, accurate and sensitive diagnostic tests to the flow cytometry.

However, most current microfluidic flow cytometry devices are micro- only in the microfluidic chip, the rest of most apparatuses are still large and costly, usually involving tubes, microscopes, lasers and mechanical pumps. Therefore, the objective of this study is to develop a novel lab-on-a-chip system based on the electrokinetically-induced pressure-driven flow and dual-wavelength fluorescent detection, which lights a promising pathway for making a real portable, compact, low-cost microfluidic flow cytometry device. In this study, the core of this microfluidic system is the custom-designed PDMS (polydimethylsiloxane) microchip. A novel method was applied to generate the electrokinetically-induced pressure-driven flow in a T-shaped microchannel using parameters settings that had been optimized by numerical study. This method combined both the electrokinetic pumping force and the pressure pumping force to eliminate their shortcomings associated with the use of each force alone. This is the fundamental of my study. By using this microchip, the size of the fluidic control subsystem is reduced significantly. Furthermore, the dual-wavelength fluorescent detection strategy is proposed in this thesis. On the optical detection side, excitation lights of two different wavelengths are provided by a single LED (light-emitting diode) from one side of the microchannel. Then the two emission lights are captured individually by two photo-detectors placed on the top and the bottom of the microchip. Compared with other microfluidic detection devices reported in the literatures that use lasers or PMTs (Photomultiplier tubes), this design allows for a significant reduction of 90% in the volume and cost. As another important part of my thesis research, a novel flow focusing method that allows the hydrodynamic focusing in a T-shaped microchannel with two

sheath flows is developed. This method solves the biggest obstacle which exists in current microfluidic flow cytometry devices. In this method, no external pumps, valves and tubing are involved in the system.

Although substantial progress has been made in current microfluidic flow cytometry, there is still a need for a low-cost, compact, portable microfluidic devices, especially in low-resource settings as well as the developing world for POC (point-of-care) diagnosis and analysis. This thesis work has made a great achievement towards the final goal.

Acknowledgements

At the outset, I would like to express my sincere gratitude to my supervisor Prof. Dongqing Li, for his support and patience. Firstly, I would like to thank him for giving me the opportunity to pursue this Ph.D degree. My original background, Biomedical Engineering, was quite different from his research fields. However, he believed in me and continually encouraged me. As a result, I have been able to make several key contributions to the new research fields – immunoassay and lab-on-a-chip microfluidic devices. He always emphasized the importance of hard work and perseverance as an independent researcher in order to have deep insights. I had a great PhD study under his supervision. His help and support was truly beyond the traditions of academic study.

I also thank the other members of the dissertation committee, Prof. Mustafa Yavuz, Prof. Zhongchao Tan, Prof. Chang-qing Xu and Prof. Boxin Zhao for carefully reading my thesis and providing valuable comments.

I would like to acknowledge Prof. Niels Bols and his Ph.D student Nguyen Vo for their efforts to collaborate with me during this project.

I would like to thank my colleagues and fellow graduate students Dr. Xudong Wu, Fang Zhang, Saeid Movahed, Yasaman Daghighi and Chong Shen. I enjoyed their kind support during my studies.

And last, but not the least, I'd like to thank my wonderful family for the unwavering support they have consistently given to me during my life.

Dedication

This dissertation is dedicated to my brilliant wife, Xuan Weng, our exuberant, sweet, and kind-hearted little boy, Ivan Chenxi Jiang, and to my always encouraging, ever faithful parents.

Table of Contents

Author's Declaration	ii
Abstract	iii
Acknowledgements	v
Dedication	vi
Table of Contents	vii
List of Figures	x
List of Tables	xvi
Chapter 1 Introduction.....	1
1.1 Background	1
1.2 Research objectives	2
1.3 Outline of thesis.....	2
Chapter 2 Literature Review	4
2.1 Introduction	4
2.2 Flow cytometry.....	4
2.2.1 The principle of the commercial flow cytometer	4
2.2.2 Microfluidic flow cytometer.....	6
2.2.2.1 Fluidic control subsystem.....	7
2.2.2.2 Focusing subsystem.....	10
2.3 Detection methods for microfluidics	12
2.3.1 Optical detection.....	12
2.3.1.1 Fluorescence detection	12
2.3.1.2 Chemiluminescence detection	16
2.3.1.3 Thermal lens microscope.....	18
2.3.1.4 Surface plasmon resonance	20
2.3.1.5 Absorption detection.....	23
2.3.2 Non-optical detection	24
2.3.2.1 Electrochemical detection.....	24
2.3.2.2 Quartz crystal microbalance	28
2.3.3 Summary.....	30
2.4 Optical detection in microfluidic flow cytometry	31
2.5 Concluding remarks.....	33

Chapter 3 Study of Electrokinetically-induced Pressure-Driven Flow in a T-shaped microfluidic chip	35
.....	35
3.1 Introduction	35
3.2 Principle of electrokinetically-induced pressure-driven flow.....	35
3.3 Numerical study.....	37
3.3.1 Physical modeling	37
3.3.2 The flow field in the T-shaped microchannel.....	38
3.3.3 Influence of the pressure-driven back flow	43
3.3.4 The relationship between the average velocity in vertical channel and the horizontal channel size	45
3.3.5 The relationship between the average velocity in the vertical channel and different electrical field intensity	46
3.3.6 The simulation of the motion of particles.....	46
3.3.7 Summary.....	48
3.4 Experimental study	48
3.4.1 Material and solution	48
3.4.2 Chip and electrode fabrication.....	48
3.4.3 Chip design.....	50
3.4.4 Experimental setup and operation	52
3.4.5 Experimental results	54
3.5 Concluding remarks.....	57
Chapter 4 Study of Dual-Wavelength Fluorescent Detection of particles/cells on a novel microfluidic chip	59
.....	59
4.1 Introduction	59
4.1.1 Light source	59
4.1.2 Optical system	60
4.2 Methods	60
4.2.1 Electrokinetically-induced pressure-driven flow.....	60
4.2.2 Low-cost, dual-wavelength fluorescent detection system	62
4.2.3 Chip fabrication and sample preparation.....	63
4.2.4 Experiment setup	65

4.3 Results and discussion.....	66
4.4 Concluding remarks.....	70
Chapter 5 Study of a Novel Flow Focusing Method in a Microfluidic Chip for Dual-wavelength Fluorescent Detection of Particles.....	71
5.1 Introduction.....	71
5.2 Principle of flow focusing method.....	71
5.3 Theory.....	72
5.4 Numerical study.....	74
5.4.1 Physical modeling.....	75
5.4.2 Results and discussion.....	77
5.5 Experimental study.....	89
5.5.1 Material and solution.....	89
5.5.2 Chip fabrication.....	89
5.5.3 Chip design.....	90
5.5.4 Experimental setup and operation.....	87
5.5.5 Experimental results.....	92
5.6 Concluding remarks.....	99
Chapter 6 Conclusions and Future Work.....	100
6.1 Contributions of this thesis.....	100
6.2 Publications resulting.....	101
6.3 Suggestions for future work.....	102
Appendix A.....	103
Bibliography.....	107

List of Figure

Figure 2-1 A simplified schematic diagram of a typical flow cytometer (Used with permission by Life Technologies Corporation).....	5
Figure 2-2 Microfluidic pumping force for fluid control system. (A) Capillary pump. (B) Manual compression. (C) Centrifugal force. (D & E) Peristaltic pumps. (F) Syringe pump. (G) Electro-osmotic pump (Used with permission by Expert Reviews Ltd).....	9
Figure 2-3 The schematic of the microfluidic measuring system with the laser induced fluorescence method.....	13
Figure 2-4 (a) Layout of the integrated microfluidic device for clenbuterol immunoassay. (b) Photograph of the prototype microfluidic device. (c) Cross-sectional view of microvalves on chip. (d) Scheme of the optical configuration of the confocal LIF scanning system. (Source: Jing Kong and Bingcheng Lin et al. 2009).....	14
Figure 2-5 Image of IMPOD with hardware components. Inset shows glass microdevice used in performing immunoassays. (Source: Amy E. Herr and Anup K. Singh, 2007).....	14
Figure 2-6 a) Illustration of a fluorescence polarization apparatus. b) Principle of the assay of binding reaction using fluorescence polarization. (Source: K. Kakehi and Y. Oda et al., 2001).....	15
Figure 2-7 The principle of the Chemiluminescence detection method.....	16
Figure 2-8 Schematic of the experimental set-up for on-chip antioxidant capacity screening. (Source: Xuhua Wang and Andrew J. de Mello et al., 2009).....	17
Figure 2-9 The schematics of the thermal lens microscope.....	18
Figure 2-10 The micro-ELISA system. (a) A glass chip integrated with microfluidic channels was used for the OS-ELISA reaction. (b)-(e) Polystyrene beads with immobilized MBP-VL were introduced and stored between a dam structure and the three-way junction. Extra beads were flushed away. The reagents were introduced into the microchip to form an immuno-complex on the beads. After washing, the substrates were applied and dye molecules produced by the enzyme reaction were detected by a TLM downstream of the dam structure. The microbeads after each assay were flushed by an inversed flow. (Source: Masaki Ihara and Hiroshi Ueda et al. 2010).....	19
Figure 2-11 Schematic view of the SPR immunoassay technique.....	21
Figure 2-12 (a) Microarray of gold iSPR sensing islands. (b) glass-PDMS microfluidic chip. (c) The iSPR interface module with chip fixture with integrated platinum electrodes. (d) Electrical circuit. (Source: Krishnamoorthy et al. 2010).....	22
Figure 2-13 Three-electrode cell and notation for the different electrodes.....	24

Figure 2-14 (a) Schematic diagram of the microfluidic immunoassay system. (b) The chamber holding the polybeads. (c) A photograph of the immunoassay microchip. (Source: Sung Ju Yoo and Sang-Hoon Lee et al. 2009).....	25
Figure 2-15 (b) Photograph of a glass slide with three electrochemical cells. (c) Schematic representation of the reference (ER), interdigitated working (Ew), and counter electrodes (EA). (Source: I-Jane Chen and Erno Lindner, 2009).....	26
Figure 2-16 (a) Schematic cross-sectional (top) and top view (down) of the microsystem. (b) Exploded to scale view of the designed four-component system: the silicon substrate, the VCAF, the quartz crystal and the protective polymer cap. (c) Front and backside pictures of two devices. The QCM crystal is visible through the polymer backside cover. (Source: Thomas Frisk and Goran Stemme et al. 2008).....	29
Figure 3-1 Schematic diagram of the proposed method to generate electrokinetically-induced pressure-driven flow. The s-s is the central line of the microchannel. The particles/cells are loaded in reservoir C. Reservoirs A and B contains initially the buffer solution. The red lines show the position of the electrodes.....	36
Figure 3-2 (a) Pressure gradient distribution in the T-shaped microchannel. (b) Electrical field distribution in the T-shaped microchannel. The width of horizontal channel is 100 μm . Electrical field intensity is 100 V/cm (-50 V at A, B and 0 V at Point O)	40
Figure 3-3 The velocity profile in the T-shaped microchannel. The width of horizontal channel is 100 μm . Electrical field intensity is 100 V/cm (-50 V at A, B and 0 V at Point O)	41
Figure 3-4 The velocity profile in the T-shaped microchannel. The width of horizontal channel is 25 μm . Electrical field intensity is 100 V/cm (-50 V at A, B and 0 V at Point O)	42
Figure 3-5 The relationship between the average velocity in vertical channel and the pressure drop for different horizontal channel size. Electrical field intensity is 100 V/cm (-50 V at A, B and 0 V at Point O)	44
Figure 3-6 The relationship between the average velocity in vertical channel and the different horizontal channel size under the same electrical field intensity. Electrical field intensity is 100 V/cm (-50 V at A, B and 0 V at Point O)	45
Figure 3-7 The relationship between the average velocity in vertical channel and the applied electric voltages at reservoirs A and B. Electrical field intensity is 100 V/cm, 200 V/cm, 300 V/cm and 400 V/cm, respectively (-50 V, -100 V -150 V, -200 V at A, B and 0 V at Point O)	46

Figure 3-8 Sequential images of the simulation of particle's motion. Cross-sections are $25\mu\text{m}$ (w) \times $25\mu\text{m}$ (h) in horizontal channel and $100\mu\text{m}$ (w) \times $25\mu\text{m}$ (h) in vertical channel. Electrical field intensity is 100 V/cm (-50 V at A, B and 0 V at Point O). Diameter of the particles is set up to $10\mu\text{m}$ 47

Figure 3-9 Soft lithography protocol. UV light is used to project channel patterns of a high resolution photomask onto photoresist. Once the photoresist is developed, only the exposed parts remain. They act as a negative mold onto which liquid PDMS is poured. Subsequently, the PDMS is baked at $65\text{ }^\circ\text{C}$. Cured PDMS is peeled off the mold revealing the positive channel structures. After punching wells, the PDMS microchip is bonded to a glass slide in a plasma oven (Used under permission by Expert Reviews Ltd) 49

Figure 3-10 Two-dimensional (x - y plane) illustration of the microchannel design used in this study 52

Figure 3-11 The microfluidic chip and the experimental system: a picture of the chip and the illustration of the experimental system..... 53

Figure 3-12 A series of fluorescent images of electrokinetic transport of Rhodamine B dye solution in microchannels. Red strips were fluorescent dye moving in the horizontal channel and the vertical channel ($E=100\text{ V/cm}$. -50 V is applied at the two ends of the channel A-B and 0 V at point O) 54

Figure 3-13 A series of fluorescent images of the motion of $10\mu\text{m}$ and $5.76\mu\text{m}$ fluorescent microspheres ($E=100\text{ V/cm}$. -50 V is applied at the two ends of the channel A-B and 0 V at point O). The upper four images indicate the $10\mu\text{m}$ fluorescent microspheres flowing in the vertical channel at different time. The bottom four images show the $5.76\mu\text{m}$ fluorescent microspheres flowing in the vertical channel at different times 55

Figure 3-14 A series of images of the motion of real blood cells ($E=60\text{ V/cm}$, -30 V was applied at the two ends of the channel A-B and 0 V at point O). The four images indicated the blood cells flowing in the vertical channel at different time..... 56

Figure 3-15 A series of images of the motion of real blood cells ($E=60\text{ V/cm}$, -30 V was applied at the two ends of the channel A-B and 0 V at point O). The four images indicated the blood cells passing through the converging-diverging section.in the vertical channel at different time 57

Figure 4-1 (a) Schematic diagram of a new method to generate electrokinetically-induced pressure-driven flow in a microchannel. The arrows indicate the flow directions. The particles/cells are loaded initially in reservoir C. (b) A photograph of the microfluidic chip 61

Figure 4-2 (a) Schematic of the dual-wavelength optical detection system. (1) Bi-colour blue/red LED; (2) dual-wavelength excitation filter; (3) band-pass emission filter (535 nm); (4) photodiode 1; (5) band-pass emission filter (710 nm); (6) photodiode 2, (7) microfluidic chip. (b) A photograph of the optical detection system.....	63
Figure 4-3 Illustration of the experimental system which consists of the microfluidic chip, a two-stage amplification circuit, a fluorescent detection system, DC power supplies, and a data acquisition system.....	65
Figure 4-4 The average velocity of the particles moving in the L-shaped channel under different voltages applied at the reservoirs A and B.	66
Figure 4-5 An example of the detected signals from a sample containing 7.0 μm Dragon Green fluorescent beads (a) and 7.0 μm Flash Red fluorescent beads (b). The ratio of the Dragon Green fluorescent beads to the Flash Red fluorescent beads is 1 to 3.....	68
Figure 4-6 The number counts for two fluorescent particles determined by a commercial flow cytometer. (a) The counting result for two different types of fluorescent particles in Exp. 1 in Table 1. (b) The counting result for two different types of fluorescent particles in Exp. 2 in Table 1.	69
Figure 5-1 Schematic diagram of the proposed method to generate electrokinetically-induced pressure-driven flow and two sheath flows	74
Figure 5-2 The velocity profile in the T-shaped microchannel. The red vectors and stream line show the direction of the flow field (50 V at C, D, C', D' and 0 V at Point O' and O'')	78
Figure 5-3 The velocity profile in the T-shaped microchannel. The red vectors and stream line show the direction of the flow field (-50 V at A, B and 0 V at Point O)	79
Figure 5-4 The velocity profile in the T-shaped microchannel. The red vectors and stream line show the direction of the flow field. The bottom plot shows the concentration field in the in the T-shaped microchannel (-100 V at A, B and 0 V at Point O; 50 V at C, D, C', D' and 0 V at Point O' and O'')	81
Figure 5-5 The velocity profile in the T-shaped microchannel. The red vectors and stream line show the direction of the flow field. The bottom plot shows the concentration field in the in the T-shaped microchannel (-75 V at A, B and 0 V at Point O; 50 V at C, D, C', D' and 0 V at Point O' and O'')	82
Figure 5-6 The velocity profile in the T-shaped microchannel. The red vectors and stream line show the direction of the flow field. The bottom plot shows the concentration field in the in the T-shaped	

microchannel (-150 V at A, B and 0 V at Point O; 50 V at C, D, C', D' and 0 V at Point O' and O'')	83
Figure 5-7 Sequential images of the simulation of particle's motion in the channel. 1000 particles of 10 μm diameter are released at the sample inlet (-150 V at A, B and 0 V at Point O; 50 V at C, D, C', D' and 0 V at Point O' and O'')	85
Figure 5-8 The top view of the vertical channel and the particle's motion. The red dashed lines show the focusing stream. The black dashed line is the center line of the vertical channel. (a) -150 V is applied at A, B and 0 V is applied at Point O; 50 V is applied at C, D, C', D' and 0 V is applied at Point O' and O''. (b) -200 V is applied at A, B and 0 V is applied at Point O; 75 V is applied at C, D, C', D' and 0 V is applied at Point O' and O''. (c) -300 V is applied at A, B and 0 V is applied at Point O; 125 V is applied at C, D, C', D' and 0 V is applied at Point O' and O''	88
Figure 5-9 (a) Schematic diagram of a new method to generate electrokinetically-induced pressure-driven flow and two sheath flows in a microchannel. (b) A photograph of the microfluidic chip	91
Figure 5-10 (a) A fluorescent image of flow focusing effect in the vertical microchannel. (b) A simulation image of flow focusing effect in the vertical microchannel (-150 V at A, B and 0 V at Point O; 50 V at C, D, C', D' and 0 V at Point O' and O'')	92
Figure 5-11 (a) A fluorescent image of flow focusing effect in the vertical microchannel. (b) A simulation image of flow focusing effect in the vertical microchannel (-100 V at A, B and 0 V at Point O; 25 V at C, D, C', D' and 0 V at Point O' and O'')	93
Figure 5-12 (a) - (d) A series of images of the motion of 7 μm microspheres (-150 V at A, B and 0 V at Point O; 50 V at C, D, C', D' and 0 V at Point O' and O''). (e) - (h) A series of simulation images of the motion of 7 μm microspheres (-150 V at A, B and 0 V at Point O; 50 V at C, D, C', D' and 0 V at Point O' and O'')	95
Figure 5-13 The focusing effect of 7 μm diameter microspheres in the vertical channel. (a) The width of the vertical channel is 100 μm (-150 V at A, B and 0 V at Point O; 50 V at C, D, C', D' and 0 V at Point O' and O''). (b) The width of the vertical channel is 50 μm (-150 V at A, B and 0 V at Point O; 50 V at C, D, C', D' and 0 V at Point O' and O'')	96
Figure 5-14 The focusing effect of 0.5 μm diameter microspheres in the vertical channel. (a) The comparison between the experimental result and the simulation result for the flow focusing effect (-300 V at A, B and 0 V at Point O; 125 V at C, D, C', D' and 0 V at Point O' and O''). (b) The comparison between the experimental result and the simulation result for the flow focusing effect (-	

300V at A, B and 0 V at Point O; 60 V at C, D, C', D' and 0 V at Point O' and O''). The width of the vertical channel is 100 μm97

Figure 5-15 The estimation of the average velocity of the particles in the vertical channel with different applied voltages.98

List of Table

Table 4-1 Comparison of the ratios of particles/cells detected by the device of this study and a commercial flow cytometer. PD stands for photo-detector	68
Table 5-1 Comparison of the ratios of particles/cells detected by the device of this study and a commercial flow cytometer. PD stands for photo-detector. (-300 V is applied at A, B and 0 V is applied at Point O; 125 V is applied at C, D, C', D' and 0 V is applied at Point O' and O'').)	99

Chapter 1

Introduction

1.1 Background

Flow cytometry is an analysis tool that has been developed for more than 40 years. It is widely employed for the diagnosis of many diseases because of its capabilities of counting, characterizing, and sorting cells.¹⁻⁴ Recently, on-site detection of different diseases from human cells such as leukocytes or cancer cells has become highly desirable, particularly in resource-limited settings, because of increasing demands for early diagnostics and rapid testing results. However, most flow cytometry tests are performed at hospitals, medical laboratories or outpatient clinics. In developing countries and some low-resource settings, the long testing time, the high cost and the large sample consumption are not desirable. The high cost, the large size, and the complexity in operation and maintenance limit the application of flow cytometers.⁵⁻⁷

POC (point-of-care) device should be able to analyze small volumes of body fluids such as blood, saliva and urine, and minimize the number of assay steps, such as sample preparation and washing processes. The cost of POC diagnosis device should be low. In addition, its applications in the resource-limited settings such as insufficient water, high or low temperatures, humidity and poor power supply should also be considered. In order to overcome these weaknesses, it is highly desirable to develop portable, low-cost flow cytometry devices.

In recent years, the rapid development of microfluidic and lab-on-a-chip technology has created a pathway for creating portable flow cytometers for the point-of-care diagnostics⁸⁻¹¹ in low-resource settings. Microfluidic devices allow for the integration of multiple liquid handling processes required in diagnostic assays, such as pumping, metering, sampling, dispensing, and sequential loading and washing. These lab-on-a-chip solutions have been recognized as an opportunity to bring portable, accurate and sensitive diagnostic tests to conventional flow cytometers in low-resource settings as well as in the developing world. It provides a very promising way to miniaturize the size with added benefits such as portability, improved reaction kinetics, minimal reagent consumption, automation and parallel processing.¹²⁻¹⁴ In order to obtain quantitative results, the microfluidic chips can be combined with optical, electrical, and mechanical sensors in an integrative format. Generally, the detection system in the flow cytometer must be small in size and have high sensitivity and response

time. For the past two decades, a handful of research teams around the world have involved in the research of the microfluidic flow cytometry devices.¹⁵⁻¹⁸ However, most current proposed microfluidic flow cytometry devices are micro- only in the microfluidic chip. The rest of most apparatuses such as pumps, valves and tubing s are still bulky and expensive, which is very difficult to integrate into the system.

1.2 Research objectives

In order to overcome the shortcomings of current flow cytometry devices, the major objective of this thesis is to develop a novel lab-on-a-chip system based on electrokinetically-induced pressure-driven flow and dual-wavelength fluorescent detection, which will light a promising pathway to make a real portable, compact, low-cost microfluidic flow cytometry device. Compared to other devices, this proposed microfluidic system can significantly reduce the size, the assay consumption and the cost while maintain a comparable detection sensitivity. Most importantly, the external mechanical pumps, valves and tubing need to be eliminated. The efforts made in this thesis should address the biggest difficulty which prevents it from developing a real portable, low-cost flow cytometry device.

1.3 Outline of thesis

The complete thesis comprises the following major sections:

Chapter 1 serves as an introduction to this thesis. The background, objectives and the scope of the thesis are also given in this chapter.

Chapter 2 reviews commercial benchtop flow cytometers and current microfluidic flow cytometers. A comprehensive understanding on the pros and cons of current microfluidic device set-ups including the flow control system and the flow focusing system helps us to improve the functionality of the proposed design. Furthermore, this review examines the status and the major development of detection methods that can be applied in the microfluidic device, especially the optical detection method for the microfluidic flow cytometry.

Chapter 3 introduces a novel approach for generating a continuous pressure-driven flow and transporting the particles or biological cells in the T-shaped microchannel by using the electrokinetically-induced pressure-driven flow. Thus, the shortcoming associated with the electrokinetic force and the pressure pumping force when employed individually is avoided. This is the fundament of this study.

Chapter 4 presents a fluorescence-activated particle counting system based on electrokinetically-induced pressure-driven flow and a miniaturized dual-wavelength fluorescent detection method. This design of the two-wavelength fluorescent detection system leads to a significant reduction in volume and cost, compared with other microfluidic fluorescent detection devices reported in literature.

Chapter 5 describes a novel flow focusing method that allows hydrodynamic focusing in a T-shaped microchannel with two sheath flows. Sample stream and sheath flows flowing through the T-shaped microchannel are generated by electrokinetically-induced pressure-driven flow. Compared to other flow focusing methods, this novel approach decreases the number of required components such as air pump or syringe pump. It reduces the complexity of fabrication for hydrodynamic focusing, and enables an easy integration with other microfluidic components.

Chapter 6 summarizes the major findings and contribution of this work. Recommendations for future projects are briefly outlined.

Chapter 2

Literature Review

2.1 Introduction

In this chapter, first, it is worth looking into the principle of commercial benchtop flow cytometers and current microfluidic flow cytometry devices. A comprehensive understanding on the pros and cons of current microfluidic device set-ups including the flow control system and the flow focusing system helps me to improve the functionality of the proposed design. Furthermore, this review examines the status and the major development of detection methods that can be applied in the microfluidic device, especially the optical detection method for the microfluidic flow cytometry.

2.2 Flow cytometry

2.2.1 The principle of the commercial flow cytometer

Flow cytometer is a bio-analysis tool that is widely applied to diagnosis and treatment of many human diseases due to its ability to count, characterize and sort particles or cells. By using flow cytometers, medical practitioners can obtain abundant information on both biological and physical properties of interested human samples such as different types of cells, bacteria and virus. Moreover, flow cytometer can supply a non-destructive and highly quantitative approach. Therefore, flow cytometer is commonly used for the analysis of cellular antigens, studies of different cellular parameters, cell biology, cell cycle analysis etc. in various research fields.¹⁹⁻²³

Generally, the flow cytometer implements the analysis by passing thousands of cells per second through a laser beam and capturing the light from each cell when it passes. The light signals are collected by the sensor and converted into electrical signals. Then, the data is logged into the computer and analyzed by the flow cytometry software.

A traditional flow cytometry system has three main units: the sample injection and fluidic system, which conducts samples to the detection zone and takes away the waste samples; the optical detection system, which is used to excite and collect the lights; and the computer analysis system, which convert the signals from the detectors into the digital data and perform the analyses. Figure 2-1 shows the main principle of a commercial flow cytometer. One of the basic principles of flow cytometry is

the ability to analyze individual particles. It is well known that when the particles or cells are injected into a flow cytometer, the particles/cells are randomly dispersed throughout the suspending medium. For accurate data collection, it is important that particles or cells are passed through the laser beam one at a time. This function is realized by using the hydrodynamic focusing method. Figure 2-1 shows that the sample is injected into a narrowing core channel under pressure. An outer sheath fluidic system surrounds this core channel. Two sheath flows which flow faster than the injected sample flow are generated under lower pressure. Sheath flows can produce a great drag effect on the core channel. This drag force can compress the sample stream to a single file according to the size of the particles or cells.

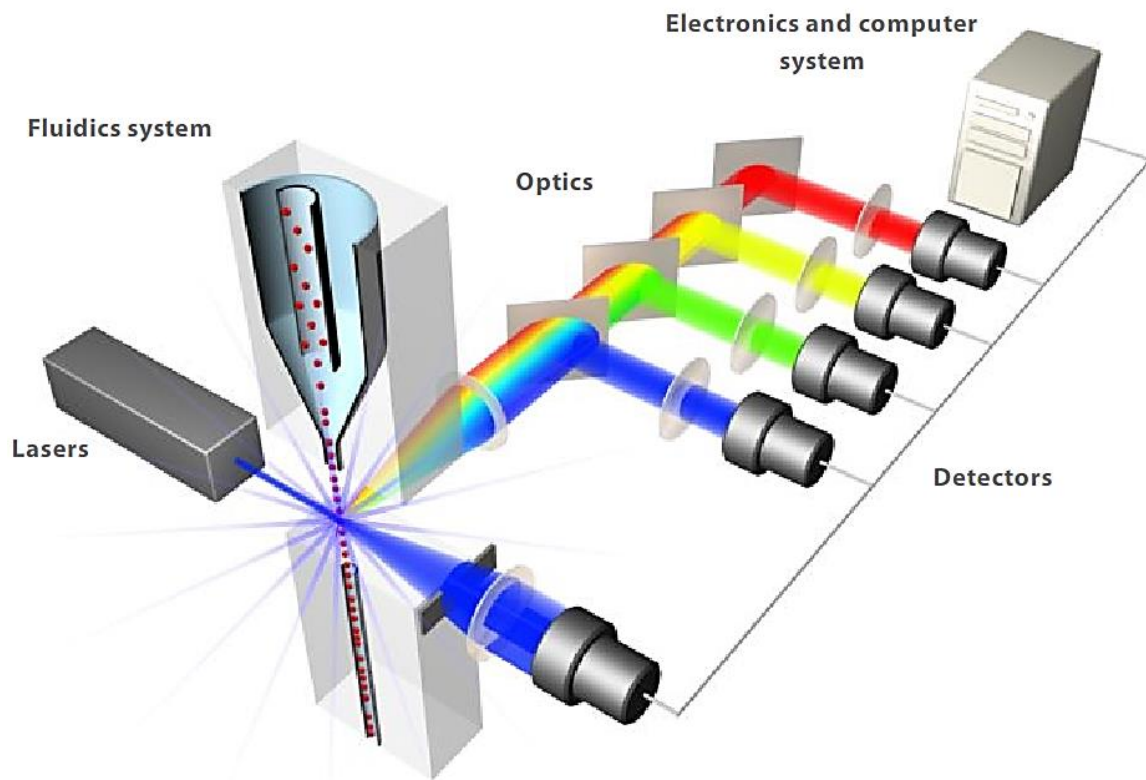


Figure 2-1 A simplified schematic diagram of a typical flow cytometer (Used with permission by Life Technologies Corporation).

Optical detection unit consists of a light source, lenses, dichroic mirrors, filters and photo detectors. The light source is typically a laser. Air-cooled gas lasers have been integrated into flow cytometers for years. The argon-ion and He-Ne (helium-neon) lasers are the most prominent examples. Lenses and filters which are placed in front of the detectors are used to gather and direct the emission lights

from the particle/cell. The cell samples are introduced into the injection unit hydrodynamically and focused by two sheath flows which are used to ensure that the cells can travel in the fluidic channel one by one. When cells reach the interrogation zone, cells are detected individually by the focused light beam which is passing through the channel perpendicularly. In a typical flow cytometer, the scattered light and fluorescent light are recorded. In most cytometers, an obscuration bar is placed in front of the forward detector. The obscuration bar prevents any of the intense laser light from reaching the detector. As a cell crosses the laser, light is scattered around the obscuration bar and is collected by the detector. The magnitude of forward scatter is roughly proportional to the size of the particle/cell. The fluorescent lights are emitted from the labeled particle/cell. These lights pass through a lens system which consists of dichroic mirrors and filters and are divided into different wavelength ranges. The different wavelengths of light are captured by a series of appropriate detectors. The most commonly used photo detector in conventional flow cytometers is the PMTs (photomultiplier tubes). PMTs are highly sensitive to weaker signals generated by fluorescence. However, PMTs are relatively large (hand size) because of their vacuum tube structure.

Nearly two decades, benefitting from the development of new hardware and software, modern flow cytometers have been developed for fast and accurate cell processing and analysis.²³ However, there still exists many shortcomings which prevent the further development of flow cytometers. For example, to realize the multifunctional applications, two and more lasers, lenses, filters and photodetectors must be added into the system.²⁴⁻²⁶ To operate commercial flow cytometers, highly trained personnel are generally required as well as bulky and costly equipment. These factors are the key reasons that most commercial flow cytometers are still of large size, not portable and complex. All of these limit its use for POC (point-of-care) applications.

2.2.2 Microfluidic flow cytometry

In order to overcome the weaknesses of conventional flow cytometers, researches and scientists introduce the concept of microfluidics to the flow cytometry. It is called 'microfluidic flow cytometry'. In recent years, the rapid development of microfluidics based on lab-on-a-chip technology has created a new pathway for the POC flow cytometry. Microfluidic flow cytometry system allow the integration of multiple liquid handling processes required in diagnostic assays, such as pumping, metering, sampling, dispensing, and sequential loading and washing. These lab-on-a-chip solutions have been recognized as an opportunity to bring portable, accurate and sensitive diagnostic tests to POC diagnostics²⁷⁻³⁰ in low-resource settings as well as in the developing world.

Furthermore, it provides a very promising way to miniaturize conventional flow cytometers with added benefits such as portability, improved reaction kinetics, minimal reagent consumption, automation and parallel processing.³¹⁻³³

Similar to the conventional flow cytometry, typical microfluidic flow cytometry devices are also composed of three major subsystems: the fluidic control and focusing subsystem, the optical detection subsystem and the analysis subsystem. The fluidic control and focusing subsystem is realized by applying a microfluidic chip which is usually fabricated by the lithography/soft-lithography technology. By applying a pumping force, the sample can be easily driven in the microchannels. Due to the extremely small size of the microfluidic chip, microfluidic flow cytometer can operate with small sample and reagent volumes, thus reducing the cost greatly. A mass-product chip would be more easily accepted by research laboratories and medical clinics. Unlike the bulky optical detection unit in conventional flow cytometers, microfluidic flow cytometry devices utilize an integrated optical detection component for the illumination of samples and collection of emitted light. This can dramatically decrease the service and maintenance requirements. With the development of computer science and microelectronics, the analysis can be easily miniaturized and integrated into the microfluidic flow cytometry devices. For the past two decades, a handful of research teams around the world have been involved in the research of microfluidic flow cytometry devices.

2.2.2.1 Fluidic control subsystem

The fluidic control system of a flow cytometer is used to introduce a randomly distributed solution of cells. This is a key part which determines the portability of flow cytometry devices. To design the fluidic control system, the fluid pumping force must be carefully chosen. Different pumping forces require the different control system structures and sizes. Most microfluidic flow cytometers utilize a pressure-driven pumping method³⁴⁻³⁵ such as a syringe pump or a piezoelectric pump. Figure 2-2 lists several representative pumping forces which can be applied on the microfluidic chip. Figure 2-2 (A) demonstrates the capillary pumping force.³⁶⁻³⁸ Due to the surface tension of the fluid, the sample solution is driven along the microchannel wall. This phenomenon can be easily utilized in a microfluidic chip to create a capillary pump force for driving the liquid. However, this kind of fluid control is rarely used in microfluidic flow cytometers due to the low flow rate and the uncontrollability in a given experiment. Higher flow rates can be achieved through manual compression of the liquid reservoir (Figure 2-2 (B)). For example, after pressing the bellow, a pressure-driven flow is generated, which drives the liquid into the microfluidic channel. By using the

flexible material, the bellow can be integrated into the microchip. This method can generate high flow rate which depends on the manual compression force, however, it still cannot be controlled. In Figure 2-2 (C), the high-speed rotation on a compact disk generates a strong centrifugal force which can be utilized as a microfluidic pumping force. In recent years, the microfluidic CD (compact disk) has become a promising platform for POC applications.³⁹⁻⁴⁰ However, generating centrifugal force requires precise design and control, and also requires an external spinner for centrifugal separation. Figure 2-2 (D) and (E) show two different types of the peristaltic pumping force.⁴¹⁻⁴² No matter which type of peristaltic pumping force is chosen, an external device must be added. For example, in Figure 2-2 (E), air pressure is sequentially applied into air channels which are perpendicular to a liquid-filled sample channel to push the liquid flowing along the channel. To generate the air pressure, an air pump must be connected to the air channels. Another big problem with the peristaltic pumping force is that the flow in the channel is pulse flow which depends on the pushing frequency.

Without exception, in conventional flow cytometers, a pressure pumping force is the best option because it can be easily generated by an air pump. In this way, a high level of control can be achieved and relatively large volumes can be rapidly processed, even in narrow channels with high resistance. The flow rate can be controlled by adjusting the pressure difference between the entrance and the exit at any desired speed. The highlight of using a pressure pumping force is that it is a non-destruct approach for cell detection. The properties of the sample will not be changed under the pressure pumping force. Practically, in many microfluidic flow cytometers, a syringe pump (Figure 2-2 (F)) is utilized to generate a pressure-driven flow.⁴³⁻⁴⁵ Fluid is driven in the microchannels by mechanically pushing the plunger of a standard laboratory syringe. However, to generate a pressure pumping force, bulky pumps, tubing and valves are often needed which are difficult to integrate into microfluidic flow cytometers. Moreover, pipes and valves are required between the microfluidic chip and the pump, resulting in sealing and operating difficulties. Furthermore, the need of this external equipment will significantly increase the volume of the cell samples.

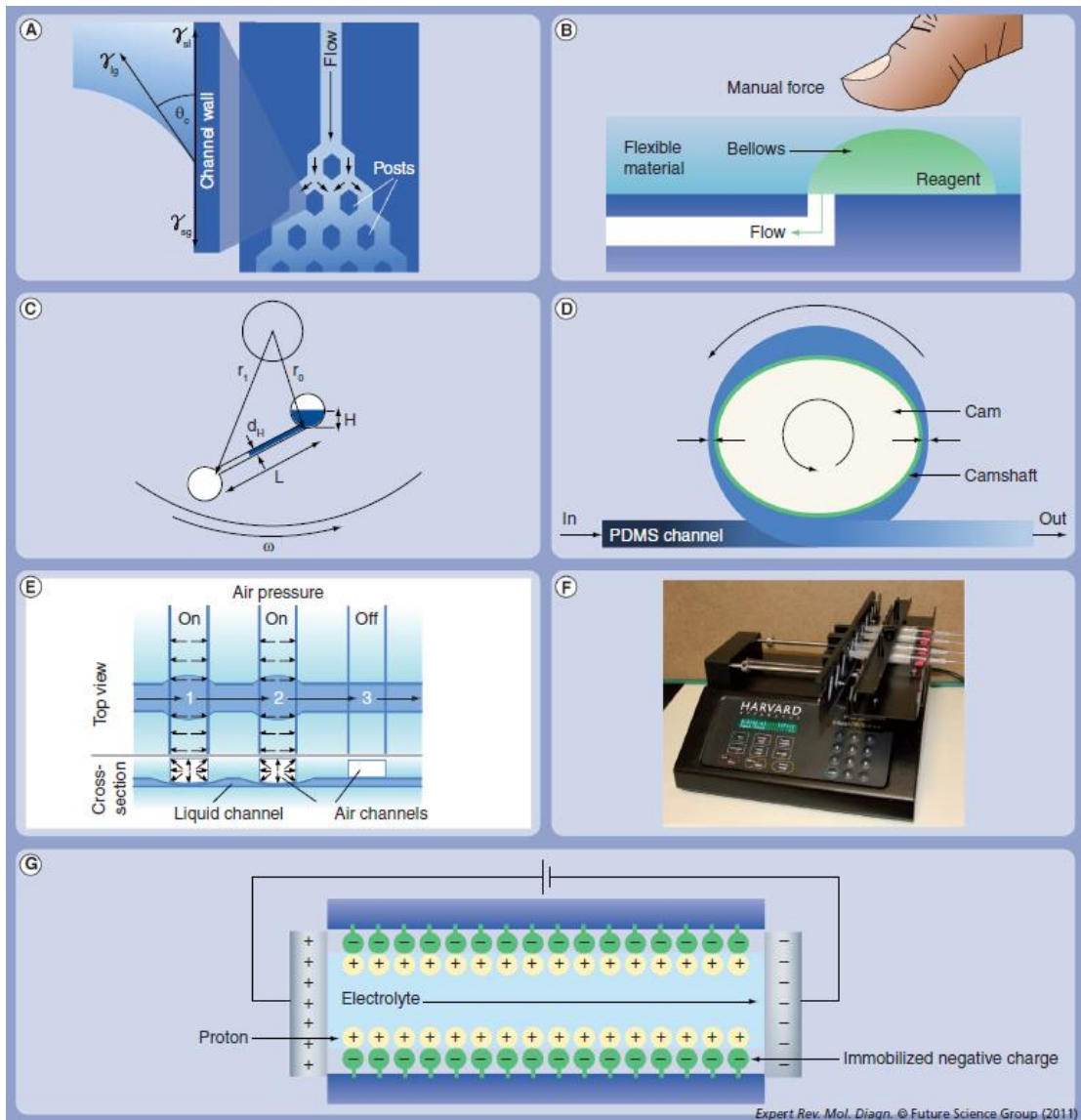


Figure 2-2 Microfluidic pumping force for fluid control system. (A) Capillary pump. (B) Manual compression. (C) Centrifugal force. (D & E) Peristaltic pumps. (F) Syringe pump. (G) Electro-osmotic pump (Used under permission by Expert Reviews Ltd).

Alternatively, an electro-osmotic pumping can be used in microfluidic cell cytometers (Figure 2 (G)). In a microchannel filled with an aqueous solution, the electrostatic charge on the solid surface will attract counter-ions in the liquid to form an electric double layer. An externally applied electrical field will cause excess counter-ions in the electric double layer to move and consequently generate the liquid motion in the microchannel via viscous effect. This is called electroosmotic flow. It is well-

known that the EOF (electro-osmotic flow) method can generate and control the flow in microchannels precisely. Electro-osmotic flow can be generated easily by a DC (direct current) potential difference between the inlet and outlet of a microfluidic channel. It does not require any mechanical parts and it allows an extremely constant flow rate to be established without any pulsing effects. Therefore, the use of an electro-osmotic pumping force can overcome the weaknesses associated with the pressure pumping force due to its ease of automation, integration and miniaturization.⁴⁶⁻⁴⁸ However, the electroosmotic pumping also has some disadvantages. For example, under the applied electric field, the properties of cells may be changed, or the cells may be killed. For example, the irregular motion of cells was observed and studied by Minerick et al..⁴⁹ They found that the irregular motion of the cells was caused by a pH gradient between electrodes due to electrolysis reactions. The pH gradient changed local zeta potentials of both the PDMS (polydimethylsiloxane) channel and blood cells. Consequently, the local EOF velocity and the electrophoretic velocity of blood cells were altered. Furthermore, a strong electric field can destroy the cell membrane.⁵⁰ Another concern is that the fluorescent dye may be affected under an electric field for a sufficiently long time.

2.2.2.2 Focusing subsystem

Conventional flow cytometers use a precise flow cell which allow for hydrodynamic flow focusing. Two sheath flows flow faster than the injected sample flow are generated under lower pressure. Sheath flows can produce a huge drag effect on the core channel. This drag effect can compress the sample stream to a single file according to the size of the particle or cell. Thus, the sample particle/cell can pass through the detection zone one by one, which can decrease the detection error greatly. However, conventional flow cytometer need large amounts of sheath flow reagent. A major goal driving the development of microfluidic flow cytometer is to reduce the size of the device and the amount of the sample reagent and the sheath fluid. To achieve the goal, new concepts must be done to implement the flow focusing on the microfluidic chip. In recent years, many methods have been proposed to achieve the flow focusing to align the particles in microfluidic channel.

Among the flow focusing methods, sheath flow focusing still is the most common one that has been developed in the microfluidic flow cytometer. Recently, Ligler research group⁵¹⁻⁵² proposed a 3D (three-dimensional) sheath flow focusing method by using the grooved microchannels based on the chevron design. This method created a vertical focusing. The height and width of sample stream can be controlled by the chevrons and sheath-to sample flowrate ratio. Dean flow is a secondary transverse flow induced by centrifugal effects in a curved channel.⁵³ Lee et al.⁵⁴ reported a CEA

(contraction–expansion array) microchannel that allows three-dimensional hydrodynamic focusing with a single sheath flow in a single-layer device. Xuan and Li⁵⁵ first investigated the electrokinetic focusing in microfluidic cross-channels. Compared to other focusing approaches, sheath flow focusing is mostly determined by the flow-rate ratio between the sheath fluid and the particle suspension and thus potentially able to focus very small particles. Moreover, both the location and the dimension of the focused particle stream are readily tunable, which can be achieved by adjusting the flow rate of each of the sheath fluids. However, the requirement of sheath flows complicates the device control, extends the size of the device and increases the device operation cost due to the consumption of sheath fluids.

Sheathless flow focusing methods are proposed to overcome the weakness of the sheath flow focusing. Sheathless flow focusing typically depends on a force to operate the particles laterally to their equilibrium positions in the microchannel. Recently, Acoustic flow focusing has been developed due to the non-destructive method for cell detection. This method can yield the acoustic wave-induced radiation pressure on particles. This pressure can force particles toward pressure equilibrium position depending on the density and compressibility of the particle and the medium. Shi et al.⁵⁶ introduced a novel on-chip focusing technique for focusing microparticles using SSAW (standing surface acoustic waves). Goddard et al.⁵⁷ evaluated the performance of a flow cytometer that uses acoustic energy to focus particles to the center of a flow stream by using quantitative measurements of fluorescent microspheres and cells. Although this method is simple and efficient, it typically requires the transducer to be placed in close proximity to the microchannel. This complicates the device fabrication and affects its integration with other functional components into devices. Another approach uses the inertia of the fluid acting on particles in microchannel to enable precise cell positioning in the stream. Carlo et al.⁵⁸ investigated the inertial focusing of particles in a straight microchannel. They observed that initially uniformly distributed 9 μm diameter beads were focused to four single streams in a square microchannel. Carlo et al.⁵⁸ also studied particle inertial focusing in curved microchannels. Inertia-based particle focusing method is easy to realize and can offer a very high particle throughput. However, the inertial focusing depends on very high flow rate to generate the decent inertia motion in the microchannel. Moreover, the equilibrium positions of the focused particle streams are sensitive to the particle's Reynolds number, the operation of such inertial particle focusing becomes complicated. DEP (dielectrophoresis) is another sheathless focusing approach which can be applied to the microfluidic flow cytometer. DEP is the translational motion of particles due to either induced or native electrical dipoles in an electric field gradient. Traditional

dielectrophoretic particle focusing methods are based on the non-uniform AC (alternating current) electric field between pairs of patterned microelectrodes inside microchannels. Recently, Chu et al.⁵⁹ presented a 3D particle focusing channel using the pDEP (positive dielectrophoresis) guided by a dielectric structure between two planar electrodes. Demierre et al.⁶⁰ reported a microfluidic device based on a novel geometrical arrangement of lateral metal electrodes and a patterned insulator. They utilized the principle of “electrodeless” dielectrophoresis with multiple frequencies to achieve focusing and continuous separation. For electrode-based AC dielectrophoretic particle focusing, fabrication of microelectrodes still remains challenging. The focusing efficiency is sensitive to the dielectrophoretic force. For example, if the particles are away from the electrode surfaces, the dielectrophoretic force on the particles decays rapidly. Moreover, dielectrophoretic force may cause the adhesion of particles in the microchannel, which can influence the detection greatly.

2.3 Detection methods for microfluidics

For most analysis on a microfluidic chip, the detection depends on the use of an analytical reagent that is associated with a detectable label such as radioactive elements, enzymes, kinds of particles (latex, magnetic, gold and silver) and others⁶¹⁻⁶⁷. According to the label used, detection methods can be classified as optical detection methods and non-optical detection methods on microfluidic chip. In the following, we will focus on the most common detection techniques used for microfluidics in recent years.

2.3.1 Optical detection

2.3.1.1 Fluorescence detection

The most commonly observed form of optical detection is fluorescence, because of its high sensitivity and the ease of integrating a label. Fluorescence is the emission of certain wavelength of visible light from a substance by the absorption of an excitation light of different wavelength LIF (laser induced fluorescence) has a high sensitivity and fast response. Figure 2-3 shows the basic principle of the of laser induced fluorescence method. A microscope focuses on the microchannel and connects to a CCD (charge coupled device) camera or photomultiplier tube. The excitation light is provided by a laser system. It passes through a beam splitter and is focused on the detection area. The fluorescence emission returns through the same beam splitter and is reflected towards the detection system. Jing Kong and Bingcheng Lin et al.⁶⁸ reported an integrated microfluidic system combining with

microvalves and micro-pumps for the clenbuterol immunoassay via the LIF detection method. This system consists of an integrated microchip and a linear confocal LIF scanner. The microfluidic chip is composed of three layers: a fluidic channel layer, a PDMS membrane layer and a pneumatic control layer (Figure 2-4). It should be noted that all parts of the fluorescence setup such as the lens, the excitation source and detection device, can be miniaturized. The entire device can be made portable. Amy E. Herr and Anup K. Singh⁶⁹⁻⁷⁰ developed a portable device for detection of potential biomarkers of periodontal disease in saliva. The microfluidic chip was integrated with miniaturized electronics, optical elements (such as diode lasers), fluid-handling components, and data acquisition software (Figure 2-5).

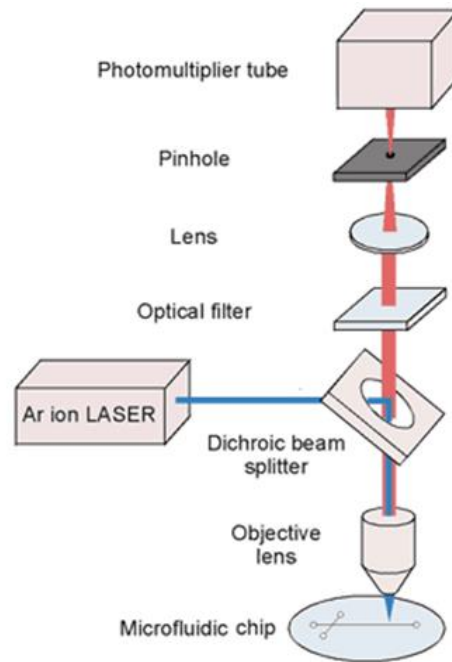


Figure 2-3 The schematic of the microfluidic measuring system with the laser induced fluorescence method.

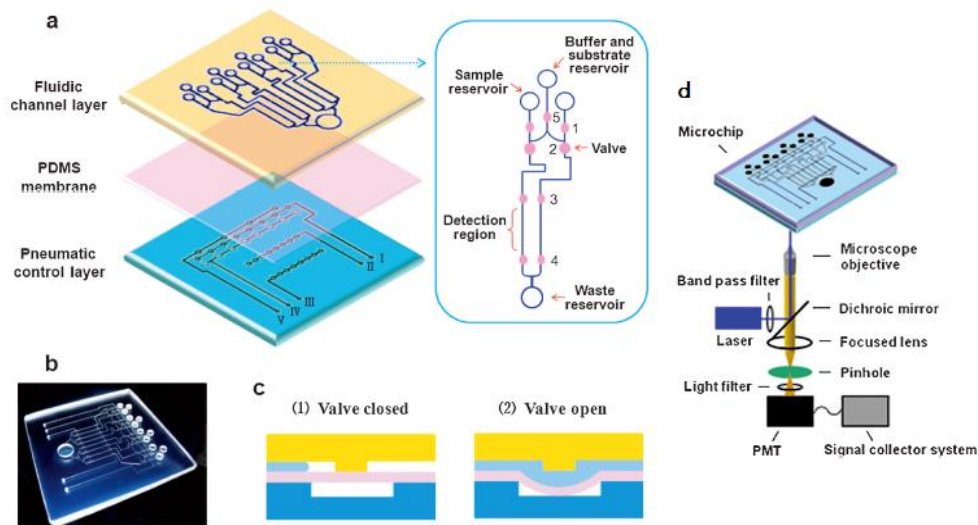


Figure 2-4 (a) Layout of the integrated microfluidic device for clenbuterol immunoassay. (b) Photograph of the prototype microfluidic device. (c) Cross-sectional view of microvalves on chip. (d) Scheme of the optical configuration of the confocal LIF scanning system. (Source: Jing Kong and Bingcheng Lin et al. 2009)

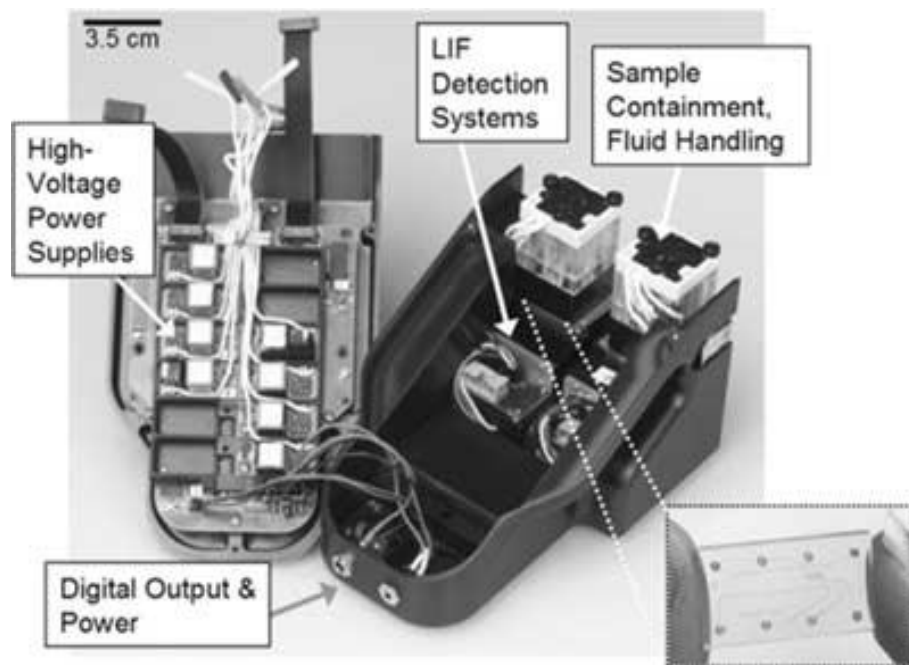


Figure 2-5 Image of IMPOD with hardware components. Inset shows glass microdevice used in performing immunoassays. (Source: Amy E. Herr and Anup K. Singh, 2007)

Another type of the fluorescence detection used in microfluidic applications is FP (fluorescence polarization) which detects the change in anisotropy caused by the slower rotation of a free label. FP gives a direct and nearly instantaneous measure of a tracer's bound/free ratio, even in the presence of free tracer. Figure 2-6 illustrates the FP principle. A single-plane fluorescence polarization light can be generated by installing two polarizing filters in the light paths of both excitation and emission in a fluorescent system. The intensity of FP light is proportional to the size of the fluorescent molecules and inversely proportional to the rotating speed of the molecules. In the solution, the rotation of the small molecules is very rapid, but the larger molecules become slower. Therefore, the emission light of the fluorescent-labeled small molecules is depolarized when the molecules are excited. However, when the fluorescent-labeled small molecules are bound to the antigen/antibody, the emitted light of the conjugates is obviously less depolarized due to the larger mass. Difference between these states is dependent on the number of bound molecules and the binding constant or affinity constant.⁷¹

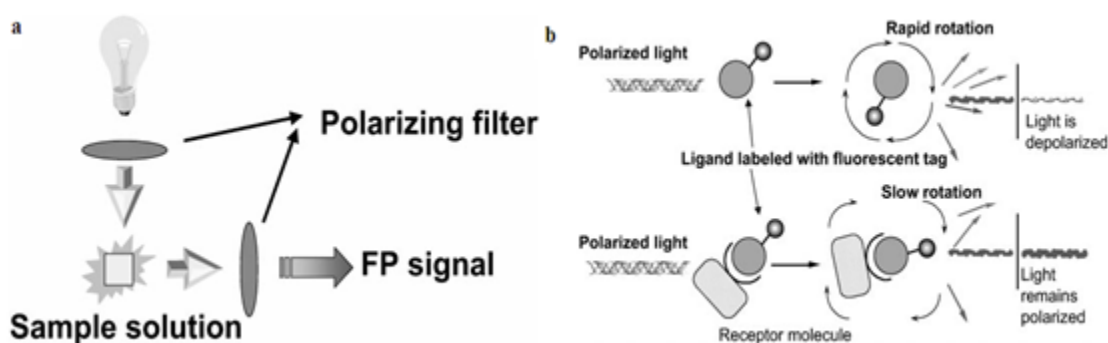


Figure 2-6 a) Illustration of a fluorescence polarization apparatus. b) Principle of the assay of binding reaction using fluorescence polarization. (Source: K. Kakehi and Y. Oda et al., 2001)

Vamsi K. Yadavalli and Michael V. Pishko⁷² demonstrated that fluorescence polarization can be used to reliably and accurately study binding events and detect analytes in microfluidic devices. A TRITC (tetramethylrhodamine isothiocyanate) labeled antibody was used to detect the polyaromatic hydrocarbon pyrene at 10-40 nmol. Tomoya Tachi and Yoshinobu Baba et al.⁷³ reported a microfluidic FPIA system composed of a microfluidic chip, a laser, a CCD camera and an optical microscope with two specially installed polarizers (one fixed and one rotatable). By using this system, they successfully carried out a quantitative analysis of theophylline in serum near the therapeutic range in 65 seconds.

2.3.1.2 Chemiluminescence detection

CL (Chemiluminescence) is another excellent optical detection method in microfluidics. Chemiluminescence is the light produced by a chemical reaction. The CL intensity is directly proportional to the concentration of a limiting reactant involved in the CL reaction. As a principle of the CL, reactants A and B react with an excited intermediate to form a product and emit the light which can be detected and analyzed by an optical detection system (Figure 2-7). The advantage of this technique is that the excitation light instrumentation is not required. Because of this advantage, the background interference can be eliminated.

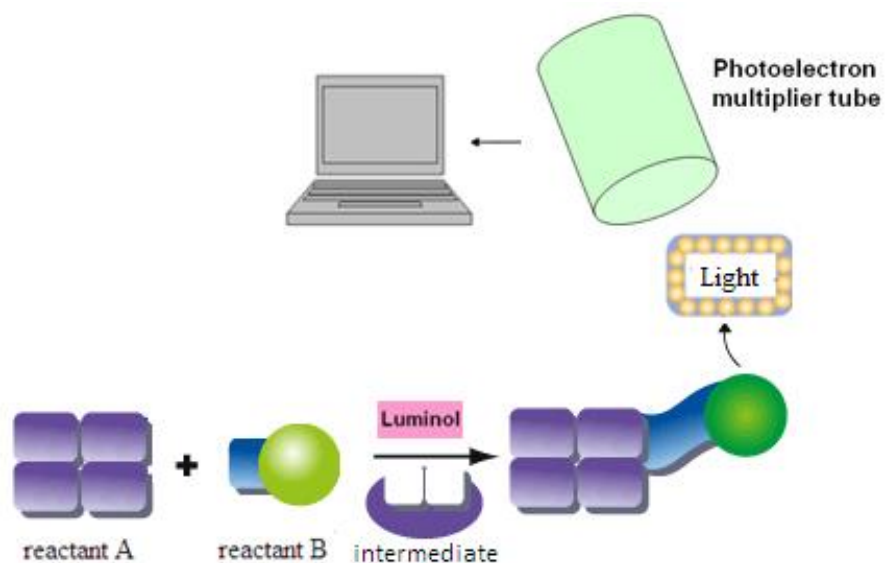


Figure 2-7 The principle of the Chemiluminescence detection method.

Yi-Ning Yang and Gwo-Bin Lee et al.⁷⁴ demonstrated a microfluidic chip integrated with pneumatic micropumps, micro-valves and vortex-type micromixers for CRP (C-reactive protein) measurement. The magnetic beads with CRP-specific DNA aptamers and bio-samples with CRP were placed in the reaction chamber. The target CRP was captured by the magnetic beads and the complex was attracted to the bottom of the microchannel using a magnet. After washing, the Anti-CRP antibody labeled with acridinium ester was added and interacted with the target CRP. Finally, a developer H_2O_2 was added for chemiluminescence. The chemiluminescence light signal was measured by using a luminometer. The entire reaction time is less than 25 min and the detection limit of the CRP concentration was 0.0125 mg/L.

Andrew J. de Mello's group⁷⁵⁻⁷⁶ reported a microfluidic chip integrated with the thin-film OPDs (organic photodiodes) for antioxidant capacity screening (Figure 2-8). The PDMS microchip comprised two inlets, mixing channel, a circular detection chamber and an outlet. The PO-CL reagent, dye, catalyst, hydrogen peroxide and sample were injected into the microchip and reacted at the detecting zone. In this study, the CL was based on hydrogen peroxide induced oxidation of an aryl oxalate ester which resulted in the formation of an electronically excited intermediate. When the fluorophore was added, the energy transferred to the fluorophore with concomitant emission of light. But during the reaction, antioxidants scavenged hydrogen peroxide and resulted in a decrease in CL emission. The OPDs detectors were applied to detect the chemiluminescence signal for determining antioxidant capacity. The whole detection system can be portable and has wider applications for chemiluminescence based point-of-care diagnostic tests.

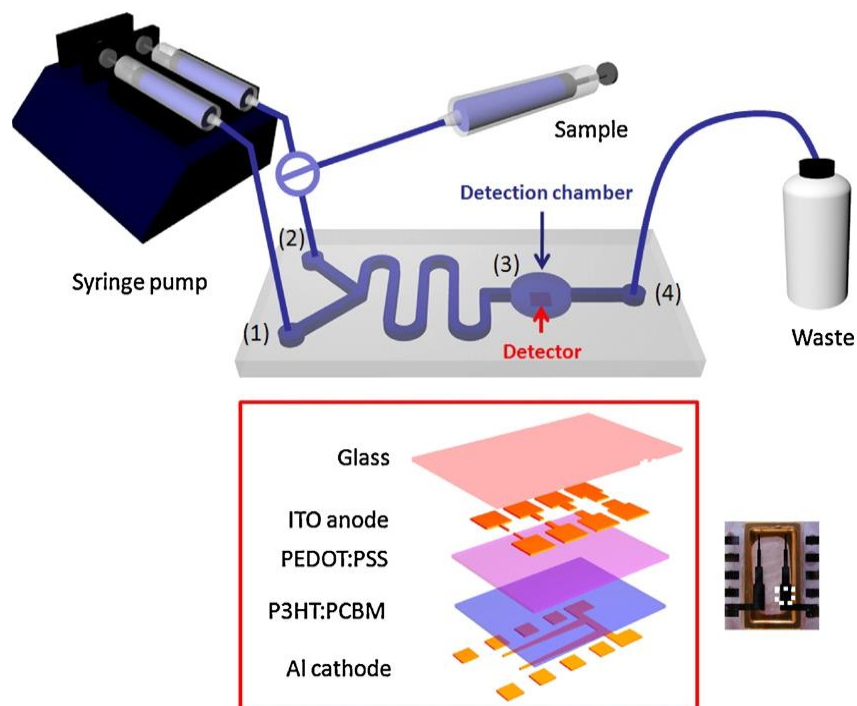


Figure 2-8 Schematic of the experimental set-up for on-chip antioxidant capacity screening. (Source: Xuhua Wang and Andrew J. de Mello et al., 2009)

Hui Huang and Xiao Yun Pu et al.⁷⁷ reported a rapid and sensitive chemiluminescence microfluidic immunoassay system based on super-paramagnetic microbeads for determination of AFP (alpha-fetoprotein). In their system, the microfluidic chip was fabricated by the CO₂ laser. Super-paramagnetic microbeads coated with AFP antibody were immobilized in the reaction chamber by

electromagnetism. After loading the sample and the HRP-labeled anti-AFP antibody, the sandwich immunoassay was carried out. Then, the Luminol and H₂O₂ were loaded into the reaction chamber to generate the chemiluminescence signal. With this system they performed AFP analysis in 20 min and the detection limit is 0.23 ng/mL.

2.3.1.3 Thermal lens microscope

TLM (thermal lens microscope) is a very sensitive detection method. Compared with the fluorescence detection method, the detection limit can reach zepto-mole to yocto-mole levels under the perfect conditions.⁷⁸ It is good at detecting the non-fluorescent samples. Sometimes, it needs very high sensitive detector to analyze the very small volume of the analyte on a microfluidic chip. Therefore, TLM is a powerful tool for the microfluidics. TLM is implemented by using a laser microscope. Two coaxial laser beams are introduced into a liquid sample under an optical microscope. The wavelength of the excitation beam is selected to coincide with an absorption band of the analyte. The wavelength of the probe beam is chosen so that the sample solution has no absorption (Figure 2-9). The temperature of the analyte in the confocal region increases because the heat is yielded by absorbing the excitation beam. For most solutions, the RI (refractive index) decreases with the high temperature. According to the proportional relationship among the laser intensity, the temperature distribution and the RI distribution, the RI distribution becomes a nearly Gaussian distribution because the laser intensity profile is nearly a gaussian distribution. This phenomenon forms a concave lens and is called ‘thermal lens effect’. The degree of the thermal lens which is measured by the probe beam is proportional to the number of analyte molecules in the confocal region.⁷⁹

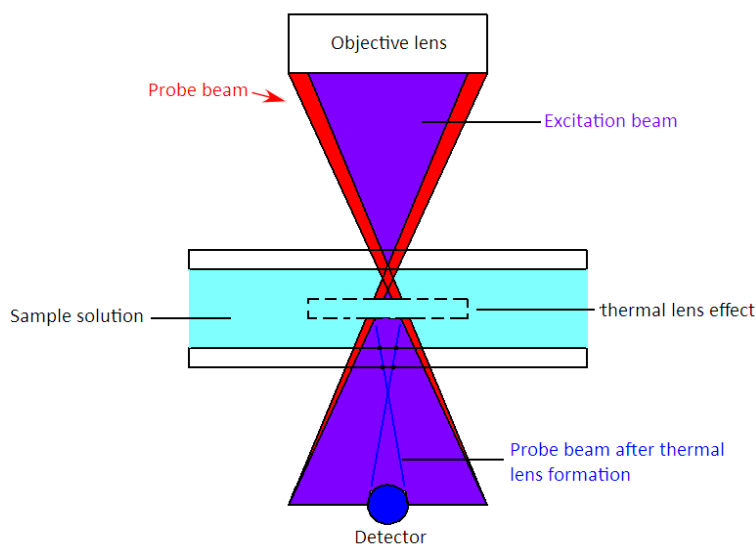


Figure 2-9 The schematics of the thermal lens microscope.

For example, Terence G. Henares and Hideaki Hisamoto et al.⁸⁰ reported a multiple micro ELISA system to simultaneously determine human, goat, and chicken IgGs by combining a capillary-assembled microchip and TLM detection method. The microchip had a PDMS plate with the lattice microchannel network. The plugged capillaries, the valving capillaries and the immuno-reaction capillaries were embedded into the microchannel network to form a flow controlling and immune reaction system. A Peltier device was used to open or close the valve. The thermal lens detector focused on the region of the immuno-reaction capillaries to detect the IgGs. The detection limit of 0.1 ng/mL IgGs (human, goat, chicken) was obtained in 30 min. Masaki Ihara and Hiroshi Ueda et al.⁸¹ developed a novel detection system that combined the merits of open-sandwich enzyme-linked immunoadsorbent assay, a microfluidic sensor chip system and a sensitive thermal lens microscope. In their work, OS-ELISA was performed in a microfluidic channel in which polystyrene microbeads were packed using an automated ELISA system. The microfluidic channel with a dam structure was used for retaining the microbeads (Figure 2-10). A small amount of the BGP, a biomarker for bone metabolism, was quantified by utilizing the thermal lens microscope. In a short analysis time (12min), detection limits of the total BGP-C concentrations in bovine and human serum samples were 17 and 10 nM, respectively.

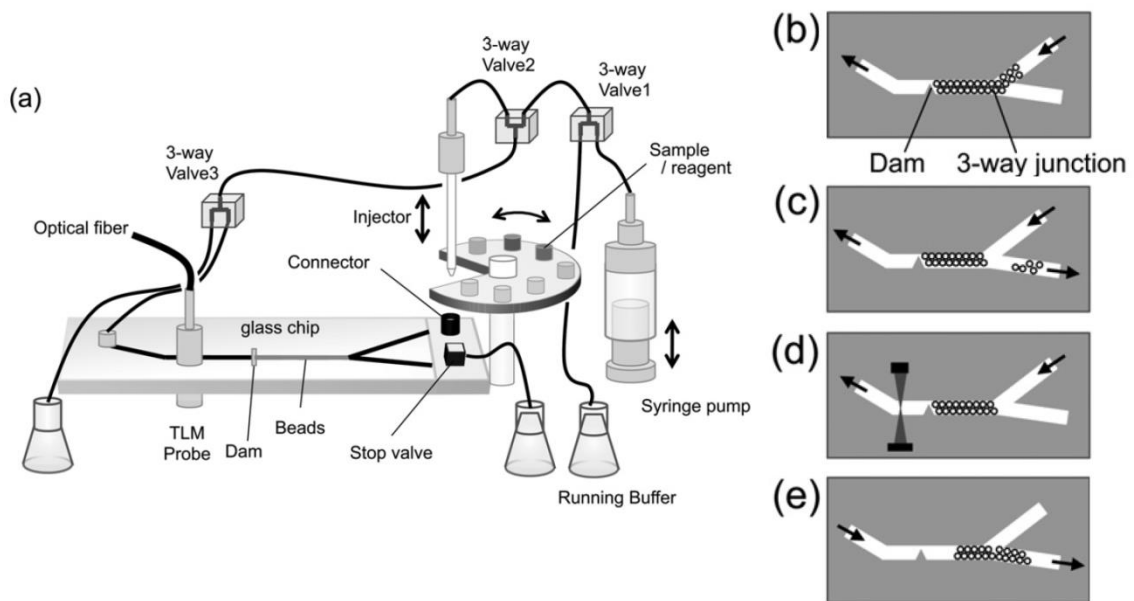


Figure 2-10 The micro-ELISA system. (a) A glass chip integrated with microfluidic channels was used for the OS-ELISA reaction. (b)-(e) Polystyrene beads with immobilized MBP-VL were

introduced and stored between a dam structure and the three-way junction. Extra beads were flushed away. The reagents were introduced into the microchip to form an immuno-complex on the beads. After washing, the substrates were applied and dye molecules produced by the enzyme reaction were detected by a TLM downstream of the dam structure. The microbeads after each assay were flushed by an inversed flow. (*Source*: Masaki Ihara and Hiroshi Ueda et al. 2010)

2.3.1.4 Surface plasmon resonance

Another detection strategy that widely used in optical microfluidics is SPR (surface plasmon resonance). A landmark paper involved in the SPR was published by Kretschmann in 1971.⁸² The 'kretschmann structure' lays a solid foundation for the SPR sensor. The operation principle and experimental configurations of SPR have been described in several review papers.⁸³⁻⁸⁷ Briefly, when a polarized light hits a prism covered with a thin film of metal at a specific (resonance) angle, SPR occurs. SPR effect is sensitive to the binding of analyte because the increase in mass causes a proportional increase in the refractive index at the interface between a thin metal film and an ambient medium. SPR provides a non-invasive, label-free approach for detecting the concentration of analytes, kinetics, and affinity in real time. Figure 2-11 shows the scheme of a typical experimental configuration for SPR instrumentation. The transduction surface is usually a thin gold-film (50–100 nm) on a glass slide, optically coupled to a glass prism through a refractive index matching oil.

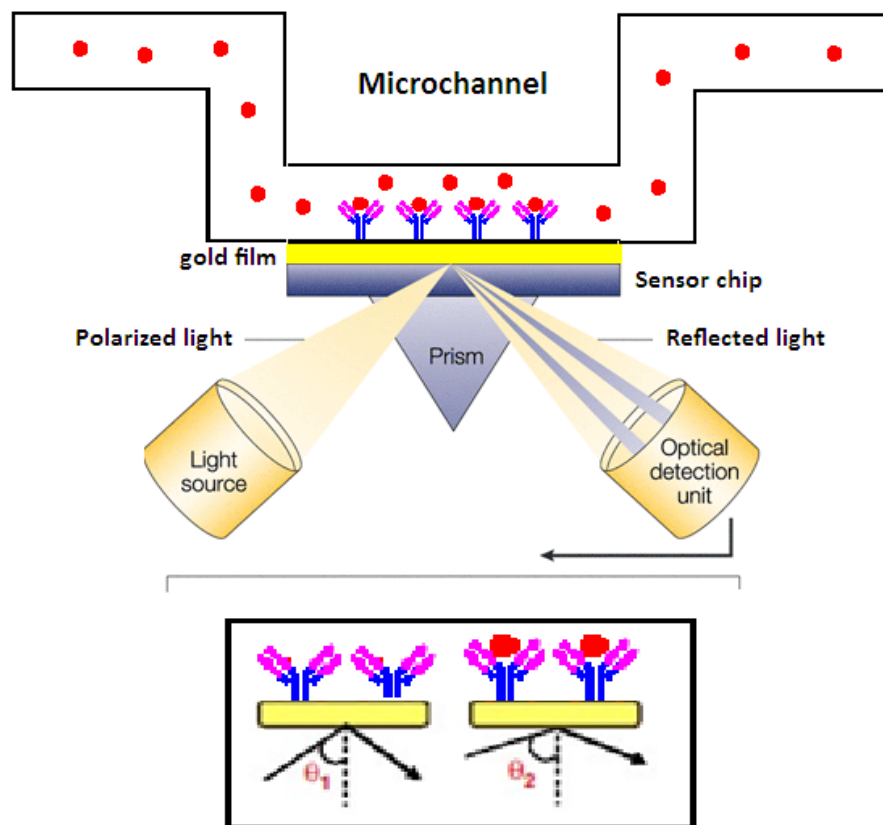


Figure 2-11 Schematic view of the SPR immunoassay technique.

Because of several advantages including high sensitivity, specificity and rapid response time, a great variety of SPR-based sensors have been developed since its introduction in the 1990s. Recently, C. Estmer Nilsson et al.⁸⁸ introduced a new approach using SPR for accurate quantification of influenza virus. Recombinant HA proteins (A/H1N1, A/H3N2 and B respectively) were immobilized on the dextran matrix of a sensor chip. By using a microfluidic system for reagents handling, a binding event occurred on the sensor surface. A change in SPR response was detected. In their study, the calibration curve range was 0.5–10 $\mu\text{g}/\text{mL}$ and the limit of detection was estimated as $<0.5 \mu\text{g}/\text{mL}$ for all three analytes. Lee et al.⁸⁹ developed a microfluidic system integrated with 2-D SPR phase imaging system for microarray immunoassays. In this work, the microfluidic device was composed of an arrayed sample/reagent delivering module and a micro-temperature control module. Using this system, the interaction of anti-rabbit IgG and IgG was successfully detected. A detection limit of $10^{-4} \text{mg}/\text{mL}$ for IgG was obtained. Changchun Liu et al.⁹⁰ developed a compact microfluidic-based biosensor flow

cell for SPR imaging. This biosensor flow cell consisted of a ‘hard’ plastic substrate (PMMA) coated with a SiO₂ thin film which was used as an adhesion intermediate layer and a ‘soft’ PDMS microfluidic layer which adhered to the SPR array chip. An immunoassay was successfully carried out on the microchip and the limits of detection of sulfamethoxazole and sulfamethazine were obtained as 3.5 and 0.6 ng/mL, respectively. Krishnamoorthy et al.⁹¹⁻⁹² used a surface plasmon resonance imaging (iSPR) label-free biosensor to detect surface binding events in a microchip which used electrokinetic flow focusing to selectively deliver samples over an array (Figure 2-12).

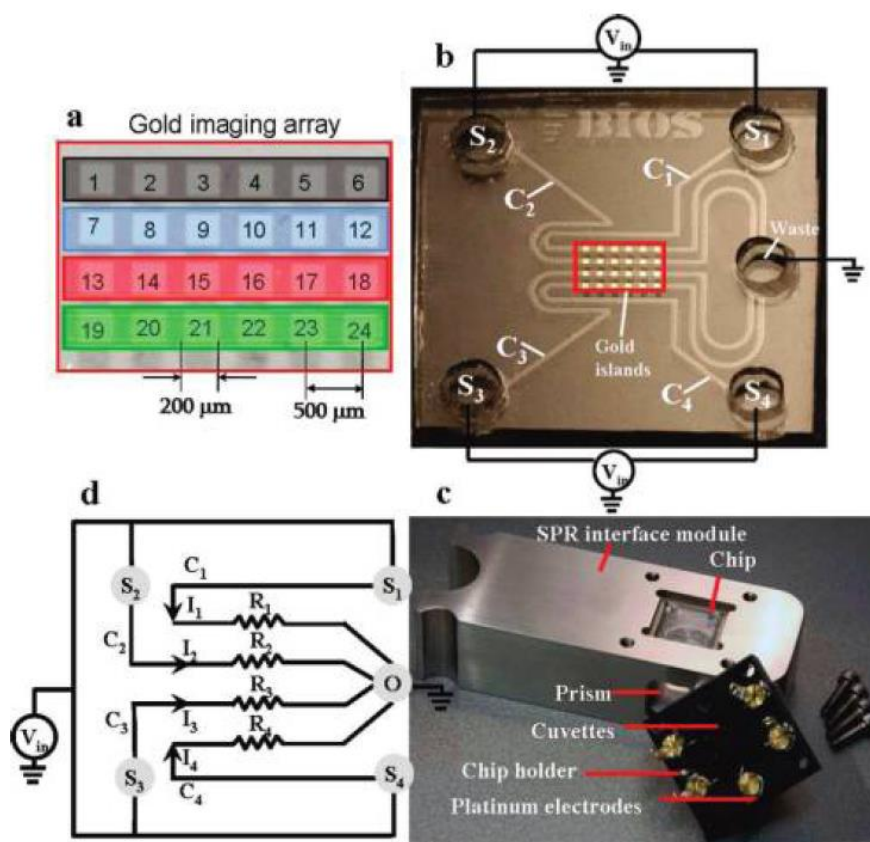


Figure 2-12 (a) Microarray of gold iSPR sensing islands. (b) glass-PDMS microfluidic chip. (c) The iSPR interface module with chip fixture with integrated platinum electrodes. (d) Electrical circuit. (Source: Krishnamoorthy et al. 2010)

By combining the EOF for sample transport and the electrokinetic focusing for sample guiding, an advantage of this approach was the ability to direct a single analyte to a specific ligand location in the microarray which could facilitate analysis parallelization. The SPR signal was changed and measured during sample focusing. In their study, they successfully analyzed the binding kinetics and affinity

during the biomolecular interaction. In addition, many commercial SPR systems have been introduced by different companies with various options and resolutions; BIAcore (Uppsala, Sweden), Nippon Laser Electronics (Hokkaido, Japan), Affinity sensors (Franklin, MA), IBIS technologies (Enschede, The Netherlands), Texas Instruments (Dallas, TX), Moritex (Japan), Aviv (Lakewood, NJ), etc.⁹³ SPR detection is a highly sensitive, labelling-free and real-time response detection method. However, the structure of the SPR device is complex, and a layer of metal (such as gold) must be deposited on the microchip. In addition, when doing experiments, the impact of the change of the temperature must be considered. Because the refractive index of the solution is sensitive to the change of the temperature, the accuracy of the detection may be reduced.

2.3.1.5 Absorbance detection

UV/visible absorption spectroscopy is a general optic technique. When a beam of light passes through the sample, the light absorption occurs because of the atoms or molecules taking away the energy from the light. It means that the transmission of light is reduced when passing through a sample. Generally, the absorbance of a sample is directly proportional to the optical path length of the sample holder and the concentration of the sample. Absorbance detection is used in macroscale analytical chemistry and laboratory diagnostics because of its simplicity and acceptable sensitivity. However, in the microscale, the absorbance of a sample is constant. If the optical path length is shortened greatly, the concentration of the sample must be high enough to be detected. The short optical path length limits the applications of this method due to micron-sized or nano-sized channel. Wanida Laiwattanapaisal et al.⁹⁴ performed an experiment on a portable microfluidic device to measure urinary albumin by monitoring the absorbance changes. For increasing the sensitivity of absorbance detection in a microfluidic chip, the PDMS chip was composed by two layers. The upper layer was a 2-mm thick PDMS containing the channel structure. A modified flow cell made from a polystyrene cuvette with a 1-cm path length and a total volume of 90 μL was incorporated into the lower, 6-mm thick PDMS layer. The optical path length was increased significantly in this way. With their proposed system, a calibration curve which was linear up to 10 mg/L, with a detection limit of 0.81 mg/L was obtained.

2.3.2 Non-optical detection

2.3.2.1 Electrochemical detection

Electrochemistry-based methods have played a major role in the microfluidic detection. The electrochemical detection can be used to measure the concentration of the analyte by converting the analyte's chemical signal into the electrical signal via the electrodes. According to the principle of the electrochemical detection method, there are three basic categories of the electrochemical techniques: amperometry, potentiometry and conductometry.

Amperometric detects the current signal generated by the redox reaction on the electrode. A three-electrode amperometric electrochemical concept is shown in Figure 2-13. The detecting sensor is composed of three electrodes (working electrode, reference electrode and auxiliary electrode). A polarizable electrode is used for the working electrode on which an electrochemical reaction takes place. The reference electrode is a potential standard to supply a constant potential for introducing the electrochemical reaction on the working electrode. When a certain potential is applied to the working and the reference electrode, the redox reaction occurs. The reaction generates the current and can be measured between the working electrode and the auxiliary electrode. The current is proportional to the concentration of the analyte.⁹⁵ Amperometric approach is a simple technique. Miniaturization and integration can be easily achieved by creating a three-electrode system on the microfluidic chip.

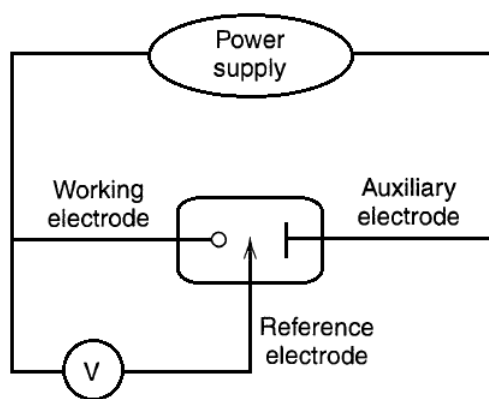


Figure 2-13 Three-electrode cell and notation for the different electrodes.

Recently, Sung Ju Yoo and Sang-Hoon Lee et al.⁹⁶ demonstrated an electrochemical-based microfluidic chip for rapid and quantitative detection of urinary HA (hippuric acid) in human urine (Figure 2-14). In their study, all the complicated HA detection processes were integrated on a single

microfluidic system. The metal three-electrode layer was patterned and deposited by chemical etching process on a glass slide. A PDMS microfluidic channel was bonded on this glass. It had a PRC (polybead reserving chamber) which was used to store beads coated with anti-HA antibody, a detection chamber and a dam which was used to prevent bead spillover. Antigens (HA and Fc-Lys-HA) were injected into the microfluidic channel and competitively bound with the antibody (anti-HA) coated on the beads. After the reaction, the unbound antigens passed through the dam and entered into the detection chamber. The unbound Fc-Lys-HA caused the redox reaction on the electrode and the change of the current which was correlated with the HA concentration was measured. They could detect the HA concentration in the range of 0-40 mg/mL.

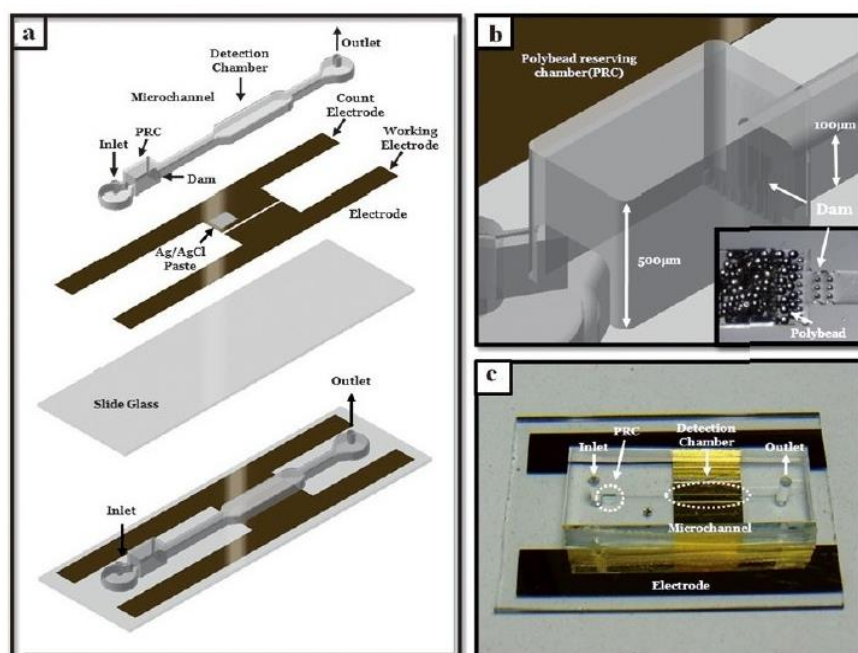


Figure 2-14 (a) Schematic diagram of the microfluidic immunoassay system. (b) The chamber holding the polybeads. (c) A photograph of the immunoassay microchip. (Source: Sung Ju Yoo and Sang-Hoon Lee et al. 2009)

Using the micromachining technology, the electrodes are easily miniaturized. The sizes of the electrodes are commonly on the order of micrometers and the nanometer sizes have also been achieved. Therefore, the electrochemical detection approach can be integrated into the microfluidic systems where the compactness and the portability are important. I-Jane Chen and Erno Lindner⁹⁷ reported a passive pump driven microfluidic system integrated with micro fabricated electrodes as electrochemical sensors to detect the analyte of the hexacyanoferrate (II) (Figure 2-15). Cheng-Yu

Lin and Gwo-Bin Lee et al.⁹⁸ developed a hand-held system for detection of urinary proteins. Their system was composed of a control circuit, an electromagnetic valve, an air compressor and a microfluidic chip which was integrated with a microfluidic control module and a micro electrochemical module. The microfluidic control module consisted of a two-way, spiral-shape micropump which could transport the urine samples to the sensing regions. The electrochemical sensing module had three sensing electrodes. The detection limits of the lysozyme and albumin measurement were experimentally found to be 0.1ppm.

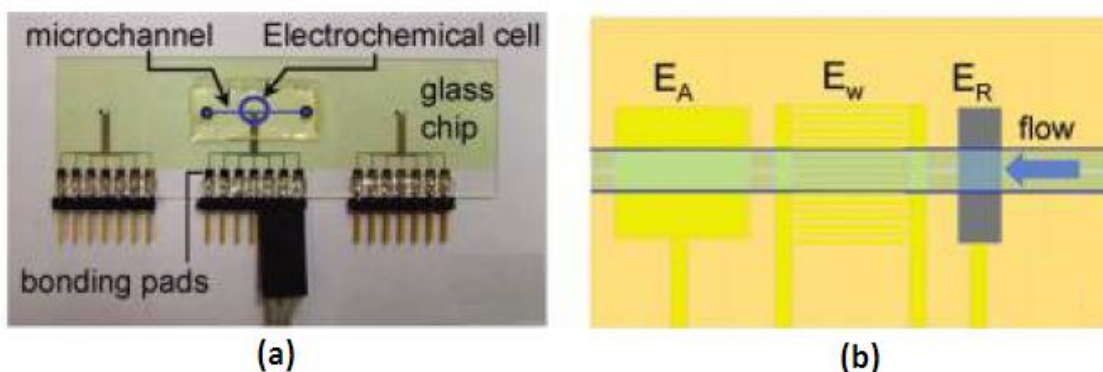


Figure 2-15 (b) Photograph of a glass slide with three electrochemical cells. (c) Schematic representation of the reference (ER), interdigitated working (Ew), and counter electrodes (EA). (Source: I-Jane Chen and Erno Lindner, 2009)

Potentiometry is used to determine the analytical concentration by detecting the electrical potential of an electrode. It consists of an ion-selective electrode and a reference electrode. The voltage difference between the ion-selective electrode and the reference electrode is measured as the signal. The relationship between the ion-selective electrode potential and the ion concentration of the analyte is expressed by the Nernst equation. The potential is proportional to the logarithm of the ion activity. Therefore, the ion-selective electrode must use ion-selective membranes to achieve charge separation between the sample and the electrode surface. Karin Y. Chumbimuni-Torres and Eric Bakker et al.⁹⁹ firstly demonstrated a polymer-membrane-based potentiometric method for nanoparticle-based protein detection. A silver ion-selective electrode was used as an effective transducer for sandwich immunoassays. The target mouse IgG antigen was captured by the primary anti-mouse IgG antibody modified gold substrate. The immunocomplex captured the gold nanoparticles labelled the secondary anti-mouse IgG antibody. After that, the catalytic deposition of silver on the conjugated Au nanoparticles was carried out to enhance the mouse IgG signal. The precipitated silver was

oxidatively dissolved with hydrogen peroxide to yield electrolyte backgrounds for the potentiometric detection of the released silver ions with the ISE. They obtained a detection limit of around 12.5 pmol of IgG in 50 uL sample.

Conductometric detection approach depends on the difference of the electrical conductivity between the background solution and the analyte. Conductometric detection is performed in two modes either with or without direct contact of the sensing electrodes with the background solution and the sample components. Generally, the detection limit of this approach can reach 10^{-6} to 10^{-8} mol/L. The structure of the conductometric detection is simple: only a pair of electrodes is necessary. This simple structure facilitates miniaturization and integration. Detection based on the conductometry has been used in microfluidic systems for foodborne pathogens¹⁰⁰ (the detection limit of the Salmonella, E.coli O157:H7 and E.coli biosensors are 8.39 ± 0.6 , 7.9 ± 0.3 and 7.59 ± 0.3 CFU/mL, respectively.), hepatitis B surface antigen¹⁰¹ (the detection limit of HBsAg is 0.01 ng/mL.), interleukin-6¹⁰² (the detection limit is 5 pg/mL.) and Escherichia coli¹⁰³ (the detection limit is 0.5 CFU/mL).

Amperometric detection method has some advantages including simple, low background noise. It is the most popular electrochemical detection method in the microfluidic immunoassay system. However, it is not the universal method. It requires the analyte has the electrochemical activity; otherwise some additional substances which have the electrochemical activity must be introduced to the system for the indirect detection. Potentiometric detection method has the specificity because it uses the ion-selective membrane to achieve charge separation. However, the selective membrane is hard to integrate into the microfluidic system that greatly limits the application of this method in the microfluidic immunoassay. Conductometric detection method is a universal detection method. However, it lacks the specificity. According to the principle, the conductivity between the background solution and the analyte must be sufficiently different. If there are two kinds of the analytes which have the similar conductivity, this method can't distinguish them.

Impedimetric detection method is the similar to the amperometric or conductometric detection method. Usually, it uses either the two-electrode or the three-electrode concept. The difference between them is that the AC is used in the impedimetric detection. Compared with the amperometric or conductometric detection method, the electrolysis of the electrode can be eliminated by using the AC. In a microfluidic system, with the antibody-antigen interaction or reaction, the variation of the impedance can be easily measured by an impedimetric analyzer. However, like the conductometric detection method, the sensitivity depends on the difference of the impedance between the background

and the analyte. Madhukar Varshney and Steve Tung et al.¹⁰⁴ demonstrated a microfluidic flow cell integrated a label-free impedance biosensor for the direct detection of *Escherichia coli* O157:H7 in food samples. MNAC (magnetic nanoparticle-antibody conjugates) were embedded in the microfluidic flow cell to capture the bacterial cells. The microelectrodes were coated on the microfluidic chip to form the impedance biosensor. The impedance changes were recorded by an impedance analyzer during the immune reaction. In their study, 1.6×10^2 cells could be concentrated from a sample volume of 5 mL, with a detection limit of 8.4×10^4 cfu/mL. In Yu-Cheng Lin's group, they developed a new, simple and sensitive immunoassay that used the impedance variation caused by silver nanoparticles (AgNPs) coated with an antibody.¹⁰⁵⁻¹⁰⁶ In their study, the electro-microchip was composed of the two parallel gold electrodes and an reaction well. The first antibodies were immobilized on the glass slides and the test antigen, the washing buffer, the PBT and the silver-conjugated second antibodies were introduced into the microchip sequentially. The AgNPs made short circuit between two electrodes and decreased the impedance. The variation of the impedance was measured during the immune reaction. The antigen detection limit is 10 ng/mL.

2.3.2.2 Quartz crystal microbalance

When applied the electrical field on the quartz crystal, it produces the mechanical deformation. Conversely, when applied the mechanical stress on the quartz crystal, it generates the electrical field. This phenomenon is called 'piezoelectric effect'. The QCM (quartz crystal microbalance), also called 'micro weighing instrument', is a sensitive mass microbalance based on the piezoelectric effect for measuring the change of the mass on a surface and works well without using any label. The detection limit of this method is up to 10^{-13} g.¹⁰⁷ Stephanus Böttgenbach et al.¹⁰⁸⁻¹⁰⁹ demonstrated a miniaturized system for the determination of protein A by integrating a QCM sensor and a PDMS-based microfluidic cell. In their study, the AT-cut quartz with the gold electrodes was used to form the quartz resonator. The PDMS flow cell was bonded to the quartz surface. The protein A was immobilized on the gold electrode. The anti-protein was introduced into the flow cell and bound with the protein A. The frequency shift was monitored by a frequency and the measured values were recorded online with software. The detection limit for protein A is 1 mg/mL. Recently, Thomas Frisk and Goran Stemme et al.¹¹⁰ reported a novel microsystem which absorbed airborne narcotics molecules and performed a liquid assay using an integrated quartz crystal microbalance (QCM). In this study, the microsystem consisted of four parts. A quartz crystal fixed to a silicon chip and covered by a protective polymer cap by using double-sided vertically conductive adhesive foil. The

silicon chip gave rigid support to all device parts and supplied microchannels for transport of buffer liquid. It defined a robust air–liquid interface where airborne molecules could become absorbed into the liquid. The anisotropically conductive property of the foil provided electrical connection between the silicon chip and the QCM, and electrical isolation to the rest of the system. The polymer cap gave protection to the QCM from external influences without making any mechanical contact to it. The quartz crystal was a shear mode electromechanical oscillator, with the resonance frequency dependent on the mass of the material attached to its surface (Figure 2-16). The microsystem was based on a QCM with a competitive immunoassay. They successfully measured 100–200ng of narcotics samples with a sensitivity ranging from 6–20 ng Hz⁻¹. QCM has been used for detecting the different analytes including C-reactive protein¹¹¹ (the detection limit is 0.13 ng/mL), prostate specific antigen¹¹² (the detection limit is 0.29 ng/mL). The QCM is a label-free detection method which has a potential to be widely used in the microfluidic detection. It offers some advantages including high sensitivity, real-time readout, low cost. In addition, the QCM not only can detect the mass changes of the analyte but also can provide the structure information of the analyte. However, one of the biggest challenges for the development of QCM microfluidic devices is how to coat the analyte on the detection surface evenly; otherwise it is hard to obtain the accurate result and the repeatability.

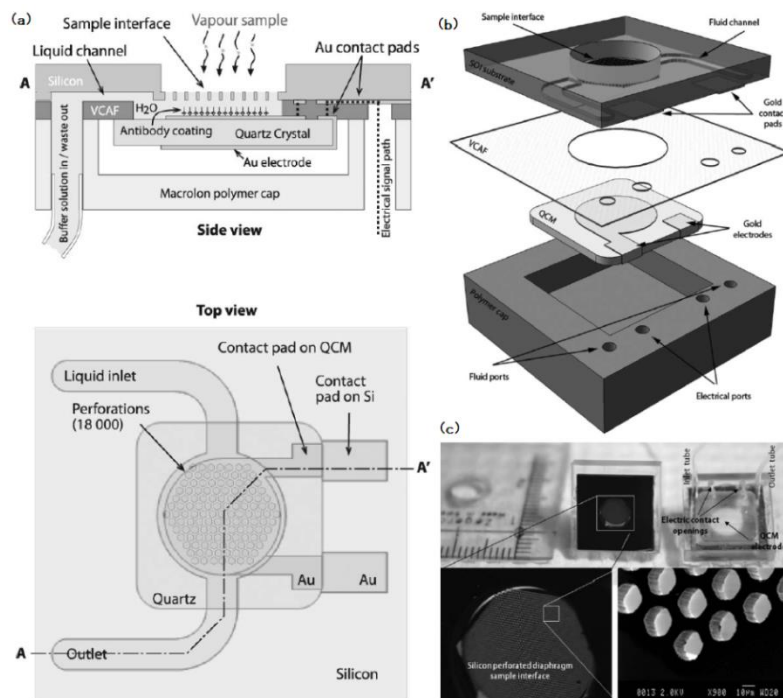


Figure 2-16 (a) Schematic cross-sectional (top) and top view (down) of the microsystem. (b) Exploded to scale view of the designed four-component system: the silicon substrate, the VCAF, the quartz crystal and the protective polymer cap. (c) Front and backside pictures of two devices. The QCM crystal is visible through the polymer backside cover. (*Source: Thomas Frisk and Goran Stemme et al. 2008*)

2.3.3 Summary

Generally, the detection system in the microfluidic devices must have high sensitivity, high response time, and minute size. Currently, the detection systems for the microfluidic devices are usually bulky and expensive. It is very difficult to integrate the detection system into a portable device if the detection system requires microscope, power supply, laser and pump.

Optical detection still is the most powerful technique for analysis in microfluidic devices. Generally speaking, fluorescence detection method is the most popular optical method for quantifying analyte in the microfluidic systems. It has high sensitivity, high response time and high selectivity due to fluorescent labeling techniques. The key to get the high qualitative fluorescent signal is to minimize the background light noise as much as possible. Therefore, material selection and sample purification are very important. Profiting from the laser diode and the miniaturized CCD sensor, fluorescence detection method can be easily integrated and miniaturized into a portable microfluidic device. Recently, LEDs¹¹³⁻¹¹⁶ as an excitation light and COMS image sensor¹¹⁷ are used for fluorescence detection to decrease the cost. They may be developed into a cost-effective ways of detection in the microfluidics. Chemiluminescence (CL) detection method is generally acknowledged to be a high sensitive method which can be comparable to the FIA method. The biggest benefit of this technique is that the excitation component, beam splitter and filter are not required. Compared with the FIA, CL detection method is much easier to integrate and miniaturize. Just a detector fixed at the reactor cell in the microchannel can accomplished the detection. Therefore, the design of the reactor cell in the microchannel is crucial to the whole system. On the one hand, the analyte and the antibody/antigen require high efficient mixing and full reaction in the reactor cell. On the other hand, the reaction system may influence the quantification of the detection, such as reaction accompanied by gas production. SPR detection method is growing rapidly, mostly because it is a free labelling and real-time response detection method, and the background noise is virtually eliminated. SPR detection method is feasible for miniaturization and portability.¹¹⁸⁻¹²¹ However, the structure of the SPR device is complex, and a layer of metal (such as gold) must be deposited on the disposable microchip, thus

increasing cost. Thermal lens microscopy (TLM) is a kind of very sensitive photothermal conversion detection technique. It is a promising method for detecting analysis in liquids. The detection limit was demonstrated to be as low as the 0.1 nM level. However, TLM has a low selectivity so that it cannot distinguish the changes of the temperature and light intensity caused by different analytes. Therefore, it is hard to be applied in the complicated detection. Besides, Integrating and miniaturizing the TLM method into a microfluidic device is a big challenge.

Non-optical detection is another important branch of detection methods for the microfluidics, especially the electrochemical detection method. Because the structure of electrochemical methods is simple, the electrochemical-based microfluidic system can be much easily miniaturized and integrated by the micromachining technology. However, the major disadvantage of this method is the interference caused by the components such as the electronic circuits, the electrodes and the microchip. In the liquid environment, because of the electrolysis, the bubbles are easily generated and will influence the result. The electrochemical detection depends on detecting the change of the current or the voltage. Therefore, compared with other detection methods, the background noise of the electronic circuits impacts the detection limit greatly in the electrochemical detection method. The QCM is a potential detection method in the microfluidic immunoassays due to the high sensitivity, the real-time readout and the low cost. However, how to coat the analyte on the detection surface evenly is a big challenge.

Although many microfluidic technologies have the potential, most of them are operated by well-trained technicians and require additional off-chip supporting units, such as fluid controlling systems, power and detection systems. Significant advancement in this area is required, and much more work remains to be done.

2.4 Optical detection in microfluidic flow cytometry

As we mentioned above, the most commonly observed form of optical detection is fluorescence, because of its high sensitivity and the ease of integrating a label. The optical system of the flow cytometry has two main functions: illumination and collection (detection). For the illumination, traditional flow cytometers are dependent on lasers which are used as an excitation source. Air-cooled gas lasers have been integrated into flow cytometers for years. The argon-ion and helium–neon lasers are the most prominent examples. In most commercial flow cytometers, the light excitation system is a single-color system. However, the single-color flow cytometer has some limiting aspects. First,

single excitation wavelength limits the fluorochromes and fluorescent proteins that can be utilized for cell detection and monitoring. In addition, double-labeling of cells with two different fluorescent markers, which would allow for such experiments is precluded. Second, single excitation light does not afford the opportunity to cross correlate acquired data, which can enhance cell detection accuracy, especially for the situations of elevated background noise that occur when tissue auto-fluorescence is high, or for minimally fluorescently marked cells. Therefore, dual-colors or multi-colors excitation system is developed in the commercial flow cytometers. These flow cytometers employ multiple lasers that excite up to different fluorescent dyes. However, all commercial flow cytometers without exception use two or more different lasers, dichroic mirrors, optical filters or photo detectors in the system. This possesses some drawbacks. First, it is well known that the laser will generate high levels of heat. The cooling system must be prepared for lasers. Second, more components mean the huge size, weight and cost. This is the key reason that today's flow cytometers are still bulky and costly, thus having only limited use for point-of-care applications. Third, more lasers mean the huge energy consumption. Recently, LEDs as an excitation light are used for fluorescence detection to decrease the cost. Compared with lasers, LEDs suffer from the disadvantage of non-collimated emission. However, they are still used in compact optical devices due to their low cost. The new generation of LEDs exhibit very high output power covering the whole visible wavelength range and even UV light. LEDs are the most effective light sources available and require only low-power driving currents. These advantages, combined with their compact dimensions, mean that they are perfectly suitable for integration into lab-on-a-chip devices. They may be developed into a cost-effective ways of detection in the microfluidic flow cytometer. Light signals are generated when particles pass through the laser beam in a fluid stream.

In recent years, fluorescent detection is the most powerful technique for analysis of cells in flow cytometers.¹²²⁻¹²⁴ For fluorescent detection, the excitation light source, optical filters and the photo-detectors are the most important components. Usually, laser is used as the excitation light source due to the ability of generating high-quality and well-focused laser beam. Photomultiplier tubes are used as the photo-detector because of its high sensitivity. Miniaturized fluorescent detection prototypes have been reported.¹²⁵⁻¹²⁷ For example, Kang et al.¹²⁸ reported a particle counting and sorting system based on the fluorescence detection for lab-on-a chip applications. However, these optical systems were still large and costly. Additionally, these prototypes have only one excitation light source and can detect only one kind of fluorochromes, restricting the applications significantly. Recently, a dual-color fluorescent detection system is developed to enhance the applications of microfluidic flow

cytometer. Zhong et al.¹²⁹ developed a two-beam, two-channel detection flow cytometry (T³FC) system which could realize the cell analysis of two different dyes. Yang and co-workers¹³⁰ also demonstrated a compact, high-sensitivity, dual-color flow cytometer (HSDCFM) for detecting specific bacterial cells. In their study, a method of labeling two dyes on one cell was used. The two different dyes were excited by using one laser and the two emission lights were captured by two photo-detectors. However, the high-cost, high-power consumption, bulky volume, heavy weight and complicated multi-dye staining protocol limit the applications of their flow cytometer. Generally, to realize dual-wavelength detection, it is a great challenge to miniaturize and integrate two sets of optical components (i.e., excitation light source, photo-detector and optic filters) into a limited space. To overcome these problems, the laser combined with optical fiber is used to reduce the light pathway. Tung et al.¹³¹ introduced a microfluidic flow cytometer based on the solid-state lasers and PIN-based photo-detectors to realize dual-wavelength detection. Optical fibers were used to transmit the laser beam to the detection zone and to collect the emission light from the fluorescent particles. Golden et al.¹³² also developed a microfluidic flow cytometer based on inserted optical fibers for counting microspheres. Optical fibers inserted into the microchannels provided two excitation lights. Two emission collection fibers were connected to PMTs through a multimode fiber splitter for detection. Although this approach utilized embedded fibers which can lead to a significant reduction of the size of flow cytometer, two lasers had to be used. Moreover, using embedded optical fiber on the chip increases the cost and the complexity of the chip fabrication.

2.5 Concluding remarks

A portable flow cytometry device is of importance in many on-site tests. As known that for a real portable flow cytometry device, the space is limited. However, current microfluidic flow cytometry devices do not take the space into account, their space is unlimited. None of current microfluidic flow cytometry devices can reach the requirement of portability. From the above reviews, it is clearly shown that most current microfluidic flow cytometry systems are micro- only on the microfluidic chip, the rest components are still bulky and expensive. For the fluidic control system, all of the current microfluidic flow cytometry systems are using the external mechanical pumps, hence tubes have to be used for connecting the pump and the flow cytometry system. Moreover, the reagent consumption of their system is huge due to the use of external tubes. In order to realize the flow focusing, the structure and the fabrication of the microfluidic chip are getting more and more complicate, which prevents the mass production of the microfluidic chip. The use of Lasers and

PMTs in the optical detection system result in a high cost. To overcome all the drawbacks aboved, innovations of proposed microfluidic flow cytometry system emerge to:

- Reducing the total size of the current microfluidic flow cytometry system;
- No valves, tubes and external pumps;
- Reducing the cost;
- Reducing reagent consumption;
- Mass-production of each subsystem;
- Simplifying the optical components and alignment.

Chapter 3

Study of Electrokinetically-induced Pressure-driven Flow in a T-shaped Microfluidic Chip

3.1 Introduction

As known that the biological cells such as RBCs (red blood cells) and WBCs (white blood cells) are very difficult to be driven in a microchannel by the electrokinetical force due to the surface charge change of the cells or the pH value change of the liquid. Moreover, the cells could be killed or destroyed under the electric field. Although these shortcomings can be eliminated by using the pressure-driven flow, it still exists some concerns. Generally, the pressure pumping forces are supplied by a syringe pump or other mechanical pumps which cannot be integrated into the microfluidic flow cytometry device. Besides, the pipes and valves are inevitably used between the microfluidic chip and the pumps, resulting in sealing and operating difficulties. Furthermore, the requirement of these external equipment will significantly increase the volume of the sample/ reagent.

In this chapter, a novel approach is introduced for generating a continuous pressure-driven flow and transporting the particles or biological cells in the T-shaped microchannel by using the electrokinetically-induced pressure-driven flow. Thus, the shortcomings of the electrokinetical force and the pressure pumping force are avoided when is employed individually. This is the fundament of this microfluidic flow cytometry device. Numerical and experimental results are reported to study electrokinetically-induced pressure-driven flow.

3.2 Principle of electrokinetically-induced pressure-driven flow

In this study, a novel method is put forward to generate the electrokinetically-induced pressure-driven flow in a T-shape microchannel. The schematic diagram of the proposed method is shown in Figure 3-1. The system is placed horizontally on a lab table surface. The main objective is to generate continuous pressure-driven flow in the vertical channel. The fluidic control system consists of a T-shaped rectangular channel, three cylindrical reservoirs initially with the same fluid level. The liquid in the microchannel is assumed as an incompressible, newtonian, symmetric electrolyte with constant density and viscosity. All the three reservoirs, A, B and C, are open to air and have atmospheric pressure. The channel wall is uniformly charged with the zeta potential, ζ . The channel A-B is used as

an electroosmotic pump which can be generated by applying the DC power between the reservoir A/B and point O. The direction of the EOF (electro-osmotic flow) is towards the reservoir A/B. Because of the flow continuity, point O has negative pressure that induces a flow from reservoirs A and B to point O and hence generates a continuous pressure-driven flow in the vertical channel from reservoir C.

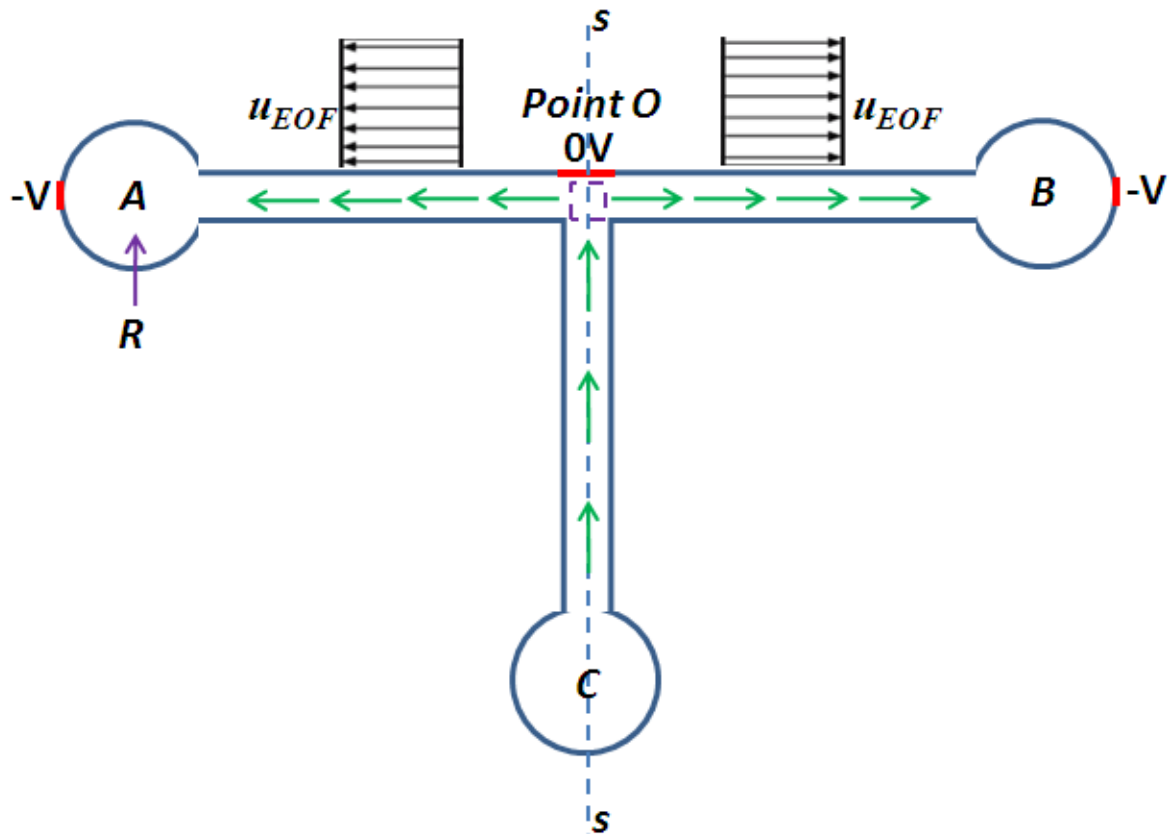


Figure 3-1 Schematic diagram of the proposed method to generate electrokinetically-induced pressure-driven flow. The s-s is the central line of the microchannel. The particles/cells are loaded in reservoir C. Reservoirs A and B contains initially the buffer solution. The red lines show the position of the electrodes.

Once the electric fields are applied on the transverse microchannel, the liquid in the purple frame (Figure 3-1) will be sucked out and flows into the wells A and B due to the EOF. The flow direction is from point O to both reservoirs A and B, thus the point O has the negative pressure. However, according to the fluidic continuity, the purple frame cannot be empty. The liquid in the vertical channel will move into the purple frame to fill it. Thus, a pressure gradient is generated between the

reservoir C and the point O. This pressure gradient is capable of generating a continuous electrokinetically-induced pressure-driven flow in the vertical channel. Compared with current microfluidic chips which are used in the fluidic control system, it is clearly shown that without any moving part and syringe pump, the pressure-driven flow can be generated in the proposed microfluidic chip. When loading the sample in the reservoir C, the particles/cells will flow into the vertical microchannel due to the pressure drop generated between the reservoir C and point O. The different kinds of the particles/cells can be detected by using the optical method when particles/cells pass through the detection zone in the vertical microchannel. This is the fundament of the microfluidic flow cytometry system in my study.

3.3 Numerical study

Numerical study was done to prove the theoretical analysis. In the numerical study, COMSOL MULTIPHYSICS was used to solve this numerical model. 800000 elements or more were used in all simulations to avoid the grid dependence. The numerical studies consisted of three main parts. In the first part, the effectiveness of the proposed method of generating electrokinetically-induced pressure-driven flow in the T-shaped channel is investigated. In the second part, the optimized chip design was studied to eliminate the influence of the pressure-driven back flow which caused by the hydrostatic pressure difference among reservoirs A, B and C. In the third part, the motion of the particles was studied.

3.3.1 Physical modeling

- *Electric field*

When the electrical potential, ϕ_e , is applied at reservoirs A, B and Point O, the applied potential through the system is governed by Laplace's equation.

$$\nabla^2 \phi_e = 0 \quad (3-1)$$

Once the electrical field is known, the local electric field strength can be calculated by

$$\vec{E} = -\vec{\nabla} \phi_e \quad (3-2)$$

The zeta potential at the non-conducting channel wall ζ_w is constant and the value depends on the properties of the solid material and the liquid solution. According to Helmholtz–Smoluchowski formula, the electro-osmotic flow velocity is

$$\vec{u} = \vec{u}_{eo} = -\frac{\varepsilon_0 \varepsilon_r \zeta_w}{\mu} \vec{E} \quad (3-3)$$

where ε_0 and ε_r are the dielectric constant in vacuum and the dielectric constant of the solution, respectively. The electro-osmotic velocity boundary condition is applied at the walls of the channel A-B. The non-slip velocity boundary condition is applied at the other walls where the flow is caused by the induced pressure. The boundary conditions of the electric field are

$$\begin{cases} \phi_e = \phi & \text{at reservoirs A and B} \\ \phi_e = 0 & \text{at Point O} \end{cases} \quad (3-4)$$

- *Velocity field*

The velocity field in the system is governed by the continuity equation and the Navier-Stokes equations.

$$\nabla \cdot \vec{u} = 0 \quad (3-5)$$

$$\rho \vec{u} \cdot \nabla \vec{u} = -\nabla P + \mu \nabla^2 \vec{u} \quad (3-6)$$

where ρ and μ are the density and viscosity of the liquid, u is velocity, P is the pressure gradient.

For analysis, the following parameters are used in the numerical simulation:

- For convenience, the channel depth is fixed at 25 μm ;
- The length of horizontal channel is fixed at 1cm;
- The width and length of vertical channel are fixed at 100 μm and 5 mm, respectively;
- The width of horizontal channel is allowed to vary from 25 μm to 300 μm .
- The work solution is water. The density of water ρ is 1000 kg/m^3 , the viscosity of water is μ is 10^{-3} $\text{kg/m}\cdot\text{s}$, the relative permittivity of water ε is 80;
- The zeta potential ζ is -0.04V;

3.3.2 The flow field in the T-shaped microchannel

Equations (3-1), (3-2) and (3-3) subjected to boundary conditions were solved to find the electric potential in the system. At point O, a plane with the dimension 100 $\mu\text{m} \times 25 \mu\text{m}$ was assumed to have a zero potential. It was also assumed that the boundaries A and B have the potential value ϕ_e . In order to find velocity field, Equations (3-5) and (3-6) subjected to boundary conditions must be

solved. The open boundary condition was assumed for boundaries A and B. The electro-osmotic slip velocity was considered on the walls of channel A-B while the walls in the rest of the system have no-slip velocity condition. By applying the negative electric potentials -50 V at the two ends of the channel A-B and 0 V at point O, electro-osmotic flow was generated in the channel A-B and consequently a pressure gradient was produced in the system.

Figure 3-2 shows the pressure gradient distribution and electrical potential distribution in T-shaped microchannel. As I mentioned before, by applying the negative electric potentials at the two ends of the channel A-B and 0V at point O, electro-osmotic flow will be generated in the channel A-B and consequently a pressure gradient is produced in the vertical channel. In Figure 3-2 (a), the simulation result clearly shows that the point O has the negative pressure (blue color). A pressure gradient is formed in the vertical channel from reservoir C to the point O. The numerical result is in accordance with the theoretical analysis. Figure 3-2 (b) shows that there is no electrical field in the vertical channel, which means that only the pressure-driven flow exists in it.

Figure 3-3 shows the velocity vector in the T-shaped microchannel with 100 μm width of horizontal channel. In the horizontal channel A-B, on one hand, the liquid near the channel walls flows from the point O to the ends of the channel due to electro-osmosis flow, on the other hand, there also is a backward flow in the middle of horizontal channel due to the pressure gradient between the reservoirs (A and B) and the point O. It should be noted that this static pressure gradient is generated by the motion of liquid. Meanwhile, in the vertical channel, the red vectors demonstrate the classic velocity profile of the pressure-driven flow. From this figure, one can clearly see that the dominant flow is the electro-osmotic flow near the walls and hence the net flow is from the point O to the ends of channel A-B. The pressure-driven flow is generated in the vertical channel. To have a better clarification, in channel OA (OB) and OC, the average velocity has been calculated. From the simulation, the average velocity of the net flow at the end of the horizontal channel is about 125 $\mu\text{m/s}$ while the velocity of the electro-osmotic flow is approximately 283 $\mu\text{m/s}$. Although the direction of net flow is from point O to the ends of the channel, the velocity of net flow is much smaller than that of the electro-osmotic flow due to this backward flow. According to the flow continuity, the average velocity in the vertical channel is approximately 168 $\mu\text{m/s}$. Thus, in the numerical simulation, the electrokinetically-induced pressure-driven flow is demonstrated and visualized.

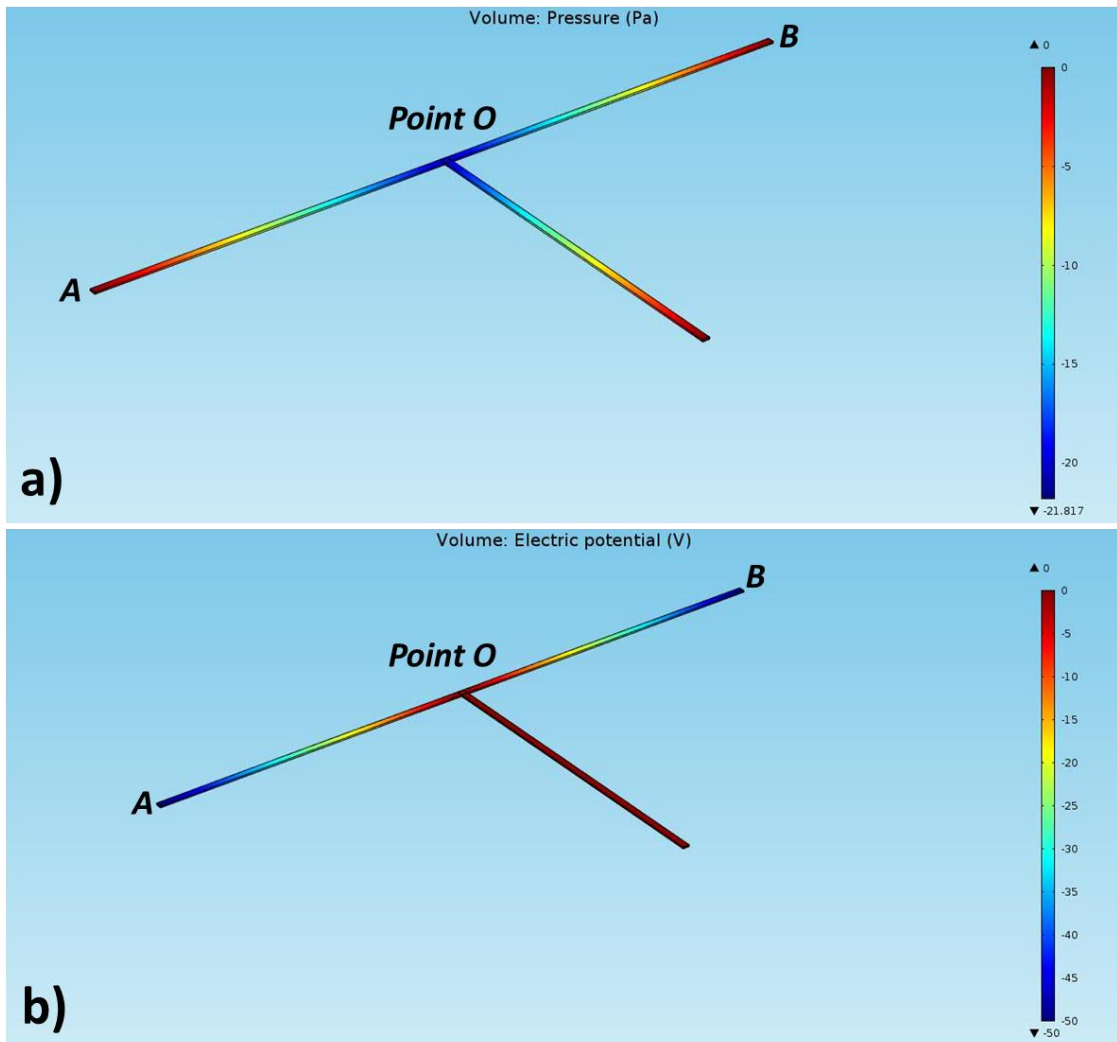


Figure 3-2 (a) Pressure gradient distribution in the T-shaped microchannel. (b) Electrical field distribution in the T-shaped microchannel. The width of horizontal channel is 100 μm . Electrical field intensity is 100 V/cm (-50 V at A, B and 0 V at Point O).

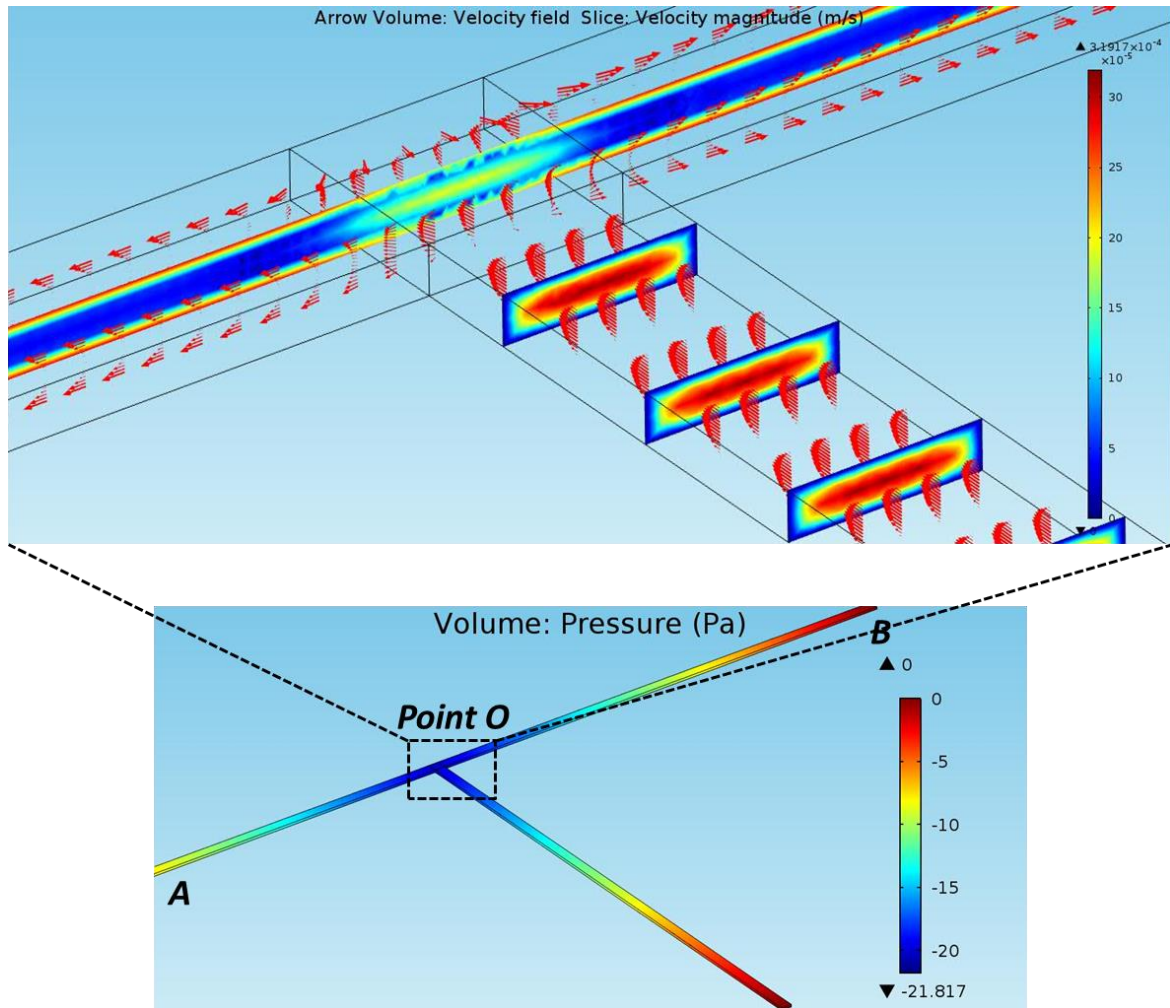


Figure 3-3 The velocity profile in the T-shaped microchannel. The width of horizontal channel is 100 μm . Electrical field intensity is 100 V/cm (-50 V at A, B and 0 V at Point O).

Another reasonable dimension of microchannel for the numerical simulation under the same electric field (-50V at A, B and 0V at Point O) was studied to investigate the influence of this back flow caused by the motion of the liquid. As shown in Figure 3-4, the width of the horizontal channel is decreased to 25 μm . The liquid level is considered the same, i.e. no pressure difference existd among these three reservoirs. It is found that when the width of the horizontal channel is decreased, the backward flow in the middle of horizontal channel is also decreased. In Figure 3-4, the average velocity of the net flow at the end of the horizontal channel is 240 $\mu\text{m/s}$ while the velocity of the electro-osmotic flow is 283 $\mu\text{m/s}$. However, the average velocity in the vertical channel decreases to 105 $\mu\text{m/s}$ due to the reduction of the flow rate in the horizontal channel. According to the result,

conclusion can be drawn that decreasing the cross-section area of the horizontal channel can increase the net flow velocity, which in turn reduce the backward flow significantly caused by the motion of the liquid in horizontal channel. However, it is also found that when the width of the horizontal channel is decreased, the velocity of the flow in the vertical channel is decreased accordingly. This is because the cross-section area has a bigger weight than the backward flow in the determination of the flow rate in the horizontal channel.

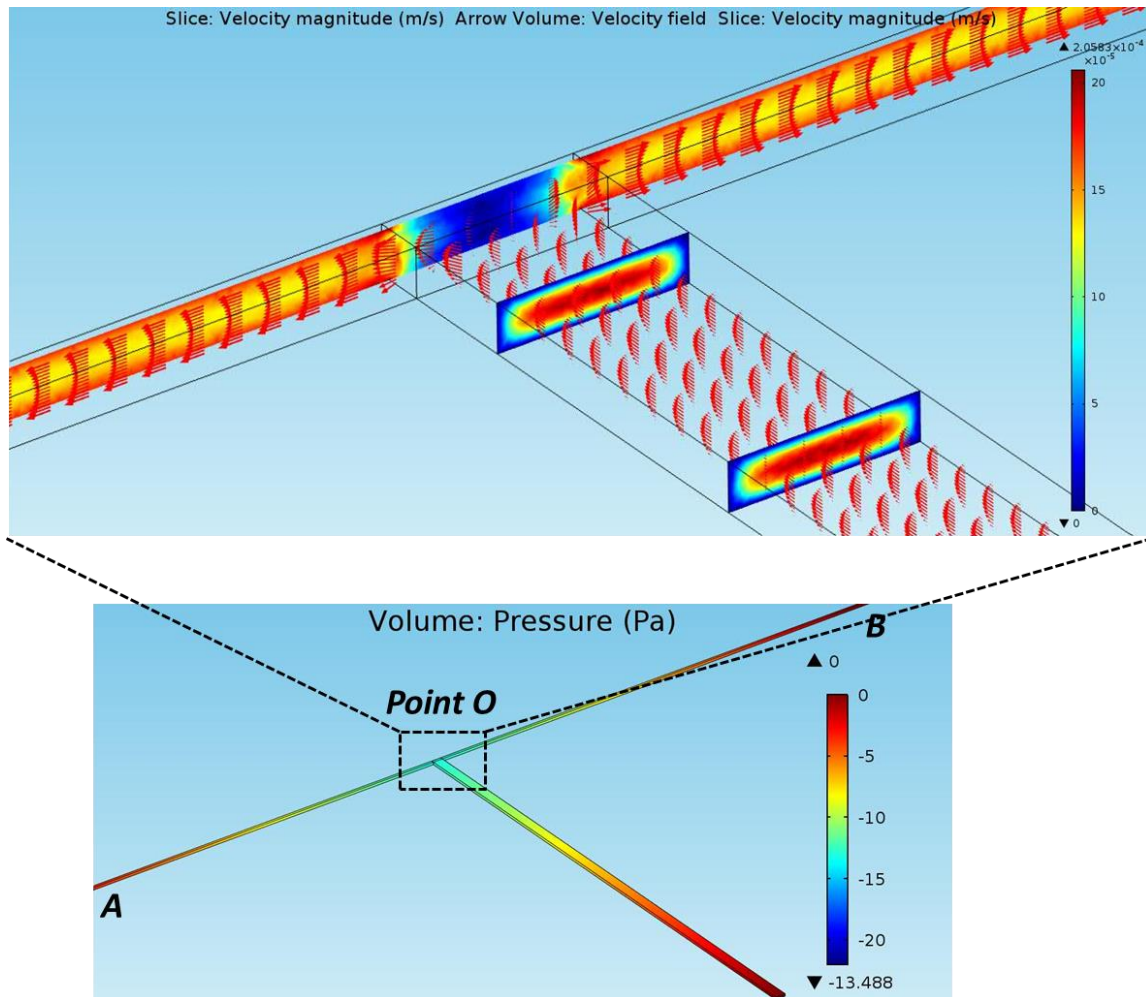


Figure 3-4 The velocity profile in the T-shaped microchannel. The width of horizontal channel is 25 μm . Electrical field intensity is 100 V/cm (-50 V at A, B and 0 V at Point O).

3.3.3 Influence of the pressure-driven back flow

After applying the voltages at reservoirs A, B and Point O, the liquid is pumped from the Point O to reservoirs A and B continuously. Since the direction of the net flow is from the Point O to reservoirs A and B, more and more liquid flows into the reservoirs A and B from the reservoir C with time. The volumes of liquid are increasing in reservoirs A and B and decreasing in reservoir C. The hydrostatic pressure difference is generated due to the height difference of the surface level among reservoirs A, B and C. The pressure-driven back flow caused by the hydrostatic pressure difference may impact the velocity of the flow in the vertical channel. In this section, the influence of the induced-pressure back flow among the three reservoirs is investigated.

As the theory predicts that the plug profile of EOF and the parabolic profile of Poiseuille flow are linearly independent, the model combines EOF and pressure-driven flow to see the influence of pressure-driven back flow in different channel width. The simulation result is obtained to analyze the influence of the pressure-driven back flow. It is well known that the EOF velocity is independent of the channel size, and there is no corresponding increase in the average velocity with increased channel cross-section. However, from Figure 3-5, it is observed that the average velocity decreases linearly with pressure drop between the reservoirs A (B) and C. The slopes of the curves decrease with reducing horizontal channel size under the same electrical field strength, implying that at the same pressure drop, the pressure-driven back flow can impact the average velocity of the vertical channel with bigger cross-section of the horizontal channel. Specifically, from the simulation result, if the pressure drop is 10 Pa, the average velocity has a big drop of about 33.3% for the 100 μm width of horizontal channel while the average velocity only drops about 15.8% for the 25 μm width of horizontal channel. It indicates that if the pressure-driven back flow is a big concern, it is better to choose the smaller horizontal channel size to reduce the influence of the pressure-driven back flow.

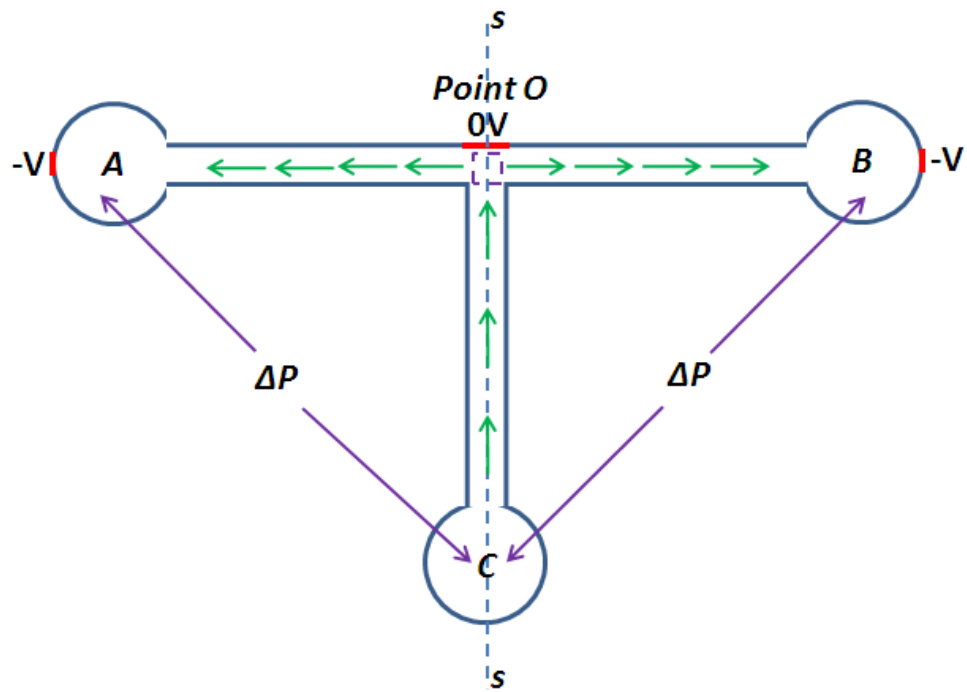
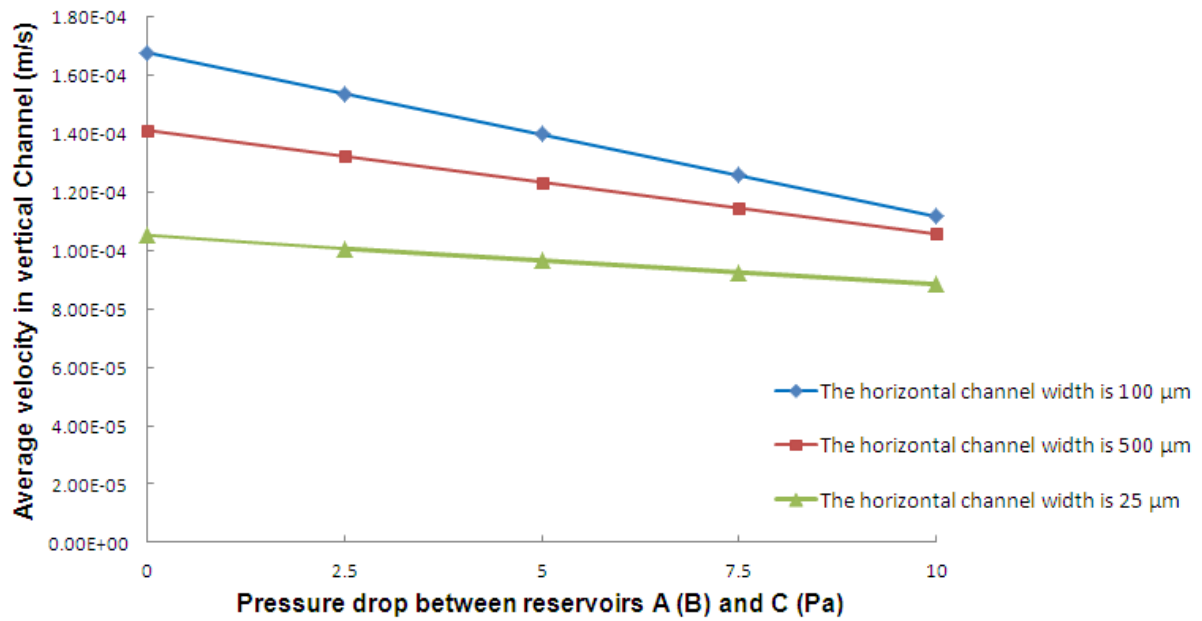


Figure 3-5 The relationship between the average velocity in vertical channel and the pressure drop for different horizontal channel size. Electrical field intensity is 100 V/cm (-50 V at A, B and 0 V at Point O).

3.3.4 The relationship between the average velocity in vertical channel and the horizontal channel size

From above discussion, after adjusting the dimensions of the microchannel, the influence of the pressure-driven back flow can be reduced. Another way is to increase the size of the three reservoirs, which also can reduce the effect of the pressure-driven back flow significantly. In this section, a pure EOF model without pressure disturbance is investigated. In this simulation, for all the channel sizes, the EOF velocity equals to $283 \mu\text{m/s}$, which is in line with the theoretical value calculated by Eq. 3-3. Figure 3-6 shows the relationship between the average velocity in vertical channel and the different horizontal channel size under the same electrical field intensity. It is noted that when the width of horizontal channel exceeds $100 \mu\text{m}$, the average velocity in vertical channel only increases slightly. The chart below can help to design the microchannel in the experimental study.

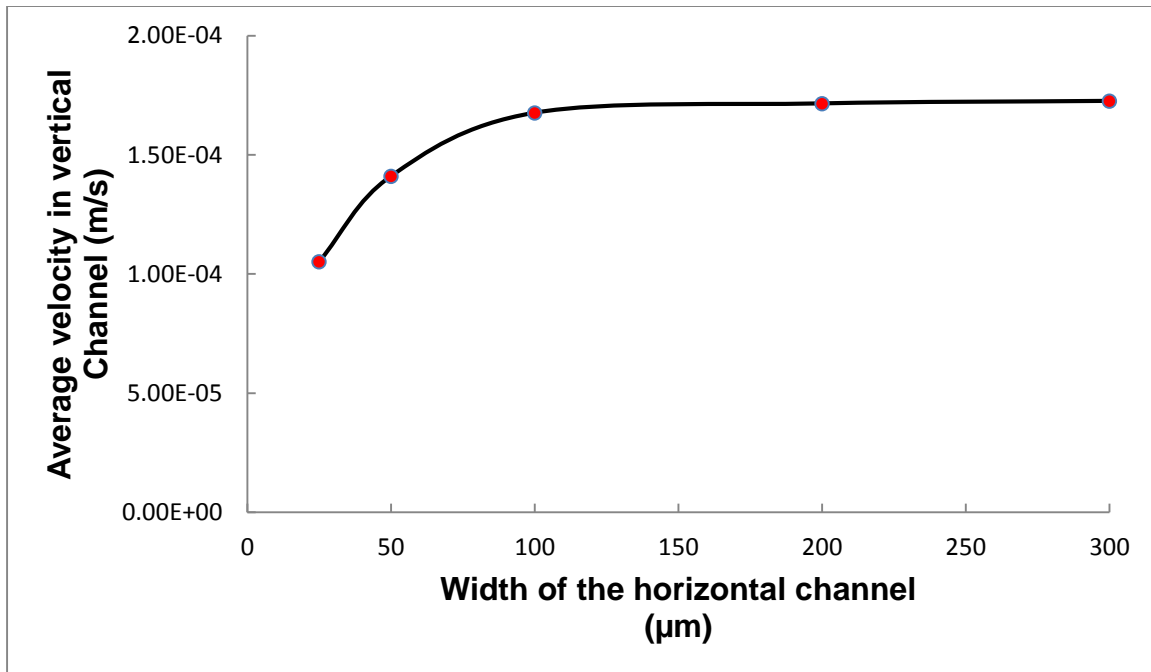


Figure 3-6 The relationship between the average velocity in vertical channel and the different horizontal channel size under the same electrical field intensity. Electrical field intensity is 100 V/cm (-50 V at A, B and 0 V at Point O).

3.3.5 The relationship between the average velocity in the vertical channel and different electrical field intensity

The motion of the flow is caused by the electrokinetic-induced pressure-driven flow. Therefore, the velocity of the flow can be controlled by the electrical field intensity applied on the reservoirs A (B) and Point O. To verify this, a series of simulation were conducted by applying different electrical field intensity with different horizontal channel size. Figure 3-7 presents the variation of the average velocity in the vertical channel with respect to the applied electric voltages at A and B. The electric potential at the point O is kept at zero. From this figure, it is evident that the average velocity of the flow is linearly dependent on the applied voltage. By increasing the magnitude of the applied voltage, the average velocity of the flow is increased. The velocity in the vertical channel is controllable due to the requirement of experiment.

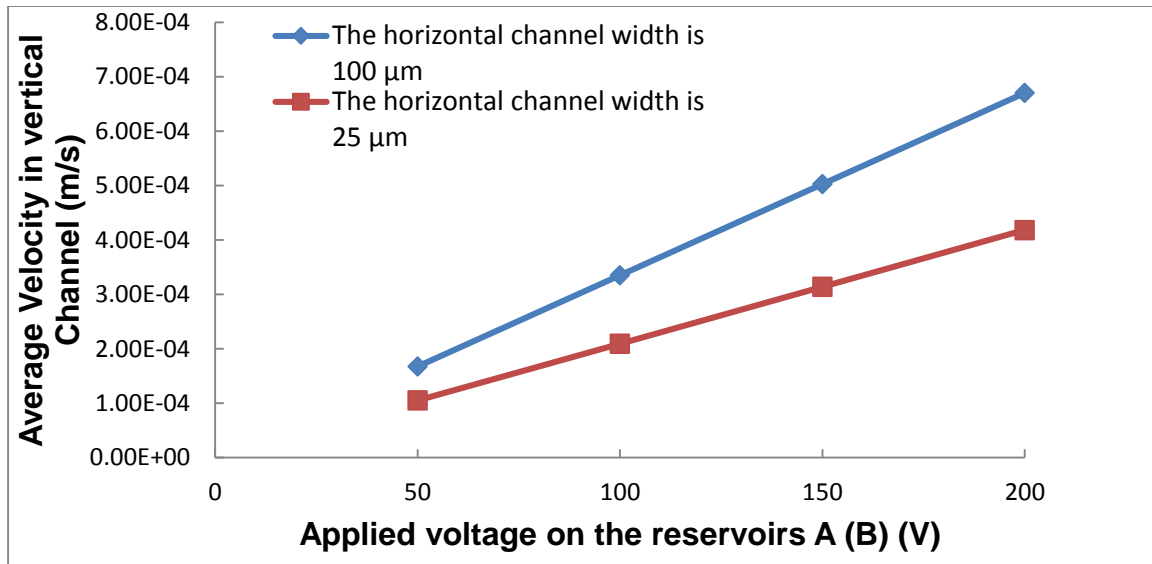


Figure 3-7 The relationship between the average velocity in vertical channel and the applied electric voltages at reservoirs A and B. Electrical field intensity is 100 V/cm, 200 V/cm, 300 V/cm and 400 V/cm, respectively (-50 V, -100 V -150 V, -200 V at A, B and 0 V at Point O).

3.3.6 The simulation of the motion of particles

By assuming that particles were loaded in the reservoir C, the motion of the particles was simulated in the vertical channel due to the electrokinetically-induced pressure-driven flow. The simulation model has been mentioned in Section 3.3.2. This simulation describes the transient motion of particles as it

moves with the fluidic flow in the vertical channel. The motion of particles is defined by Newton's second law

$$\mathbf{m} \frac{d^2\mathbf{x}}{dt^2} = \mathbf{F} \left(\mathbf{t}, \mathbf{x}, \frac{d\mathbf{x}}{dt} \right) \quad (3-7)$$

where \mathbf{x} is the position of the particle, m the particle mass, and \mathbf{F} is the sum of all forces acting on the particle. After solving by the COMSOL 4.2a, the sequential images in Figure 3-8 which illustrates the movement of particles along the vertical microchannel are obtained. These images show the motion of particles with the electrokinetically-induced pressure-driven flow.

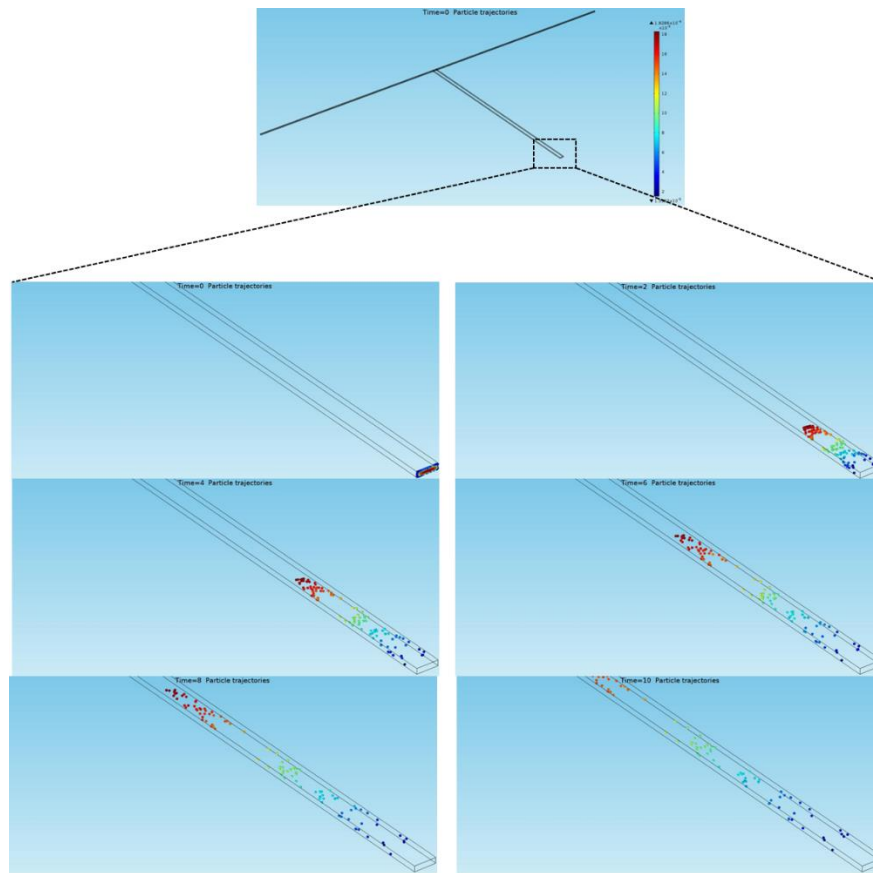


Figure 3-8 Sequential images of the simulation of particle's motion. Cross-sections are $25 \mu\text{m}$ (w) \times $25 \mu\text{m}$ (h) in horizontal channel and $100 \mu\text{m}$ (w) \times $25 \mu\text{m}$ (h) in vertical channel. Electrical field intensity is 100 V/cm (-50 V at A, B and 0 V at Point O). Diameter of the particles is set up to $10 \mu\text{m}$.

3.3.7 Summary

Although either the pressure-driven pumping force or EOF pumping force is used to drive particles/cells in many published papers, a novel method combining the EOF pumping force and the pressure pumping force is proposed in this thesis. This method eliminates the shortcomings of both of them. After doing the literature reviews, only the proposed method presents the possibility to make a real portable flow cytometry device. The numerical simulation results prove that the electrokinetically-induced pressure-driven flow can be generated in the T-shaped microchannel. Meanwhile, the particles can be driven in the vertical channel due to the induced pressure-driven flow.

3.4 Experimental study

The experimental study was performed to prove the electrokinetically-induced pressure-driven flow in a T-shaped microchannel. In this section, the experimental results are demonstrated. The particles and real blood cells were successfully driven in the microchannel based on the electrokinetically-induced pressure-driven flow.

3.4.1 Material and solution

In this experimental study, fluorescent particles and non-fluorescent particles of different sizes are used for visualizing the phenomenon: carboxyl polymers microspheres (Bangs Laboratories Inc., Fishers, Canada) of 10 μm and 5.76 μm in diameter. Microsphere concentration is 1% solids (10 mg mL⁻¹). The excitation and emission light wavelengths of the fluorescent microspheres are 480 and 520nm, respectively. The diameters of these microspheres are close to the real blood cells (RBCs, WBCs and platelets). For the flow visualization, Rhodamine B solution was used as an indicator, the wavelength of excitation and emission light are 540 and 625nm, respectively.

In the experiments of testing the real blood cells, human blood was procured (hematocrit of 45%) from a volunteer by a professional assistant. No anticoagulant and pre-treatment were applied to the blood. Blood cells were diluted by the 1X DULBECCO'S PBS buffer (MP Biomedicals, LLC, Fishers, Canada). Initially, the microchannel chip was filled with the DI water for the particle testing and 1X DULBECCO'S PBS buffer for the blood cell testing.

3.4.2 Chip and electrode fabrication

A PDMS (polydimethylsiloxane) microfluidic chip was fabricated by using the soft lithography protocol (Figure 3-9). First, a master was prepared by spin coating a film of SU-8 negative photoresist onto a silicon wafer. After pre-baking, a photomask bearing the microchannel geometry was placed on the top of the film. The photoresist film covered with the mask was then exposed to UV light. After post-baking and developing, a master could be obtained. A 10:1 (w/w) mixture of PDMS polymer base and curing agent was then poured over the master and cured at 75°C for 3h after being degassed under vacuum. After this step, the PDMS slab was solidified on the master and then peeled off from the master. Reservoirs were punched on the PDMS slab at the designed locations. Finally, the PDMS slab and a glass slide were bonded tightly after treating them in an oxygen plasma device for 30s to form the desired microchannel chip. In this design, the depth of the microchannels was 25µm.

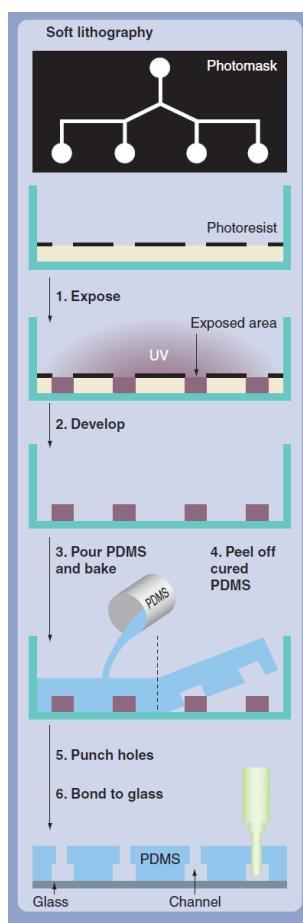


Figure 3-9 Soft lithography protocol. UV light is used to project channel patterns of a high resolution photomask onto photoresist. Once the photoresist is developed, only the exposed parts remain. They act as a negative mold onto which liquid PDMS is poured. Subsequently, the PDMS is baked at 65 °C. Cured PDMS is peeled off the mold revealing the positive channel structures. After punching wells, the PDMS microchip is bonded to a glass slide in a plasma oven (Used with permission by Expert Reviews Ltd).

The fabrication procedure of the copper microelectrode is developed by the soft lithography. First, The Pyralux AP singlesided copper-clad laminate AC 182000R (Dupont Electronic Materials, Research Triangle Park, NC) was spin-coated with a layer of SU-8 at 2000 rpm. After the baking treatment, a photomask bearing the electrode geometry was placed on the top of the copper film and exposed to UV light. After post-baking, the unexposed photo-resist is dissolved by the chemical developer (MicroChem, Newton, MA). The copper sheet covered with a layer of exposed photo-resist of the desired pattern is emerged in the copper etchant CE-100 (Transene Company Inc., Danvers, MA) at 150°C until all the uncovered copper is removed. Finally, the copper electrodes are placed in NaOH (30%) bath at 130°C for 60 min to remove the polyimide substrate and the photo-resist. The microelectrodes were inserted carefully into the electrode chambers on the PDMS chip manually under a microscope (AZ100, Nikon, Japan). After that, the PDMS slab was plasma treated and bonded with a glass slide (VWR) to form the microchannel with embedded electrodes. Because the thickness of the microelectrode (18 µm) was slightly smaller than the depth of the PDMS electrode chamber (25 µm), a droplet of liquid PDMS was used to seal the gap between the PDMS slab and the glass substrate by capillary action, and followed by heating on a hotplate at 200°C for several seconds to make it solidified.

3.4.3 Chip design

The schematic diagram of the designed microfluidic chip is shown in Figure 3-10. The design basically agrees with the dimension parameters obtained from the simulation study. The chip consists of three reservoirs and two main microchannels: one is the vertical microchannel of 100 µm in width and 5mm in length, another is the horizontal microchannels of 25 µm wide and 1cm long. A chamber connected to the horizontal channel is used to place the electrode. There is a tip in the front of the electrode, thus the electrode is closer to the microchannel that is similar to the numerical simulation. The red spots in Figure 3-10 indicate the positions of the other two electrodes. The upper reservoirs

and the channel are initially filled with a buffer solution and the lower reservoir is used to add sample solution. In the experiment, particles were found likely stick onto the surface of the electrode by this design and these particles would block the horizontal channel and then changed the distribution of the electric field. To improve the performance of the microfluidic chip, a few modifications were made, as shown in Figure 3-10 (b) and (c). In Figure 3-10 (b), the tip is removed from the electrode and the length of neck channel is shortened. In Figure 3-10 (c), two branch channels are added into the design. When conducted the experiments on these two modified microfluidic chips, it was found that the second design helped to decrease the amount of the particles stick to the electrodes but still would block the neck channel. For the third design, the particles were split into two branches before flowing to the horizontal channel and then spread into the electrode chamber. Compared with the second modified design, this one decreased the chance of blocking the neck channel by the sticky particles significantly.

The profile of the pressure-driven flow in the vertical channel is parabolic, which indicates the velocity in the middle of the channel has maximum magnitude while the velocity decreases to zero towards the wall. A converging-diverging section is introduced into the vertical channel, as shown in Figure 3-10 (d), for accelerating the speed of the particles along the wall as well as focusing the particles. According to the experimental results, the speed of the particles increased when passing through this converging-diverging section. However, this converging-diverging section cannot focus particles. Because the flow in the vertical channel is the laminar flow and the particles will flow along the streamlines. The design of the converging-diverging section cannot change the streamlines therefore it cannot change the pathway of the particles. The design of this converging-diverging section is abandoned in the following study.

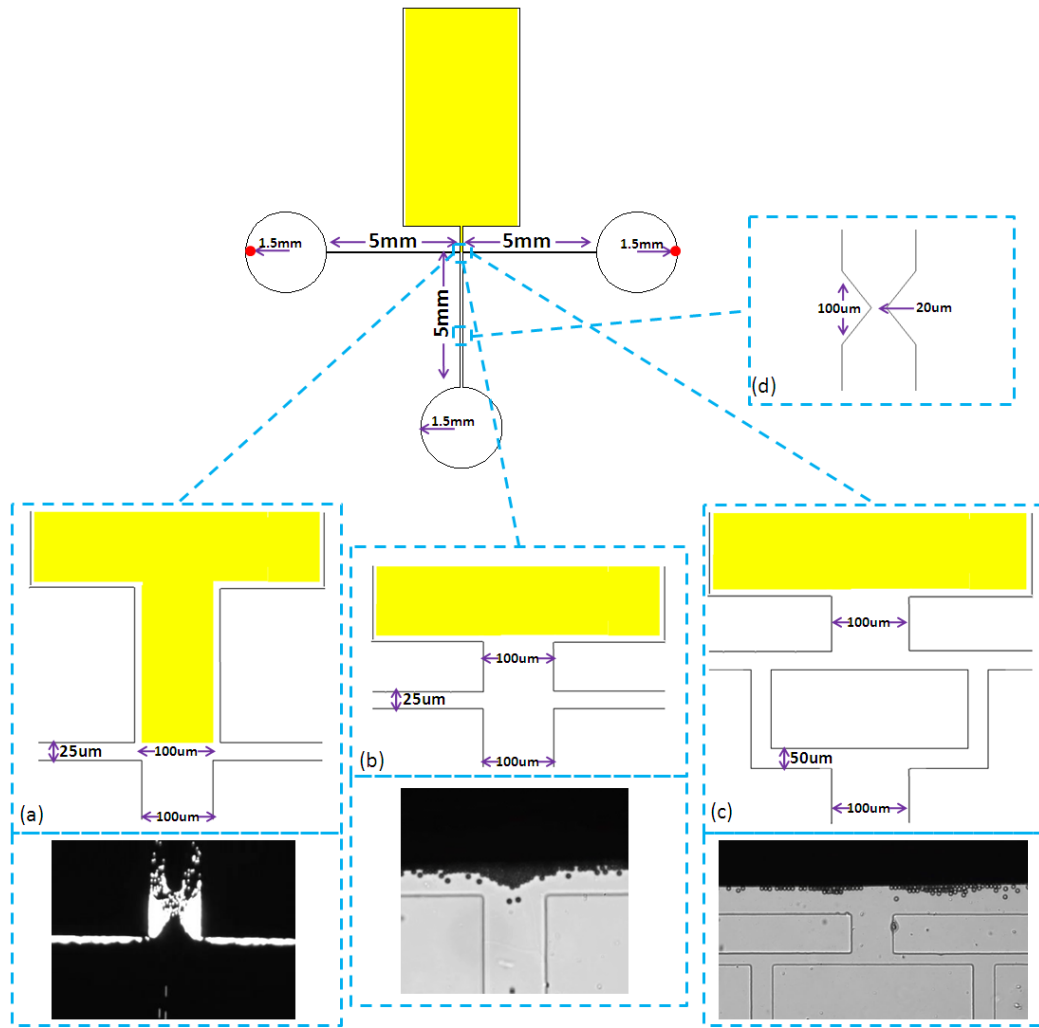


Figure 3-10 Two-dimensional (x - y plane) illustration of the microchannel design used in this study.

3.4.4 Experimental setup and operation

The experimental workstation consisted of the following major components: the microfluidic chip, a fluorescence microscope and image system, a DC (direct current) power supply and a data acquisition system, as shown in Figure 3-11. The microfluidic chip was fixed on the observation platform of the microscope. The DC regulated power supply (CSI12001X, Circuit Specialists Inc., USA) was used to control the voltages applied to the different electrodes. A fluorescent microscope (AZ100, Nikon) with a high intensity illumination system and two kinds of the CCD camera (DS-QiIMc, Nikon and Retiga 2000R, Nikon) was used to visualize the motion of the liquid (dye solution) and the

particles/cells inside the microchannel. The images were captured by the digital camera and digitized by the computer software (NIS-Elements BR 3.0).

The fluorescent particles and dye solution were used in the visualization experiments. Initially the reservoirs A and B were filled with 8 μL of DI water. To start the experiment, 8 μL of the sample solution was loaded to the reservoir C so that there was no pressure difference among the reservoirs. By applying the -50 V at the two ends of the channel A-B and 0 V at the point O, electro-osmotic flow was generated in the channel A-B and consequently a pressure gradient was produced in the network. All the images were obtained by the same CCD camera.

In experiments using real blood cells, the reservoirs A and B were filled with 8 μL of 1X PBS buffer. To start the experiment, 8 μL blood cell sample was loaded to the reservoir C. Because the PBS buffer could generate undesired effects (e.g., bubbling) under higher electric field, lower voltage (-40 V) was applied. All the images were obtained by the same CCD camera.

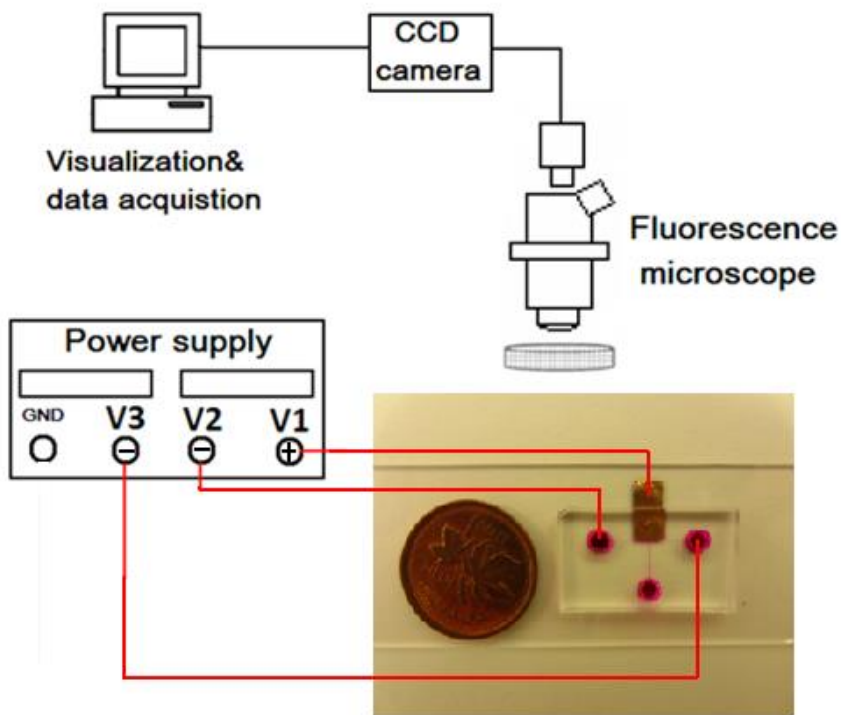


Figure 3-11 The microfluidic chip and the experimental system: a picture of the chip and the illustration of the experimental system.

3.4.5 Experimental results

- *Demonstration of the electrokinetic-induced pressure-driven flow in the microchannel*

To demonstrate that the liquid can be controlled and transported by the applied electric field from the Point O into reservoirs A and B, Rhodamine B was used as a tracer to visualize the movement of the flow. Figure 2-12 shows a series of fluorescent images of the horizontal channel and the vertical channel during the dye solution traveling. As shown in Figure 3-12, dye solution flowed in the vertical channel due to the electrokinetic-induced pressure-driven flow. Then, it moved towards the reservoir A and B due to the electro-osmotic flow.

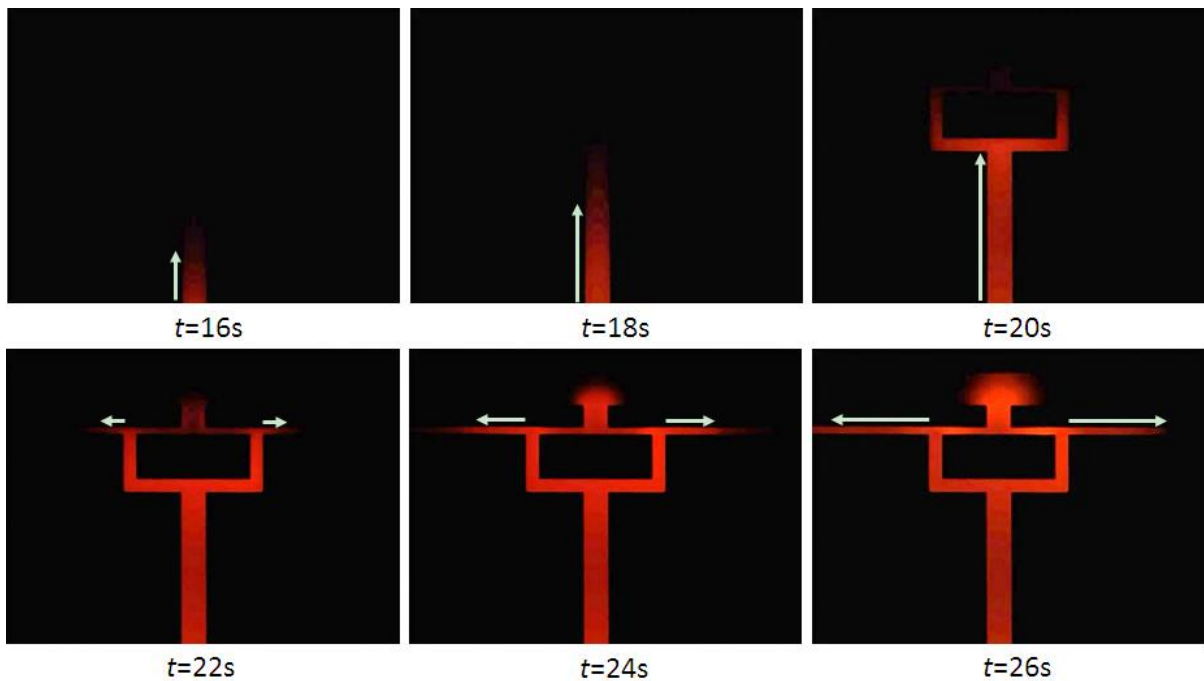


Figure 3-12 A series of fluorescent images of electrokinetic transport of Rhodamine B dye solution in microchannels. Red strips were fluorescent dye moving in the horizontal channel and the vertical channel ($E=100$ V/cm. -50 V is applied at the two ends of the channel A-B and 0 V at point O).

- *Demonstration of the motion of $10\ \mu\text{m}$ and $5.76\ \mu\text{m}$ diameter fluorescent microspheres*

To simulate the blood cells in the microchannel, fluorescent microspheres of two different sizes were used to replace the blood cells. $10\ \mu\text{m}$ fluorescent microspheres were used in this experiment as the substitute of the white blood cells. $5.76\ \mu\text{m}$ fluorescent microspheres were used to simulate the red

blood cells. As shown in Figure 3-13, the fluorescent microspheres were passing through the vertical channel due to the electrokinetic-induced pressure-driven flow.

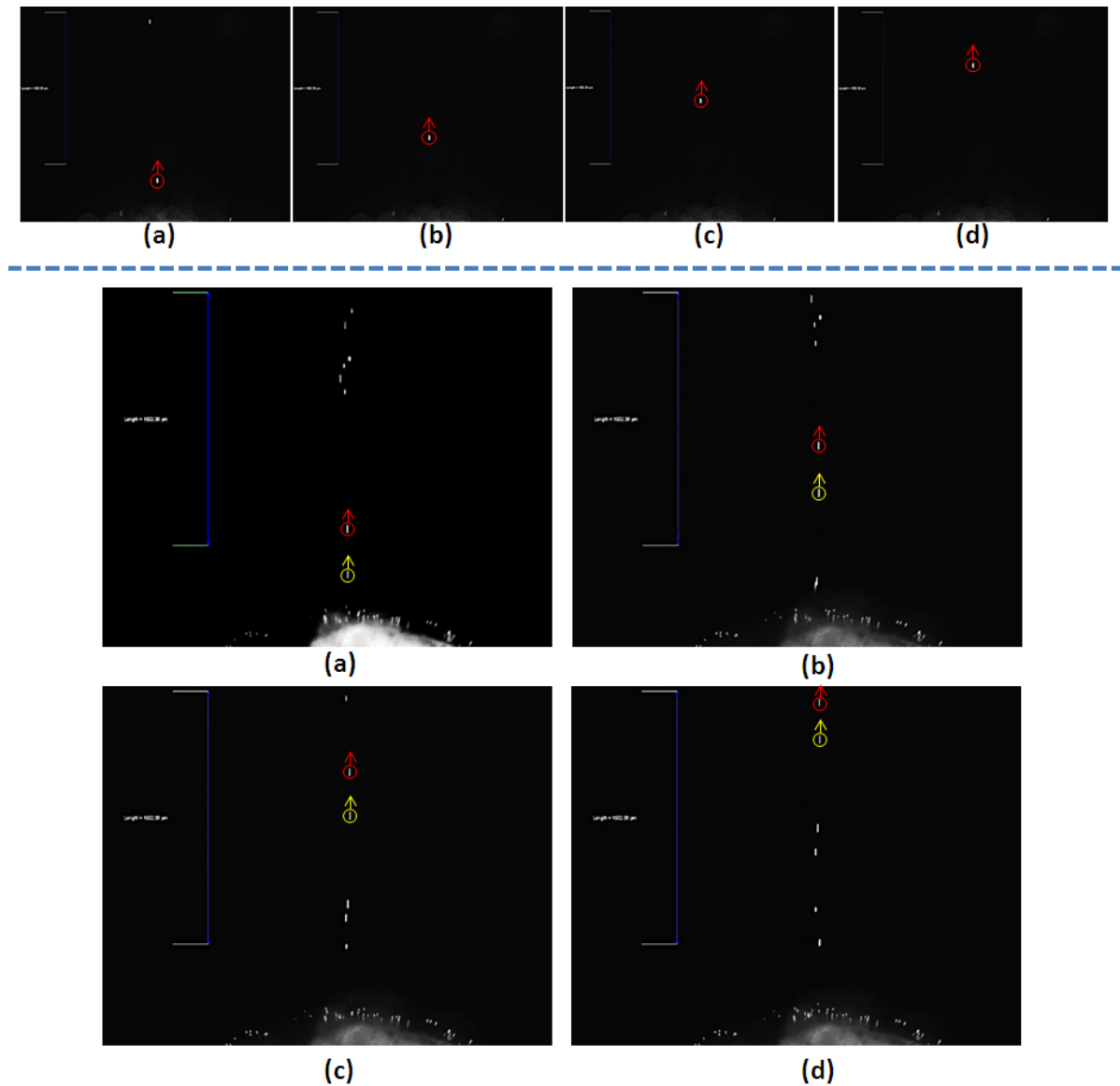


Figure 3-13 A series of fluorescent images of the motion of 10 μm and 5.76 μm fluorescent microspheres ($E=100\text{ V/cm}$. -50 V is applied at the two ends of the channel A-B and 0 V at point O). The upper four images indicate the 10 μm fluorescent microspheres flowing in the vertical channel at different time. The bottom four images show the 5.76 μm fluorescent microspheres flowing in the vertical channel at different times.

- *Demonstration of the motion of the real blood cells in the microchannel*

In experiments using real blood cells, reservoirs A and B were filled with 8 μL of 1X PBS buffer firstly. To start the experiment, 8 μL diluted blood cell sample was loaded to the reservoir C. Initially, -50 V was applied to reservoirs A and B, respectively. However, this experiment failed due to the serious electrolysis of the PBS buffer. After a series of tests, the applied voltages were reduced to -30 V in reservoirs A and B, respectively. It was observed that blood cells were transported in the microchannel. Figure 3-14 and 3-15 show that blood cells were flowing along the vertical channel (Figure 3-14) and the converging-diverging section (Figure 3-15). The result demonstrates that the motion of the continuous, real time blood cells could be achieved by using the presented electrokinetic-induced pressure-driven flow method in a microfluidic chip.

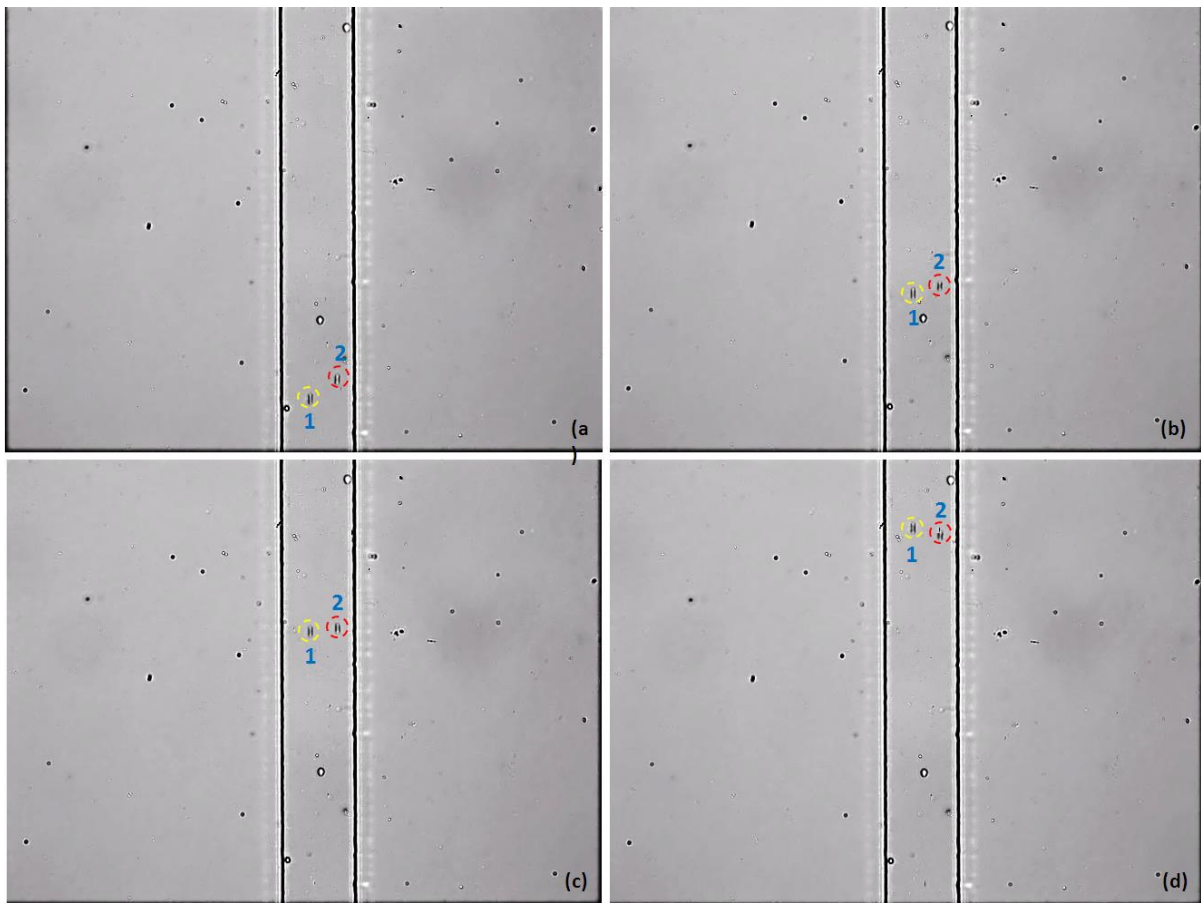


Figure 3-14 A series of images of the motion of real blood cells ($E=60 \text{ V/cm}$, -30 V was applied at the two ends of the channel A-B and 0 V at point O). The four images indicated the blood cells flowing in the vertical channel at different time.

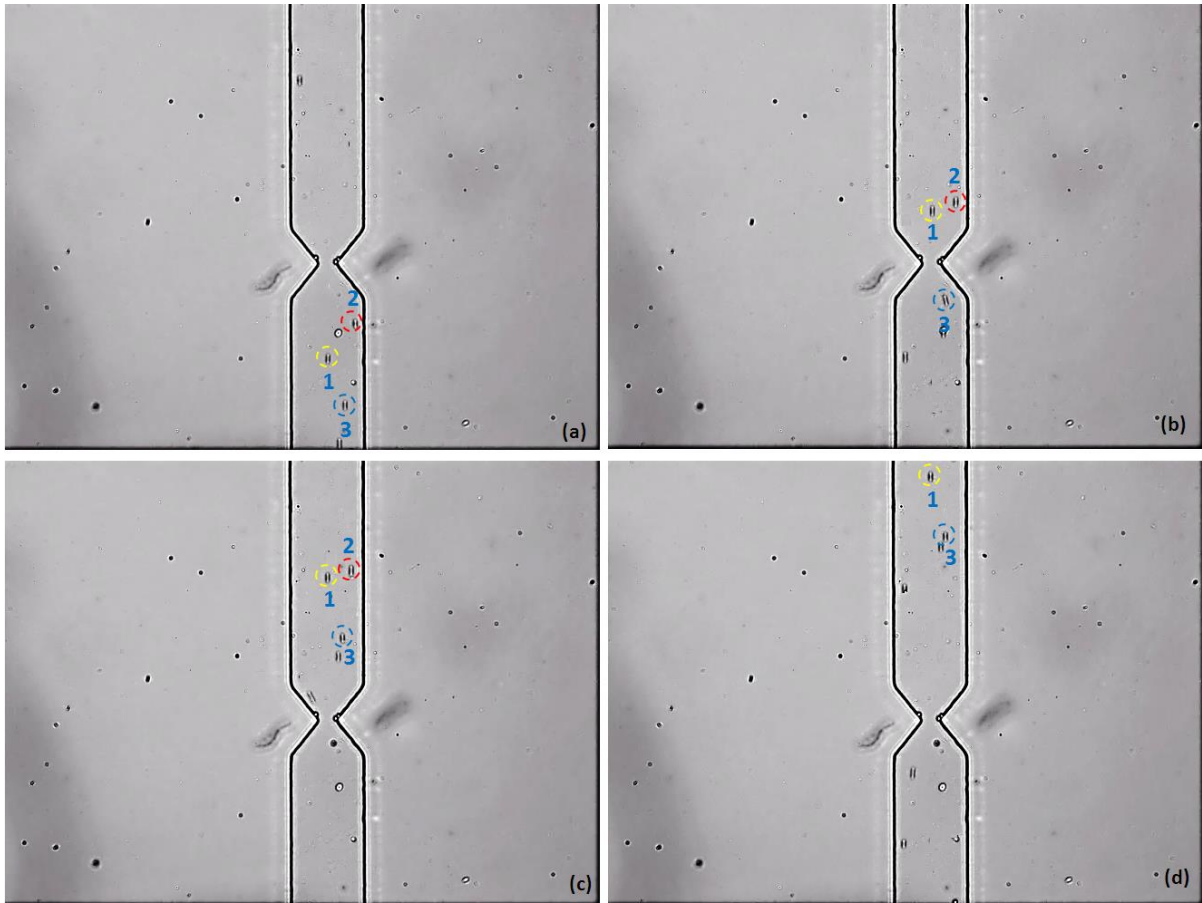


Figure 3-15 A series of images of the motion of real blood cells ($E=60$ V/cm, -30 V was applied at the two ends of the channel A-B and 0 V at point O). The four images indicated the blood cells passing through the converging-diverging section in the vertical channel at different time.

3.5 Concluding remarks

In this chapter, a novel method is presented to combine the electrokinetical force and the pressure-driven force. As I demonstrated in the reviews, most current microfluidic flow cytometry devices are micro- only in the microfluidic chip, the rest of most apparatuses such as pumps, valves and tubing are still bulky and expensive, which is very difficult to be integrated into the system. In this thesis, the novel approach utilizes the advantages of both of the electrokinetical pumping force and the pressure-driven pumping force. Once this novel microfluidic chip is applied in the flow cytometry devices, the total size of the current microfluidic flow cytometry system can be reduced greatly because no valves, tubes and external pumps are involved. This fundamental work solves the major problem which exists

in current microfluidic flow cytometry devices. Numerical and experimental results show that the electrokinetically-induced pressure-driven flow work well.

Chapter 4

Study of Dual-Wavelength Fluorescent Detection of Particles/cells on a Novel Microfluidic Chip

4.1 Introduction

In this chapter, a novel miniaturized dual-wavelength fluorescent detection system was designed and developed for particle counting and detection. This system can detect and count two different fluorescent particles/cells simultaneously. Good agreement is achieved between the results obtained by the proposed flow cytometry device and the results obtained by a commercial flow cytometer.

4.1.1 Light source

Conventional flow cytometers are dependent on the laser as an excitation source which also is used in the microfluidic flow cytometers. However, laser has some fatal shortcomings such as the high levels of heat, the big volume and the high cost. In this study, the LED (light emitting diodes) is considered as the excitation light source. To realize the dual-wavelength detection, two lasers with different wavelength must be used. The high cost can't be accepted in the microfluidic flow cytometers. Moreover, the lasers will generate high levels of heat. The cooling system must be prepared for lasers. More components mean the huge size and weight. Compared with the laser, the cost of LEDs can be ignored. The bi-color LED combines two LEDs in a single package which is ideal for small scale applications where multiple signals need to be displayed, so dual-wavelength detection can be realized.

The most common excitation sources used in the flow cytometer today are the light wavelength of 488 nm and 633 nm. These two wavelengths are enough variation to cover most researchers' needs. Therefore, blue/red bi-color LED is selected in my study. Moreover, the blue light is selected because of its capability to the commonly used fluorescently excited fluorochromes. The red light is chosen because of its good penetrating capability through tissue and blood, as well as its strong excitation capability of commonly used fluorochromes. In addition, both excitation wavelengths are sufficiently far from the emission wavelengths of the fluorescent molecules used for detection, allowing for the effective filtering of reflected excitation light from fluorescence light.

4.1.2 Optical system

In the optical system, the key point is to separate the lights of the different wavelengths and divert them to the different detectors. However, in a microfluidic flow cytometer, the space is limited. It means that it cannot put many optical filters in the device. Usually, the WDM (wavelength division multiplexers) integrated the dichroic (long-pass) filter and the band-pass filter is used in the microfluidic flow cytometers. However, the price of WDM is still high and can't be accepted. Moreover, using WDM is very easy to lose the fluorescent signal due to the strict requirement of the incident angle of the light. In our study, a 3D printer was utilized to make a module which can be used to assembly the filters and the photo detectors. The novel strategy of the detection system will be introduced as following.

4.1.3 Modified microfluidic chip

Compared with the design of the microfluidic chip which was presented in Chapter 3, this new microfluidic chip was modified to fit the miniaturized dual-wavelength fluorescent detection system. Due to the mass production concern, the microelectrode was removed. A small hole is punched at the point O so that an electrode can be easily placed in the small hole. The vertical microchannel was bended to reduce the light pathway. All the dimensions of this modified microchip were the same as the microfluidic chip which was presented in Chapter 3. The experiment results show that the new microchip work well.

4.2 Methods

4.2.1 Electrokinetically-induced pressure-driven flow

A schematic diagram and a photograph of the novel microfluidic chip are shown in Figure 4-1. The fluidic control system consists of four reservoirs A, B, C and O, one main L-shaped microchannel of width 100 μm and length 5 mm, and one pumping channel of width 25 μm and length 1cm, connecting wells A and B. There is a neck channel of width 100 μm and length 100 μm to connect the L-shaped microchannel and reservoir O. The diameter of reservoirs A, B, C and O are 3 mm, 3 mm, 3 mm and 1.5 mm, respectively. The reservoirs and the channels are initially filled with a buffer solution. The particle sample solution is added to the Reservoir C finally.

The channel A-B is used as an electroosmotic pump where the electroosmotic flow is generated by applying DC voltages via electrodes inserted in reservoirs A, B and O. The direction of the

electroosmotic flow (EOF) is from the reservoir O to both reservoirs A and B. When EOF is generated in the channel A-B, the cross-junction area near the reservoir O has a negative pressure that induces a pressure-driven flow from reservoir C to reservoir O. Consider the cross-junction region near the reservoir O in Figure 4-1 (a). Once the electric field is applied along the pumping microchannel, the liquid in this cross-junction region will be pumped into the wells A and B. Because of the fluidic continuity, the liquid in L-shaped channel will move into the cross-junction region to fill it. Thus, a pressure gradient is generated between reservoir C and the cross-junction near reservoir O. This pressure-gradient will generate a continuous flow in the L-shaped channel. The particles loaded in the reservoir C will then be carried with the flow to pass a optical detection spot in the L-shaped microchannel. In this way, the different fluorescent particles can be counted and detected. Using this method, no moving parts, external tubing, valves and syringe pumps are required. If the sample particles are biological cells, the cells will not experience any electric field, because there is no applied electric field in the L-shaped channel.

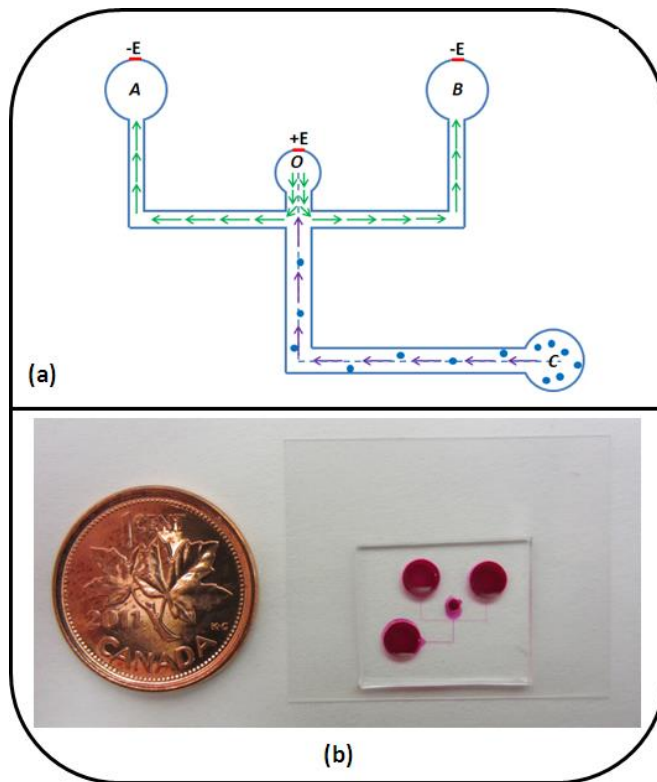


Figure 4-1 (a) Schematic diagram of a new method to generate electrokinetically-induced pressure-driven flow in a microchannel. The arrows indicate the flow directions. The particles/cells are loaded initially in reservoir C. (b) A photograph of the microfluidic chip.

4.2.2 Low-cost, dual-wavelength fluorescent detection system

A miniaturized, low-cost, optical detection system was designed and developed in this study to achieve dual-wavelength detection at a single spot. As illustrated in Figure 4-2, the core of this miniaturized fluorescent detection system consists of a high-power bi-color blue/red LED (488/635 nm, LedEngin, CA, USA) as the excitation source, a dual-wavelength excitation filter (CWL: 488/635 nm, FWHM: 20 nm, Chroma, VT, USA) to select the two excitation wavelengths, two band-pass emission filters (CWL: 535 nm, FWHM: 20 nm, Chroma, VT, USA; and CWL: 710 nm, FWHM: 40 nm, Semrock, NY, USA) to transmit the specific emitted fluorescence and block the background light noises, and two Si photodiodes (S8745-01, Hamamatsu, Japan) as the photo-detectors. In order to assembly all optical components into the limited space and to allow detecting two-wavelength signals from a single spot, the strategy of the optical pathway is very important. In this new design, as shown in Figure 4-2, the microfluidic chip was placed horizontally on a platform; the LED was placed at the side of the microfluidic chip. The light from the LED passes through an excitation filter and shines on the detection region in the upstream of the L-shaped microchannel. The distance of the light pathway is less than 2 cm from the LED to the detection spot. When two different fluorescent particles/cells passed through this spot, fluorochromes were excited. The two emission lights penetrated the bottom glass substrate and the top PDMS layer. One set of a photo-detector and emission filter was placed on the top of the chip to collect 535 nm signals. Another set of a photo-detector and emission filter was placed at the bottom of the chip to collect 710 nm signals. There was an angle of 90° between the pathway of excitation light and the pathways of the two emission lights. Thus, the two different fluorescent signals were separated and captured by two separate photo-detectors. The precise alignment among the LED, the microfluidic chip and the photo-detectors was achieved by a precisely manufactured holder.

It should be noted that the focusing lens is not used in this device. Because the distance between the LED and the detection spot is very short (less than 1.5 cm), the intensity of the excitation light is strong enough to activate the fluorescence of the particles. In the future work, for detecting smaller particles, a focusing lens will be considered to increase the excitation intensity for improving the sensitivity of the device. In this method, no special treatment is required for the PDMS chip and the channel surface.

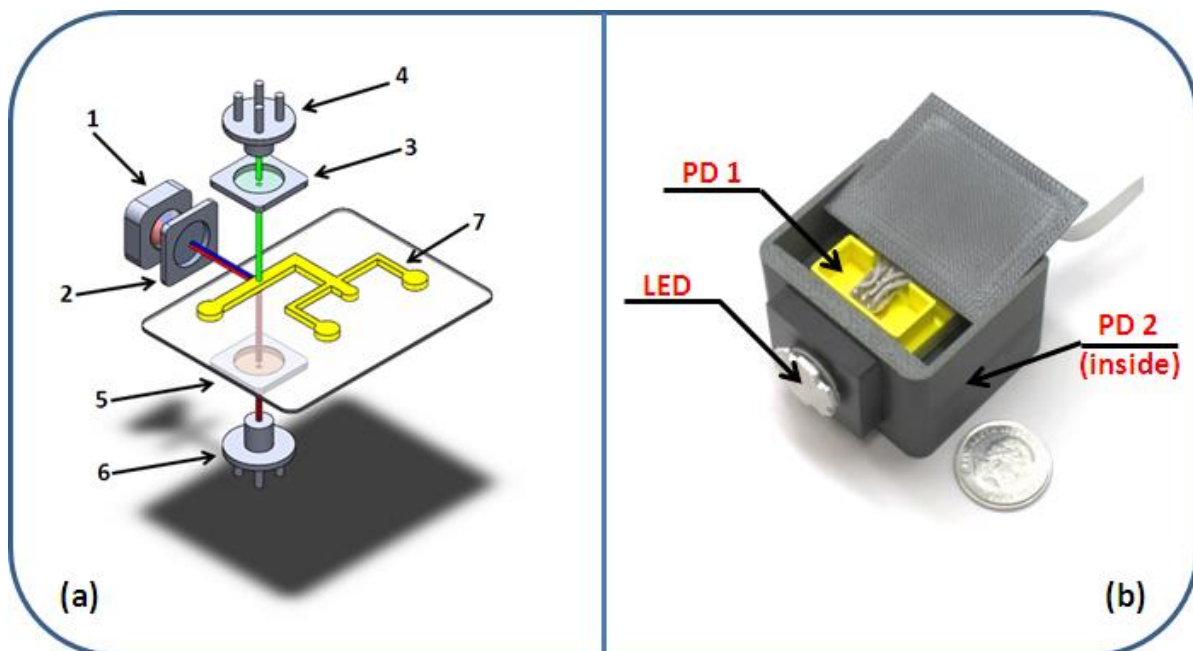


Figure 4-2 (a) Schematic of the dual-wavelength optical detection system. (1) Bi-colour blue/red LED; (2) dual-wavelength excitation filter; (3) band-pass emission filter (535 nm); (4) photodiode 1; (5) band-pass emission filter (710 nm); (6) photodiode 2, (7) microfluidic chip. (b) A photograph of the optical detection system.

4.2.3 Chip fabrication and sample preparation

Polydimethylsiloxane is a Si-based organic polymer that is commonly used in soft lithography. It has some desirable properties such as optical transparency, flexibility and bio-compatibility. Polydimethylsiloxane (PDMS) microfluidic chip was fabricated by using the soft lithography protocol. The photomask of the microfluidic chip was designed by using the AutoCAD software. A film of SU-8 negative photoresist was coated on a silicon wafer by using the spin-coater. After pre-baking, the photomask bearing the microchannel geometry was placed on the SU-8 negative photoresist film tightly. Then, this wafer was exposed to UV (ultraviolet) light. After post-baking and developing, the master could be obtained. After that, A 10:1 (w/w) mixture of PDMS polymer base and curing agent which was degassed under vacuum was poured over the master and cured at 80°C for more than three hours. After this step, PDMS polymer was solidified on the master. After peeling off from the master, the PDMS model was punched to form reservoirs which are open to the air. Finally, the PDMS model and a glass slide were bonded tightly after exposing to oxygen plasma device for 30s to form the desired microchannels.

The fluorescent particles (excitation wavelength 480 nm, emission wavelength 520 nm, BD Biosciences, Fishers, IN, USA) were used in the visualization experiments. The estimated concentration of the particles was approximately $\sim 10^6 \text{ mL}^{-1}$ after dilution. For different experiments, different voltages (-100 V, -80 V, -60 V, -40 V) were applied at the two ends of the channel A-B, and 0V was applied at point O. The electroosmotic flow was generated in the channel A-B and consequently a pressure gradient was produced in the main channel. All the images of particles' motion were obtained by a CCD camera.

To examine the dual-wavelength detection system, two different samples were used: (1) 7.0 μm Dragon Green fluorescent beads (Excited Wavelength 480 nm, emission wavelength 520 nm, BD Biosciences, Fishers, IN, USA) mixed with 7.0 μm Flash Red fluorescent beads (Excited Wavelength 660 nm, emission wavelength 690 nm, BD Biosciences, Fishers, IN, USA), (2) RTS11 cells which are a monocyte/macrophage cell line derived from long-term spleen cultures of rainbow trout, *Oncorhynchus mykiss*.¹³³⁻¹³⁴ The size of this cell is from 7 μm to 15 μm . RTS11 were collected from the culture flasks and centrifuged at $500 \times g$ for 4 min. Then, the cell pellets were washed twice with phosphate-buffered saline (PBS). RTS11 cells were stained with one of the two fluorescent dyes: Calcein-AM (Invitrogen, NY, USA) and Alexa Fluor 647-conjugated phalloidin (Invitrogen, NY, USA). For Calcein-AM staining, RTS11 cells were incubated with 10 $\mu\text{g/mL}$ Calcein-AM in PBS for 30 min, then washed five times with PBS and finally resuspended in 500 μL of fresh PBS. For phalloidin staining, the cells were fixed with 3% paraformaldehyde in PBS for 20 min, permeabilized with 0.1% Triton X-100 for 10 min and washed once with PBS. Fixed cells were then incubated with 3.3 μM of Alexa Fluor 647-conjugated phalloidin for 30 min, and washed five times with PBS prior to being resuspended in 500 μL of fresh PBS. At last, Calcein-AM-stained cells and phalloidin-stained cells were mixed. Different ratios of the two types of particles/cells used in the experiments are listed in Table 4-1. Prof. Niels Bols and his Ph.D student Nguyen Vo (Department of Biology, University of Waterloo) help me to prepare the cells and do the comparison tests of using the conventional flow cytometer.

In the experiments, initially the reservoirs A, B and O were filled with 6 μL , 6 μL and 1.5 μL deionized water, respectively. When starting the test, 6 μL of the sample solution was loaded to the reservoir C. Three different voltages were applied in the reservoirs A, B and O, respectively, to generate electroosmotic flow in the channel A-B. The liquid flow and the motion of sample particles in the L-shaped channel were then produced by the induced pressure driven flow. In the experiments

of using cell samples, the reservoirs A, B and O were filled with 1X PBS buffer. Because the PBS buffer could generate undesired effects (e.g., bubbling) under higher electric field, lower voltages (-50V) were applied at wells A and B.

4.2.4 Experiment Setup

The experimental setup consists of the following major components: a microfluidic chip, a fluorescent detection module, a two-stage amplification circuit, a DC power supply, and a data acquisition system as shown in Figure 4-3. The DC power supply (CS112001X, Circuit Specialists Inc., USA) was used to control the voltages applied to the different electrodes. The optical signals detected by the photo-detectors (PD) were amplified by the two-stage amplification circuit, and were then processed by a custom-made LABVIEW program through a data acquisition board (PCI 6281, National Instruments, Austin, TX). The signal from the PD can be amplified by the two-stage amplifier circuit. The overall amplification gain of the two-stage amplification is $A = A_1A_2$, where A_1 and A_2 are the gains of the first and the second stage amplifiers, respectively. To enhance the signal/noise ratio, an R-C low-pass filter circuit with a desired cut-off frequency was designed before the signal was collected by the Labview program.

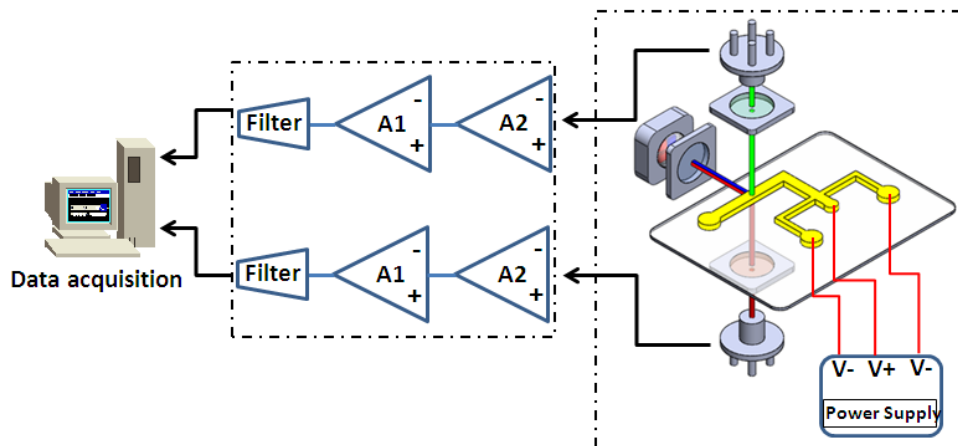


Figure 4-3 Illustration of the experimental system which consists of the microfluidic chip, a two-stage amplification circuit, a fluorescent detection system, DC power supplies, and a data acquisition system.

4.3 Results and Discussion

In order to verify the effectiveness of the modified microchip, a series of experiments to measure the velocity of the particles' motion were conducted first. Because the particles' motion was caused by the electrokinetic-induced pressure-driven flow, therefore, the velocity of the particles should depend on the applied electrical field in the channel AB. In this study, the chip was placed under a fluorescent microscope (AZ100, Nikon) with a high intensity illumination system and digital CCD cameras (DS-QiMc, Nikon and Retiga 2000R, Nikon). The particle's velocity in the microchannel was determined by analyzing the captured images by imaging analysis software (NIS-Elements BR 3.0). Figure 4-4 presents the variation of the average velocity of the particles with the applied electric voltages at A and B. Under a given electric field, the velocities of 10 particles passing through the observed area were measured. Each data point in Figure 4-4 is the average value of the velocities of this group of particles in the same run. The electric potential at the reservoir O was kept at zero. From this figure, it is evident that the average velocity of the particles was linearly dependent on the applied voltage. By increasing the value of the applied voltage, the average velocity of the particles increased.

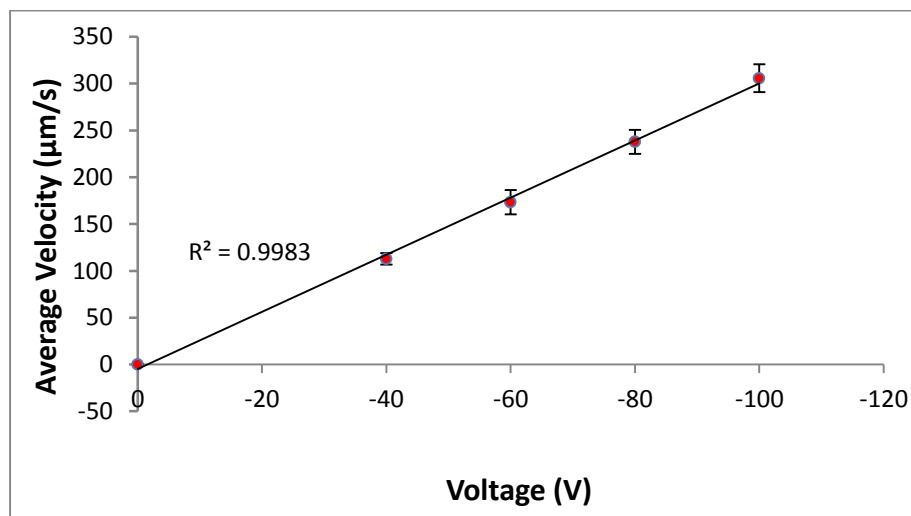


Figure 4-4 The average velocity of the particles moving in the L-shaped channel under different voltages applied at the reservoirs A and B.

The throughput of the particles is one of the important parameters of the microfluidic flow cytometry. Because of the pumping method used in this study, the speed of the particles is proportional to the applied electrical field in the channel AB. In order to avoid Joule heating effect and other undesired effects (e.g., bubbling near the electrodes), a range of the applied voltage from 40 V to 80 V was

found to be appropriate in the experiment. This range of the applied voltage is the major factor limiting the velocity and the flow rate of the electro-osmotic flow in the channel A-B hence the flow rate and the particle throughput in the L-channel of this system. The throughput can be increased by using higher particle concentrations. However, increasing the concentration of sample may cause the problem of overlapping. That is, it is possible that two or more particles pass through the detection zone at the same time, resulting in overlapped signals. In order to reduce the chance of signal overlapping, dilute particle suspensions were used in this work for proving the concept. The actual throughput was about 20~40 particles per minute. Therefore, when use high concentrations of particle solutions, an effective approach must be found for the flow focusing so that the problem of overlapping can be overcome thus the throughput is increased.

Figure 4-5 shows an example of the detected signals of the dual-wavelength fluorescent detection module for a sample solution containing 7.0 μm Dragon Green fluorescent beads and 7.0 μm Flash Red fluorescent beads. The ratio of the Dragon Green fluorescent beads to the Flash Red fluorescent beads is 1 to 3. As shown in Figure 4-5, the magnitude of the peaks for 7.0 μm green fluorescent particle's signal is approximately 4 V, and the magnitude of the peaks for 7.0 μm red fluorescent particle's signal is approximately 2 V. One reason for the weaker red fluorescent signal is the excitation wavelength. The required maximum excitation wavelength of the Flash Red beads is 660 nm; however the maximum excitation wavelength of the LED employed in this study is 635 nm. This difference in the excitation wavelength reduced the intensity of the emitted light from the Flash Red beads, because the intensity of the emitted light is directly proportional to the incident intensity required to excite the fluorophore. Moreover, the signals in Figure 4-5 (b) have a baseline at approximately -1 V, different from Figure 4-5 (a) where the baseline is at approximately 0 V. The different baselines are caused by the leakage of the background light. In our design, the LED light is parallel to the two emission filters, which will cause some light leakage. Although the emission filter is a band-pass filter, some background light still could pass through the filter. In the ideal situation, the baseline should be 0 V. Once the background light passes through the filter, the baseline will be decreased due to the designed circuit. The quality of the emission filter determines the level of the light leakage. The two emission filters come from two different companies, and their quality and performance are different.

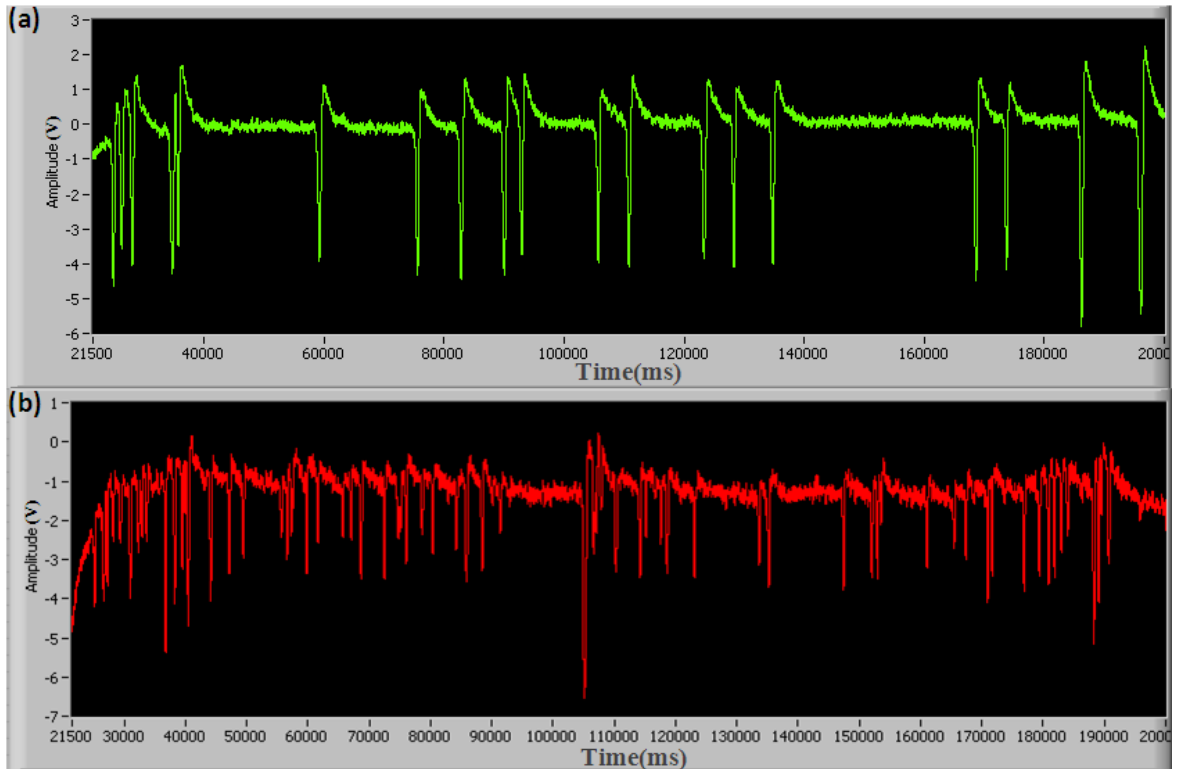


Figure 4-5 An example of the detected signals from a sample containing 7.0 μm Dragon Green fluorescent beads (a) and 7.0 μm Flash Red fluorescent beads (b). The ratio of the Dragon Green fluorescent beads to the Flash Red fluorescent beads is 1 to 3.

In order to examine the consistency and accuracy of the miniature two-wavelength fluorescent detection system developed in this study, mixtures of fluorescent particles were tested. Two groups of experiments were conducted with two different ratios of the particles. Each sample was tested at least 3 times. Table 4-1 displays the number of detected particles by the dual-wavelength detection system. For comparison, the same sample was analyzed concurrently by a commercial FACSvantage Cell Sorting Flow Cytometer (Becton-Dickinson, San Jose, CA, USA). Table 4-1 also lists the results obtained by the commercial flow cytometer. As an example, Figure 4-6 shows the percentage distributions of the particles in experiments 1, 2 and 3, determined by using the commercial flow cytometer. As seen in Table 4-1, overall, the result demonstrated the dual-wavelength fluorescent detection system developed in our study has a good agreement with the commercial flow cytometer.

Table 4-1 Comparison of the ratios of particles/cells detected by the device of this study and a commercial flow cytometer. PD stands for photo-detector.

		Chip1	Chip2	Chip3	Std. dev. (CV%)	Flow Cytometer
Exp. 1						
green/red beads	PD 2, (635nm, 690nm)	43	35	35		22.5%
	PD 1, (488nm, 520nm)	136	126	100		77.5%
	Ratio (percentage %)	31.6	28.6	35.0	3.20 (10%)	29.0
Exp. 2						
green/red beads	PD 2, (635nm, 690nm)	115	113	118		50.8%
	PD 1, (488nm, 520nm)	114	101	105		49.2%
	Ratio (percentage %)	100.9	111.9	112.4	6.50 (5.9%)	103.3
Exp. 3						
green/red cells	PD 1, (488nm, 520nm)	45	70	43		24.7%
	PD 2, (635nm, 690nm)	129	190	135		75.3%
	Ratio (percentage %)	34.9	36.8	31.9	2.47 (7.1%)	32.8

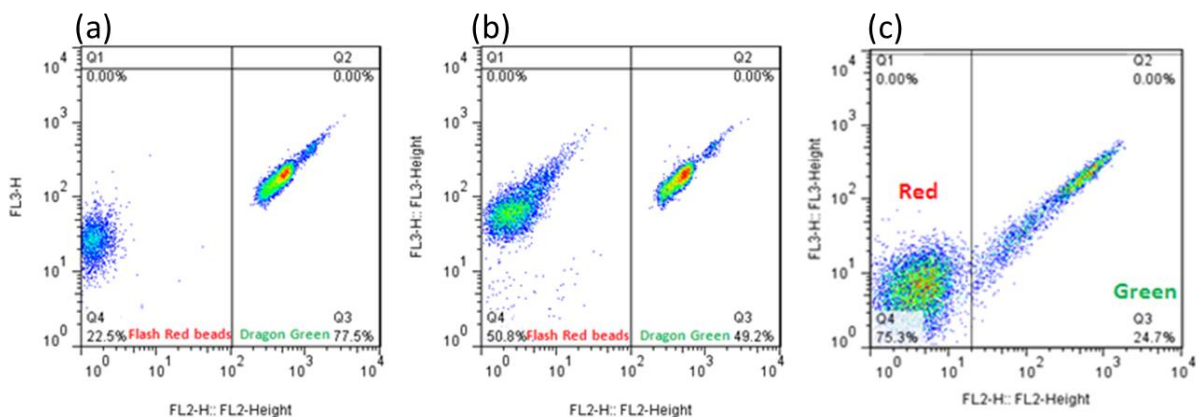


Figure 4-6 The number counts for two fluorescent particles determined by a commercial flow cytometer. (a) The counting result for two different types of fluorescent particles in Exp. 1 in Table 1. (b) The counting result for two different types of fluorescent particles in Exp. 2 in Table 4-1. (c) The counting result for two different types of fluorescent particles in Exp. 3 in Table 4-1.

While the miniaturized two-wavelength detection system was developed and has proved the concept in this study, further effort should be focused on increasing the sensitivity and achieving high-

throughput capability. In order to minimize the volume and the cost, the optical detection system in this study uses a LED instead of the lasers, and simple photo-detectors instead of the photomultiplier tubes. These may limit the sensitivity of the detection. For Now, 5 μm particles/cells can be detected. One possible way to increase the sensitivity may be the use of a UV/blue LED instead of the blue/red LED as the excitation light source. In comparison with the UV/blue fluorescence, the red/infrared fluorescence is much weaker under the same condition and it needs more energy to be excited. In order to increase the throughput, higher particle concentrations are required. However, when the particle concentration is high in the suspension, the chance of particle overlapping in the detecting spot is increased, as observed in the experiments. Therefore, future research must consider how to introduce flow focusing into the microfluidic chip to solve this problem. In addition, in order to avoid overlapping or double counting of the particle, it should reduce the excitation beam size. However, due to the compact structure of this system, there is no space to add such a focusing lens. Future research will consider to integrate the focusing lens into the microfluidic chip.

4.4 Concluding remarks

A fluorescence-activated particle counting system is developed based on the electrokinetically-induced pressure-driven flow and a miniaturized dual-wavelength fluorescent detection method. The microfluidic chip has a simple kernel structure of a main L-shaped microchannel and one pumping channel. The EOF flow in the pumping channel induces a pressure difference in the L-shaped microchannel to move the particles. The novel microfluidic chip eliminates the disadvantages of both the pressure pumping method and the electroosmotic pumping method. On the optical detection side, two excitation lights are provided by a single LED from one side of the microchannel and the two emission lights are captured by two photo-detectors from the top and the bottom of the chip. The advantages of this optical detection system is obvious. First, all the components are assembled into a small space. Second, it is easy to do the alignment. For each test, the step of optical alignment is eliminated. It only needs to replace the microfluidic chip. Third, the multiple fluorescent detection is realized by this system. It can detect one kind of fluorescent particles/cells and also can detect two different kinds of fluorescent particles/cells simultaneously. This design of the two-wavelength fluorescent detection system leads to a significant reduction of the volume and the cost, in comparison with other microfluidic fluorescent detection devices reported in literature.

Chapter 5

Study of a Novel Flow Focusing Method in a Microfluidic Chip for Dual-wavelength Fluorescent Detection of Particles

5.1 Introduction

Nowadays, flow cytometer becomes an essential equipment in many fields, such as biology and medicine due to the high-throughput quantification of single particle and continuously counting and sorting the particles. However, conventional flow cytometer is large, complex, and expensive. Specially, the consumption of sample volume is huge. There is much interest in reducing operational cost, complexity of the system, and consumption of sample volume.¹³⁵⁻¹³⁹ Therefore, Lab-on-a-chip technique have been used to manipulate liquid flows on chips for counting and sorting particles or cells.¹⁴⁰⁻¹⁴⁵

Replacing the flow chambers in conventional flow cytometer with the microfabricated flow cell is one of the most promising ways. Generally, the particle/cell focusing can be realized by two approaches: passive focusing¹⁴⁶⁻¹⁵⁰ and active focusing.¹⁵¹⁻¹⁶¹ In the first approach, it makes use of the converging channels to line particles or cells without additional energy source. In the latter approach, the external energy source such as pressure drop and electrical field must be used to drive the focusing stream. In our group, Xiangchun Xuan¹⁶² firstly investigated the electrokinetic focusing and the accelerated electrophoretic motion of focused particles and cells in microfluidic cross-channels. The effects of voltage ratio, particle size, particle property, and particle trajectory are examined. The electrokinetic manipulation of particle/cell in microchannels demonstrated in this work can be used to develop integrated lab-on-a-chip devices for the studies of cells. However, as mentioned in Chapter 2, the electrokinetic method may cause lots of problems such as pH change, bubbling, destroying cell membrane and so on. Therefore, in this chapter, a novel method based on the electrokinetic force to generate the sheath flows for flow focusing is proposed.

5.2 Principle of flow focusing method

A schematic diagram of the proposed method is shown in Figure 5-1. The flow focusing system consists of a T-shaped main microchannel and two T-shaped branch microchannels. The channel A-B is used as an electro-osmotic pump where the electro-osmotic flow is generated by applying DC

(direct current) voltages via electrodes inserted in reservoirs A, B and O. The direction of the EOF (electro-osmotic flow) is from O to both A and B due to the polarity of the electrodes shown in Figure 5-1. The channels C-D and C'-D' also are used as two electro-osmotic pumps. The direction of the EOF is from both C (C') and D (D') to the O' (O'') due to the reversed polarity of the electrodes shown in Figure 5-1.

After applying the voltages on these reservoirs, the EOF is generated in the channel A-B, C-D and C'-D'. As shown in Figure 5-1, the green arrows show the direction of the flow which is pumped into reservoirs A and B continuously. As mentioned in Chapter 3 and 4, the cross-junction area near the O has a negative pressure which may induce a pressure-driven flow in the main vertical channel. Meanwhile, the liquid is pushed into the two branch channels from the reservoirs C, D, C' and D' due to the EOF generated in the channels C-D and C'-D', as shown in Figure 5-1 by the purple and yellow arrows. Because of the electrokinetically-induced pressure-driven flow in the vertical channel, there are three flow streams are formed: two sheath flows and the sample stream. These two sheath flows are sucked into vertical microchannel along the channel wall. The sample steam (red arrows) from the sample inlet will then be squeezed by these two sheath flows. By using this method, the flow focusing is easily realized without moving parts, external tubing, valves and syringe pumps.

5.3 Theory

In this section, formulas are developed to predict the focused stream in the proposed method. The structure of the microchannel is shown in Figure 5-1. According to the fluidic continuity, for a fixed period of time, how much volume of the liquid is pumped into the microsystem means how much volume of the liquid will flow out the microsystem. It can be described by the flow rate:

$$Q_{in} = Q_{out} \quad (5-1)$$

In this microchip, we can make sure that the liquid flows into the microchannel from the inlet C, D, C' and D'. The liquid is pumped out from the outlet A and B due to the direction of the net flow. However, the flow direction of the sample inlet is unknown, which is determined by the difference between the net inflow and the net outflow. However, it should be noted that the liquid should flow out from the sample inlet in our study. Thus, the sample inlet is assumed as a part of Q_{in} . After applying the voltages at the reservoirs, EOF is generated in the channel A-B, C-D and C'-D'. According to the fluidic continuity, it can be described by Equation (5-1):

$$Q_A + Q_B = Q_C + Q_D + Q_{C'} + Q_{D'} + Q_x \quad (5-2)$$

where Q_A , Q_B , Q_C , Q_D , $Q_{C'}$, $Q_{D'}$ and Q_x are the flow rate at the outlet A and B, inlet C, D, C' and D' and sample inlet, respectively.

The channels A-B, C-D and C'-D' are perfectly symmetric, therefore, Equation (5-2) can be rewrote as

$$2 \cdot Q_A = 4 \cdot Q_C + Q_x \quad (5-3)$$

The zeta potential at the non-conducting channel wall ζ_w is constant and the value depends on the properties of the solid material and the liquid solution. According to Helmholtz–Smoluchowski formula, the electro-osmotic flow velocity is

$$\vec{v} = \vec{v}_{eo} = -\frac{\epsilon_0 \epsilon_r \zeta_w}{\mu} \vec{E} = -\frac{\epsilon_0 \epsilon_r \zeta_w V}{\mu d} \quad (5-4)$$

where V is the applied voltage between the electrodes and d is the distance separating the electrodes, ϵ_0 and ϵ_r are the dielectric constant in vacuum and the dielectric constant of the solution, respectively. If k is used to represent the constants, the Equation (5-4) can be rewritten as

$$\begin{cases} v_{eof} = k \cdot V \\ k = -\frac{\epsilon_0 \epsilon_r \zeta_w}{\mu d} \end{cases} \quad (5-5)$$

As mentioned in Chapter 3, a pressure-driven backward flow is generated in the channel A-B after applying the electric field. This backward flow can reduce the net flow velocity. However, from the simulation result, it is found that decreasing the cross-section area of the horizontal channel can increase the net flow velocity. Here, the influence of the pressure-driven backward flow in the horizontal channel is ignored. It is assumed that the net flow velocity is equal to the EOF velocity. The flow rate is only determined by the EOF generated in the channel A-B, C-D and C'-D', it can be calculated as

$$\begin{cases} Q_A = v_{eof-A} \cdot A = k \cdot A \cdot V_A \\ Q_C = v_{eof-C} \cdot A = k \cdot A \cdot V_C \end{cases} \quad (5-6)$$

Where A is the cross section area of the channels A-B, C-D and C'-D' (We use the same cross section area for the channels A-B, C-D and C'-D'). V_A and V_C are the applied voltages at A and C. If Equation (5-6) is substituted into Equation (5-3), it can be rewritten as

$$V_A = 2 \cdot V_C + \frac{Q_x}{2 \cdot k \cdot A} \quad (5-7)$$

From Equation (5-7), the relationship among the applied voltages can be obtained. There are three possibilities.

- I. If $V_A = 2V_C$, $Q_x = 0$. There is no liquid flowing into or flowing out of the sample inlet.
- II. If $V_A < 2V_C$, $Q_x < 0$. It means that part of the liquid flows into the sample inlet.
- III. If $V_A > 2V_C$, $Q_x > 0$. It means that the liquid flows out of the sample inlet.

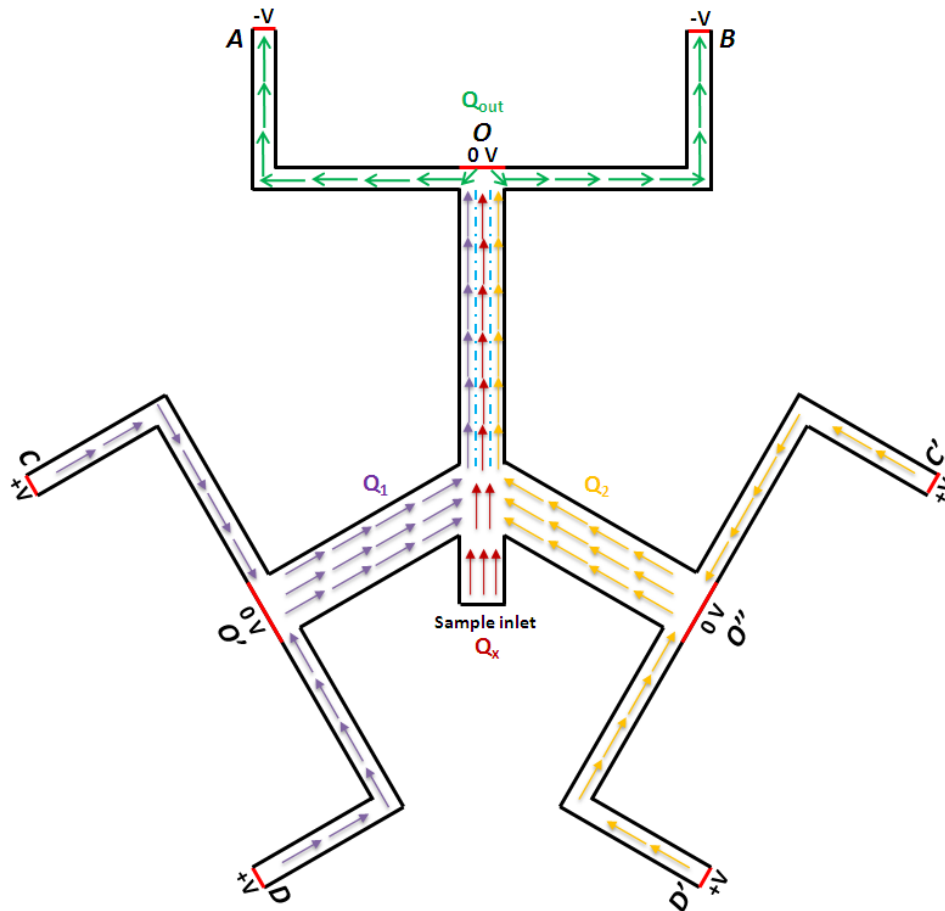


Figure 5-1 Schematic diagram of the proposed method to generate electrokinetically-induced pressure-driven flow and two sheath flows.

5.4 Numerical study

Numerical model was studied to prove the proposed focusing method. In this study, COMSOL MULTIPHYSICS 4.2a was used to solve this numerical model. 800000 elements or more were used in all simulations to avoid the grid dependence. The numerical studies consist of two main parts. In the first part, it is desired to investigate the effectiveness of the proposed method of generating focusing flow in the T-shaped channel. In the second part, the motion of the particles is studied in the T-shaped channel.

5.4.1 Physical modeling

- *Electric field*

Once the voltages are exerted at the inlets of the system, the applied potential through the system is governed by Laplace's equation.

$$\vec{\nabla}^2 \Psi_e = 0 \quad (5-8)$$

And the local applied electric field strength is

$$\vec{E} = -\vec{\nabla} \Psi_e \quad (5-9)$$

The boundary conditions of the electric field are

$$\vec{n} \cdot \vec{\nabla} \Psi_e = 0 \text{ at the channel walls} \quad (5-10)$$

$$\Psi_e = \Psi_1 \text{ at inlet C, D, C' and D'} \quad (5-11a)$$

$$\Psi_e = \Psi_2 \text{ at outlet A and B} \quad (5-11b)$$

$$\Psi_e = 0 \text{ at Point O, O' and O''} \quad (5-11c)$$

- *Velocity field*

The velocity field is governed by the continuity equation and the momentum equation

$$\vec{\nabla} \cdot \vec{U} = 0 \quad (5-12)$$

$$\rho \left[\frac{\partial \vec{U}}{\partial t} + \vec{U} \cdot \vec{\nabla} \vec{U} \right] = -\vec{\nabla} P + \mu \vec{\nabla}^2 \vec{U} + \vec{E} \rho_e \quad (5-13)$$

where ρ and μ are the density and viscosity of the liquid, \vec{U} is velocity, ρ_e is the local net charge density, $\vec{\nabla}P$ is the pressure gradient. Considering a steady flow, and no pressure driven force, the boundary conditions are

$$P = 0 \quad \text{at inlets and outlets} \quad (5-14)$$

$$\vec{\nabla}P = 0 \quad \text{in the whole flow field} \quad (5-15)$$

Because the net charge density is non-zero only in the double layer, the body force $\vec{E}\rho_e$ is zero except in the double layers. The flow is driven by the interaction force between the applied electrical field and the net charge in the double layers. Generally the thickness of the EDL (electrical double layer) is negligible in comparison with the size of the microchannel. Therefore, there is no need to solve the flow field in the thin EDL. Instead, the velocity in the EDL is considered a constant and used as a slip velocity boundary for the flow field in the microchannel. The slip velocity boundary conditions are:

$$\vec{u} = \vec{u}_{eo} = -\frac{\varepsilon_0 \varepsilon_r \zeta_w}{\mu} \vec{E} \quad \text{at non-conducting walls} \quad (5-16)$$

Since the length of the incoming channels and the branch channels are assumed long enough, the inlet and outlet boundaries have no effect on the flow field.

- *Concentration field*

The concentration field of species is described by

$$\frac{\partial C}{\partial t} + \vec{U} \cdot \vec{\nabla}C = D \vec{\nabla}^2 C \quad (5-17)$$

where C is the concentration, D is the diffusion coefficient.

The boundary conditions are

$$C = C_0 \quad \text{at sample inlet ,} \quad (5-18a)$$

$$C = 0 \quad \text{at inlet C, D, C' and D'} \quad (5-18b)$$

$$\frac{\partial C_{t \geq 0}}{\partial n} = 0 \quad \text{at all the walls} \quad (5-18c)$$

and the initial concentration in the system is

$$C_{t=0} = 0 \quad (5-18d)$$

- *Motion of particle*

The motion of particles is defined by Newton's second law

$$m \frac{d^2x}{dt^2} = \mathbf{F} \left(t, x, \frac{dx}{dt} \right) \quad (5-19)$$

where x is the position of the particle, m the particle mass, and F is the sum of all forces acting on the particle. The density of the real particles used in the experiments is about 1.06 g/cm^3 , which is very close to the density of water (1 g/cm^3). Therefore, the particles are considered to suspend in the water. In the simulation, the gravity is ignored. Brownian motion is a body force which leads to random motion of particles. The Péclet number¹⁶³ gives the relative importance of hydrodynamic forces to Brownian motion. The Péclet number can be expressed by the Equation:

$$Pe = \frac{UL}{D} \quad (5-20)$$

where L is the characteristic length, U the velocity, D the diffusion coefficient. If the Péclet number > 1 , it means that hydrodynamic forces are dominant. For a sphere of one micron diameter in water at room temperature, D is around $0.44 \text{ } \mu\text{m}^2/\text{sec}$.¹⁶⁴ In the present study, the diffusion coefficient D should be an order of magnitude lower than that of one micron diameter sphere due to the large size of the particle ($7\text{-}10 \text{ } \mu\text{m}$). Therefore, the Péclet number is much bigger than 1. The effect of Brownian motion is ignored in this study.

The following parameters are used in the study:

- One pumping channel A-B of $25 \text{ } \mu\text{m}$ in width and 1cm in length; the main vertical channel of $100 \text{ } \mu\text{m}$ ($50 \text{ } \mu\text{m}$) in width and 5 mm in length;
- The microchannels C-D and C'-D' of $25 \text{ } \mu\text{m}$ in width and 1cm in length; the branch of $200 \text{ } \mu\text{m}$ in width and 3 mm in length;
- The height of the channel is $25 \text{ } \mu\text{m}$.
- The work solution is water. The density of water ρ is 1000 kg/m^3 , the viscosity of water is μ is $10^{-3} \text{ kg/m}\cdot\text{s}$, the relative permittivity ϵ is 80; the zeta potential ζ_w is -0.04V .

5.4.2 Result and discussion

- *Situation 1 — No voltage is applied at the outlet A, B and a certain voltage is applied at the inlet C, D, C' and D'*

In this case, there is no EOF flow in the channel A-B since no voltage is applied. Meanwhile, 50 V is applied at the inlet C, D, C' and D' and 0 V is applied at Point O' and O''. The liquid are pumped into the branches from the inlet C, D, C' and D' continuously due to the EOF flow. Since the cross-section of the channel A-B is very narrow (25 μm), the flow resistance of it will be huge. Thus, the liquid will flow into the sample inlet. From the simulation result shown in Figure 5-2, it can be seen that if there is no pumping force in the channel A-B, the liquid will not flow into the vertical channel.

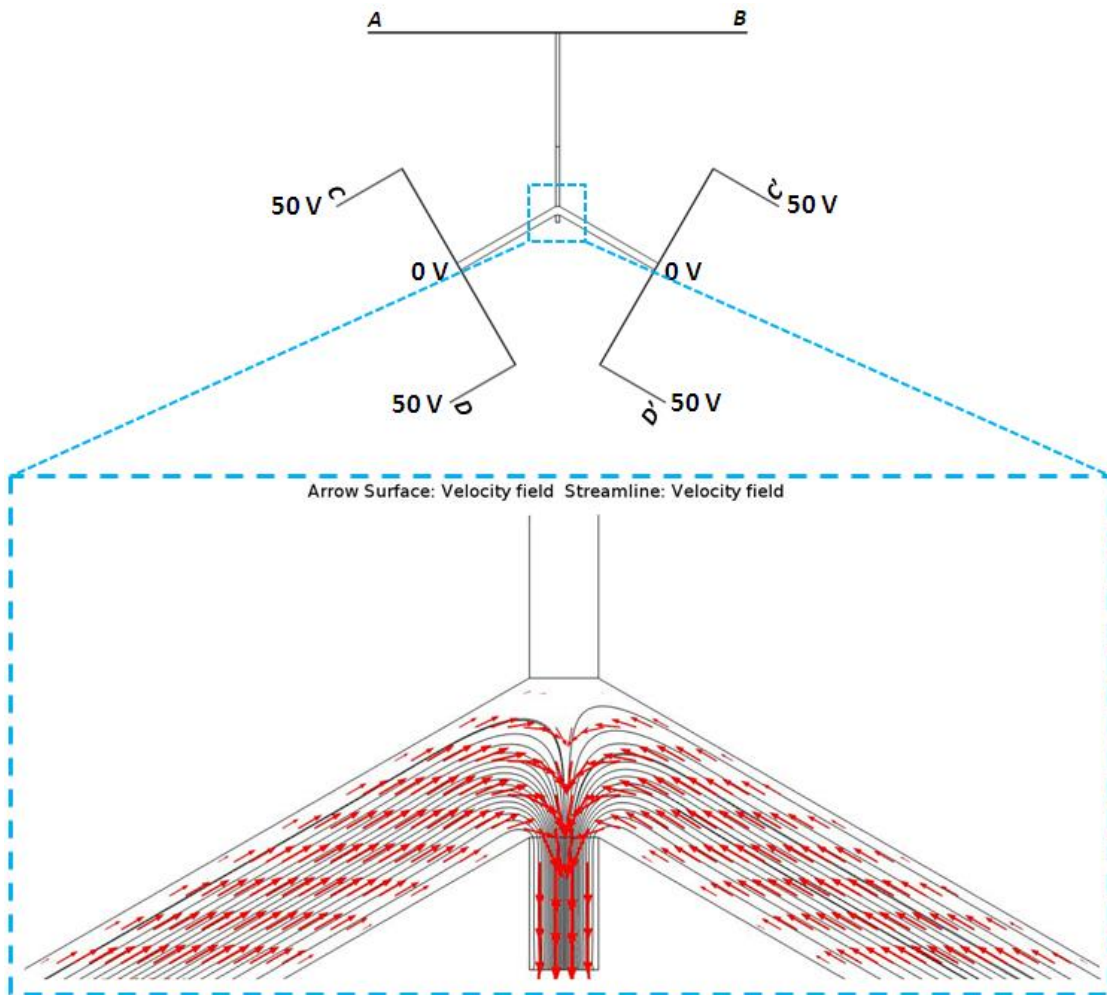


Figure 5-2 The velocity profile in the T-shaped microchannel. The red vectors and stream line show the direction of the flow field (50 V at C, D, C', D' and 0 V at Point O' and O'').

- **Situation 2** — *No voltage is applied at the inlet C, D, C', D' and a certain voltage is applied at the outlet A, B*

In this case, there is no EOF flow in the channel C-D and C'-D' because no voltages are applied. Therefore, there is no liquid being pumped into the branches from the inlet C, D, C' and D'. Meanwhile, -50 V is applied at the outlet A, B and 0 V is applied at Point O. The liquid are pumped out from the outlet A and B continuously due to the EOF flow. From the result shown in Figure 5-3, we see that in this situation, most of the liquid is sucked from the sample inlet. There is no sheath flow generated from the branch T-shaped channels.

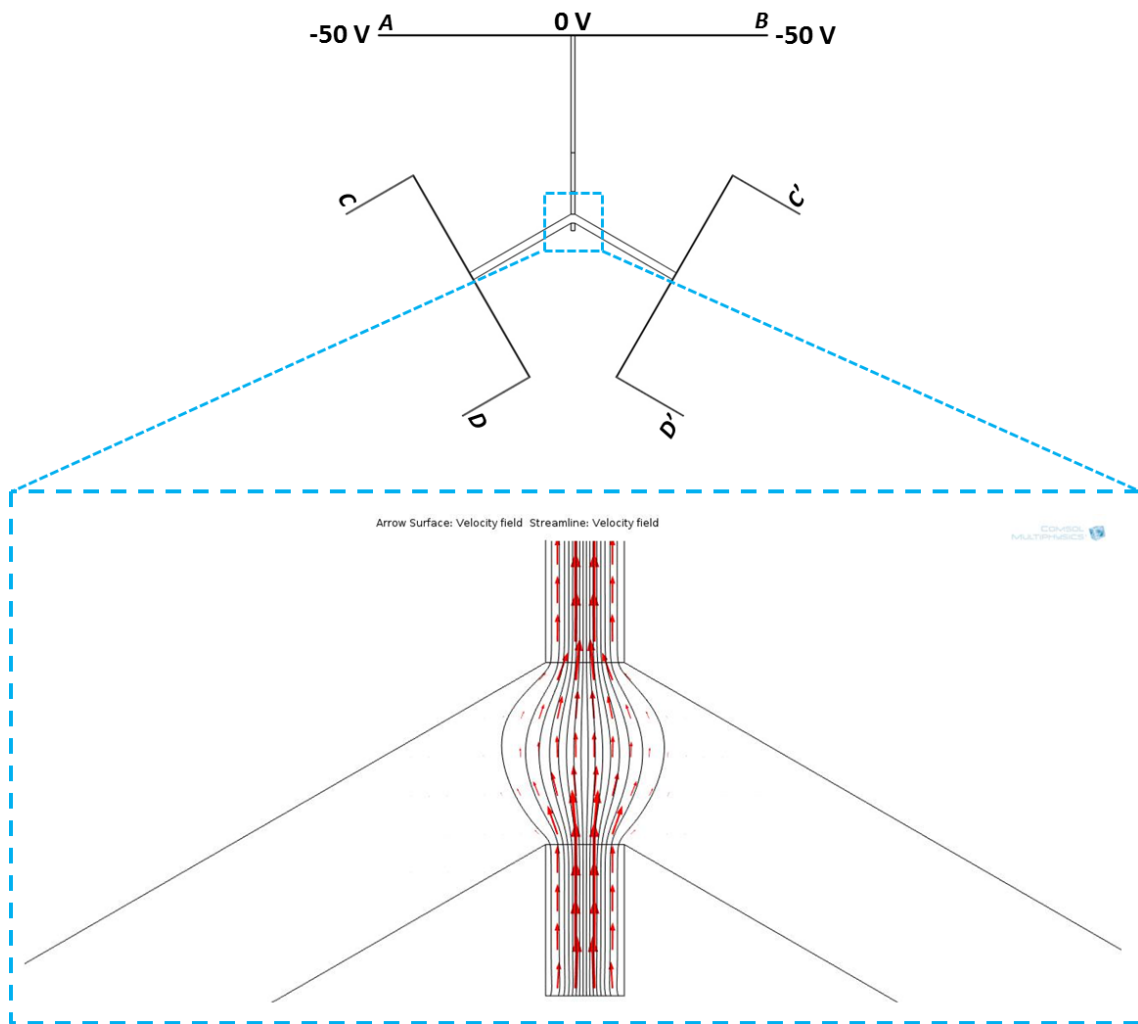


Figure 5-3 The velocity profile in the T-shaped microchannel. The red vectors and stream line show the direction of the flow field (-50 V at A, B and 0 V at Point O).

- ***Situation 3 — voltages are applied at the outlet A, B and the inlet C, D, C' and D'***

In this case, the voltages are applied at the outlet A, B and the inlet C, D, C' and D' based on Equation (5-7). The simulation results are highly corresponding to the mathematical analysis. Figure 5-4 shows that if $V_A = 2V_C$, there is no liquid flowing into or flowing out of the simple inlet. The velocity vectors and streamlines indicate that only the liquid which comes from the two branches will flow into the vertical channel. In addition, if $V_A < 2V_C$, the liquid which comes from two branches will not only flow into the vertical channel, but also flow into the simple inlet (Figure 5-5). However, when $V_A > 2V_C$, the liquid flows out of the sample inlet. From Figure 5-6, we can see that in the vertical channel, there are three streams. Two streams come from the two branches and one stream comes from the sample inlet. It is obvious that the liquid flowing from the sample inlet is squeezed in the vertical channel by the two sheath flows which come from two branches. The complicated calculation of concentration field in such microchannel networks has been done for a better visualization, as shown in Figure 5-4 to Figure 5-6.

From the above simulation results, it is distinctly shown that the effect of the flow focusing is controlled by the applied voltages at different reservoirs. Actually, this is a pushing-sucking process in the microchannel network. The channel A-B is used as the pump to generate the sucking force. While the two branch channels push the liquid into the main vertical channel, the liquid is sucked out by the EOF pump.

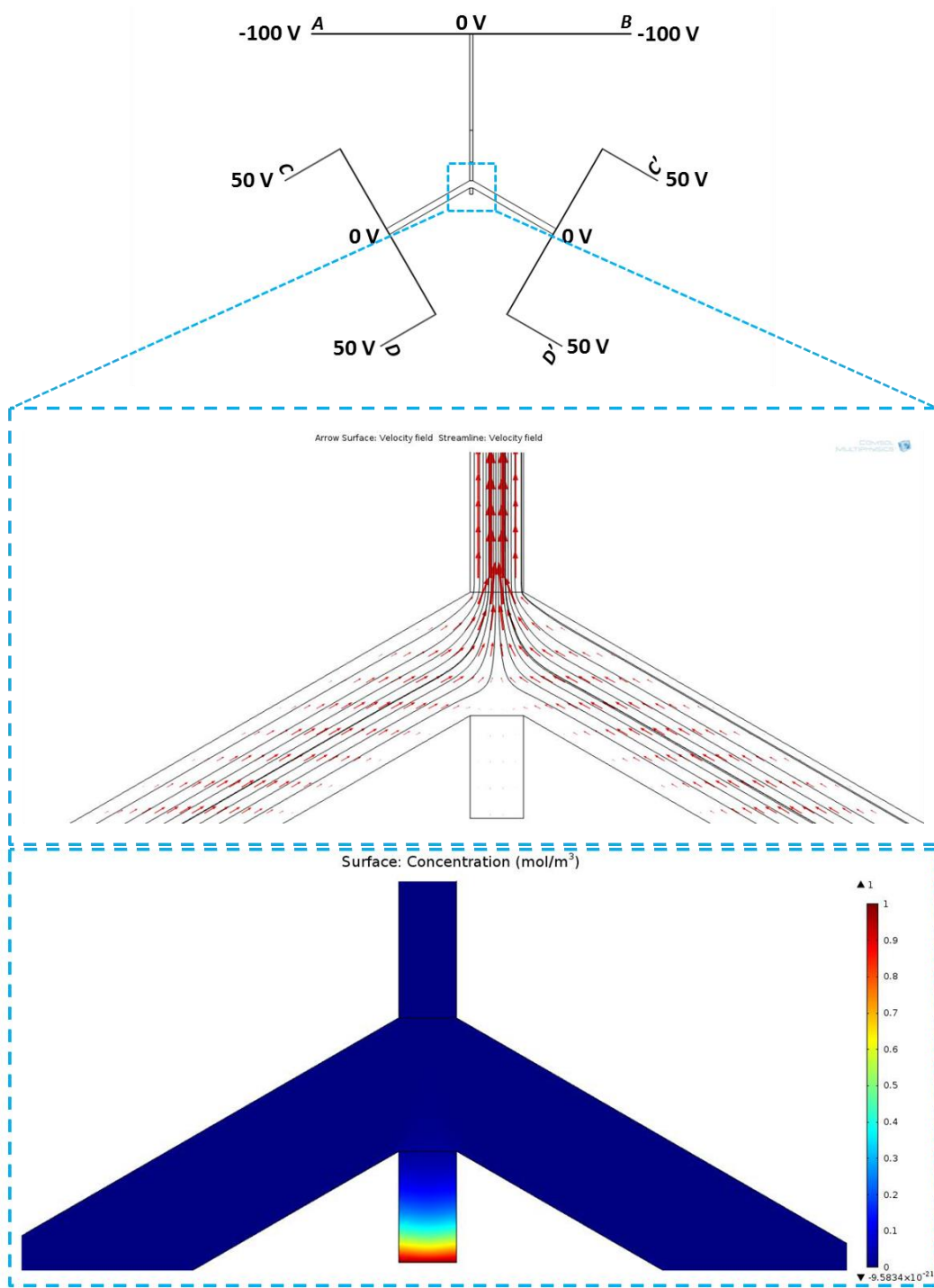


Figure 5-4 The velocity profile in the T-shaped microchannel. The red vectors and stream line show the direction of the flow field. The bottom plot shows the concentration field in the in the T-shaped microchannel (-100 V at A, B and 0 V at Point O; 50 V at C, D, C', D' and 0 V at Point O' and O'').

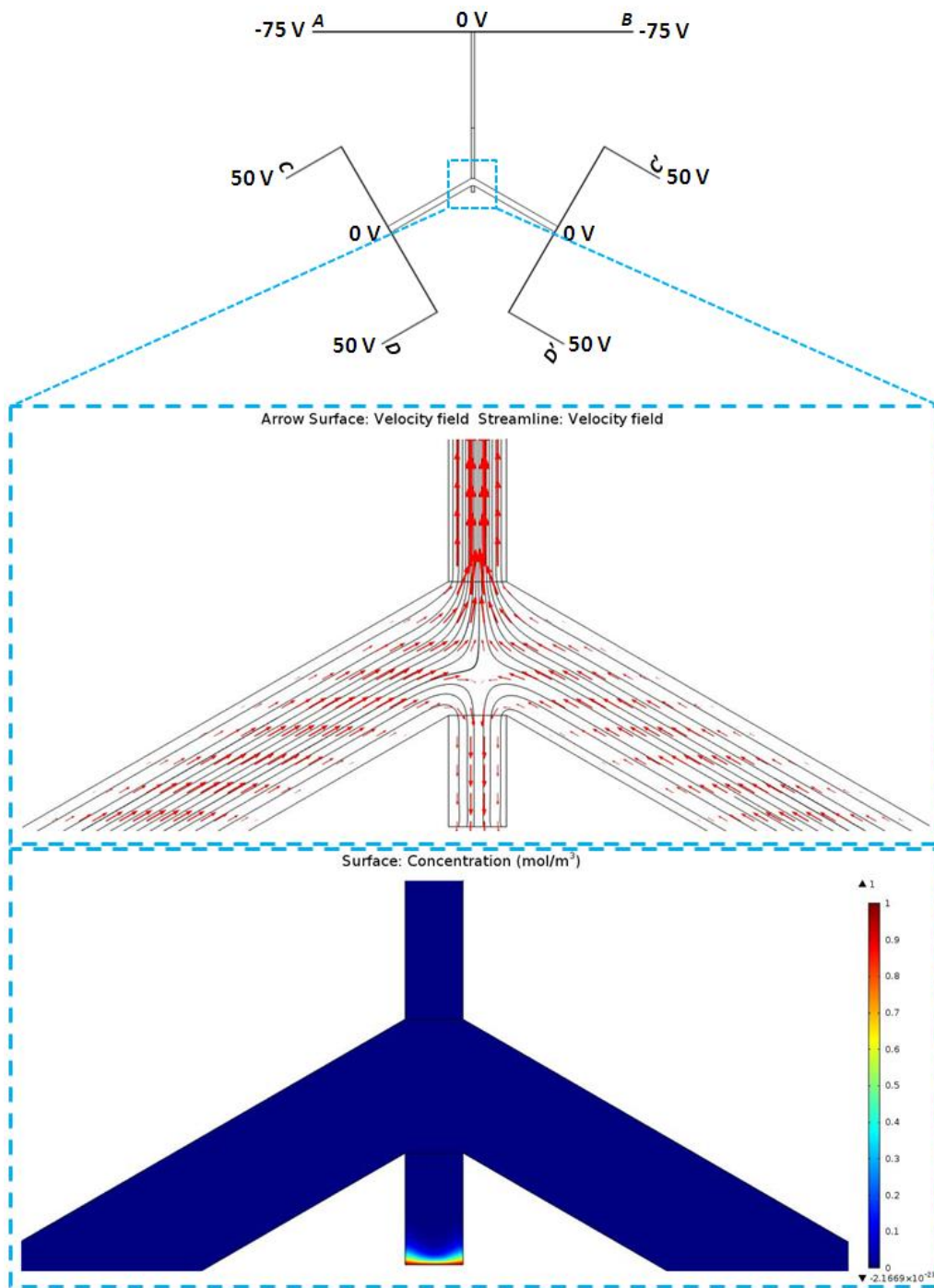


Figure 5-5 The velocity profile in the T-shaped microchannel. The red vectors and stream line show the direction of the flow field. The bottom plot shows the concentration field in the in the T-shaped microchannel (-75 V at A, B and 0 V at Point O; 50 V at C, D, C', D' and 0 V at Point O' and O'').

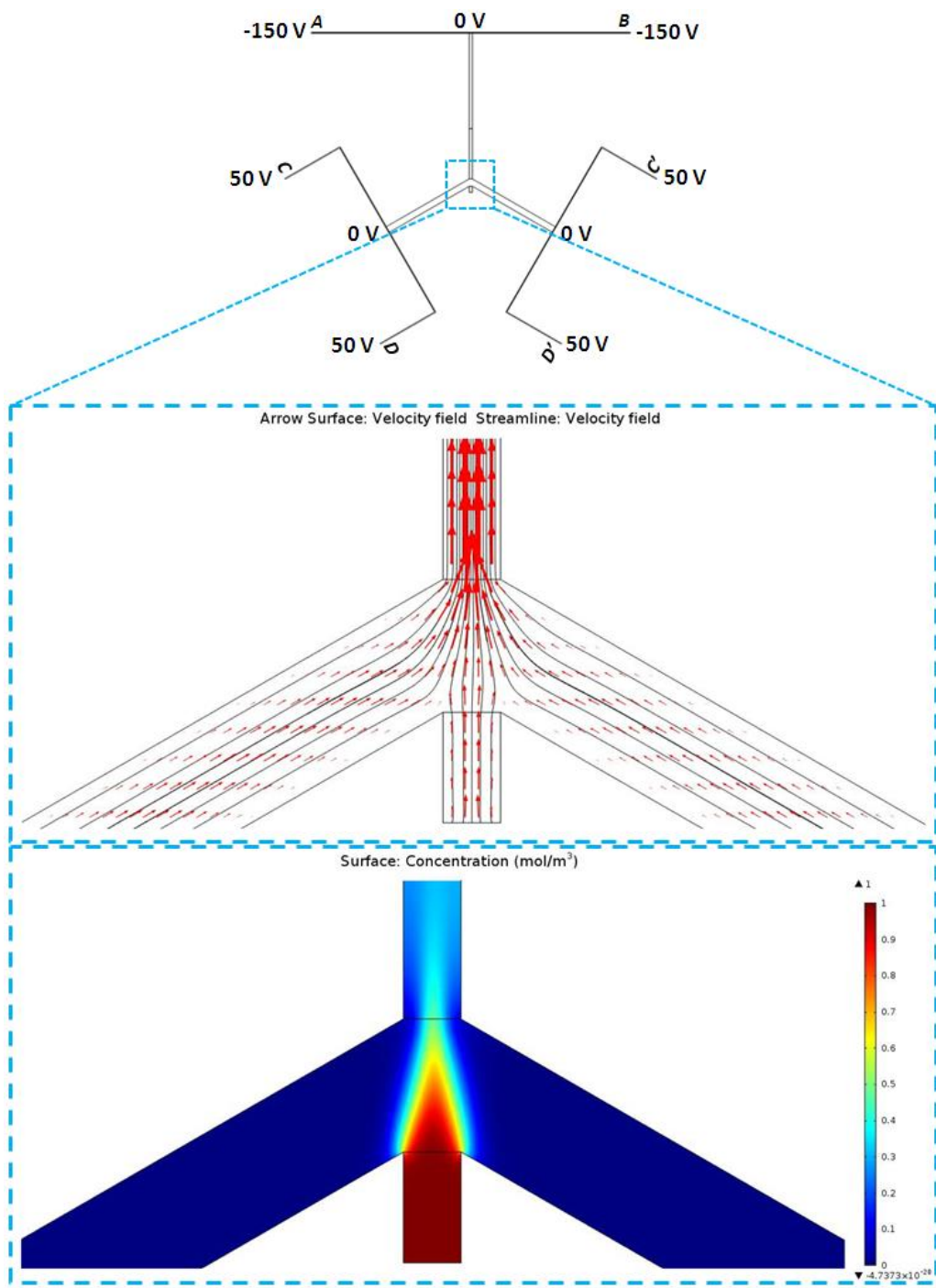


Figure 5-6 The velocity profile in the T-shaped microchannel. The red vectors and stream line show the direction of the flow field. The bottom plot shows the concentration field in the in the T-shaped microchannel (-150 V at A, B and 0 V at Point O; 50 V at C, D, C', D' and 0 V at Point O' and O'').

- *Situation 4 — The simulation of the motion of particles in the vertical channel*

This study considers the three-dimensional transient motion of the particles in the proposed T-shaped rectangular microchannel. The objective is to obtain a fundamental understanding of the characteristics of the particle motion in the complicated T-shaped microchannel. The simulation model and parameters are mentioned previously. First, the flow field and the electrical field are solved. Then, the particles are released from the sample inlet. This simulation describes the transient motion of the particles as it will move with the fluidic flow in the vertical channel. Moreover, it also illustrates how the particles are focused in the center line of the vertical channel by the two sheath flows. Figure 5-7 shows the sequential images of the simulation of particle's motion in the vertical channel. As mentioned before, the particle motion is caused by the continuous electrokinetically-induced pressure-driven flow in the channel. In Figure 5-7, it is shown that the initial position of the particles is at the entry of the sample inlet and the initial velocity of them is zero. For a good visualization, we assume that 1000 particles (the diameter of particle is 10 μm) are released. When the electric potentials are applied at the outlets and inlets, the particles begin to move. It is obvious that a parabolic velocity profile of the particles is formed due to the electrokinetically-induced pressure-driven flow. When the particle stream enters into the vertical channel, it is squeezed by the two sheath flow immediately.

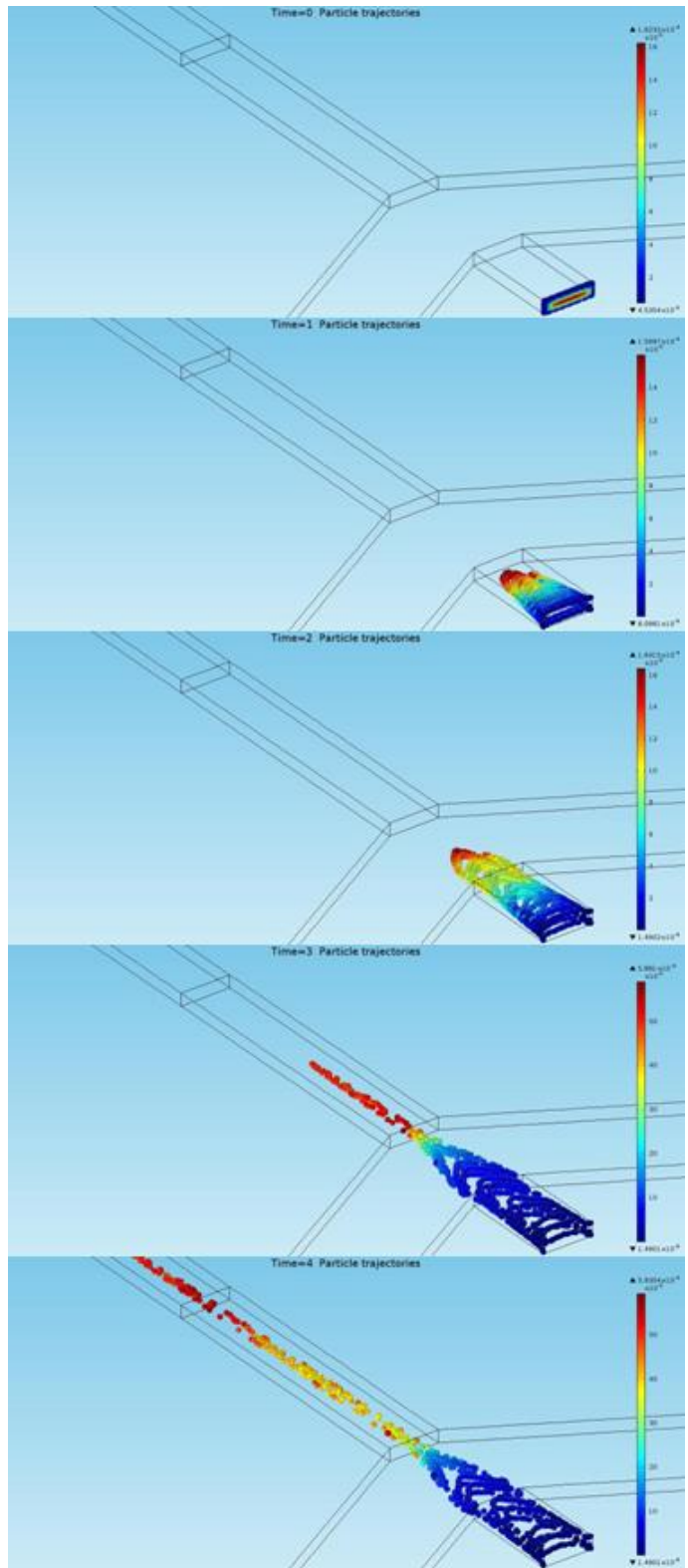


Figure 5-7 Sequential images of the simulation of particle's motion in the channel. 1000 particles of 10 μm diameter are released at the sample inlet (-150 V at A, B and 0 V at Point O; 50 V at C, D, C', D' and 0 V at Point O' and O'').

- ***Situation 5 — The simulation of the flow focusing effect with applied electric potentials***

In developing the current theoretical models for predicting the width of the two-dimensional hydrodynamically focused streams in rectangular microchannels, this study makes the following assumptions: the flow in the microchannels is steady and laminar; the microchannel is filled with water; the inlet, side and outlet channels are of the same height. In this case (Figure 5-1), the width of the focus stream is accurately approximated by a ratio of the flow rates with:

$$\frac{w_f}{w} = \frac{Q_x}{Q_x + 2 \cdot Q_b} \quad (5-21)$$

where Q_b and Q_x are the flow rate at branch channel and sample inlet, respectively. w_f and w are the width of the focusing stream and the width of vertical channel (100 μm). In symmetric hydrodynamic flow focusing in rectangular microchannel, the flow rates from the two side channels are equal, i.e. $Q_b = Q_C + Q_D$. According to Equation (5-3) and (5-6), Equation (5-21) can be rewrote as

$$\frac{w_f}{w} = \frac{Q_x}{Q_x + 4 \cdot Q_C} = 1 - 2 \cdot \frac{Q_C}{Q_A} = 1 - 2 \cdot \frac{V_C}{V_A} \quad (5-22)$$

where Q_A and Q_C are the flow rate at the outlet A and the inlet C. V_A and V_C are the applied voltages at the outlet A the inlet and C. From Equation (5-22), it is very easy to predict the width of the flow focusing stream. For example,

- -100 V is applied at outlet A and 50 V is applied at inlet C, $\frac{V_C}{V_A} = \frac{1}{2}$, $\frac{w_f}{w} = 0$, $w_f = 0 \mu\text{m}$
- -150 V is applied at outlet A and 50 V is applied at inlet C, $\frac{V_C}{V_A} = \frac{1}{3}$, $\frac{w_f}{w} = \frac{1}{3}$, $w_f = 33.3 \mu\text{m}$
- -200 V is applied at outlet A and 75 V is applied at inlet C, $\frac{V_C}{V_A} = \frac{3}{8}$, $\frac{w_f}{w} = \frac{1}{4}$, $w_f = 25 \mu\text{m}$
- -300 V is applied at outlet A and 125 V is applied at inlet C, $\frac{V_C}{V_A} = \frac{5}{12}$, $\frac{w_f}{w} = \frac{1}{6}$, $w_f = 16.67 \mu\text{m}$

From the above theoretical analysis, it is clearly shown that the width of the flow focusing stream is controlled by the applied voltages. With increasing the applied voltage at the horizontal channel (correspondingly, increasing the applied voltage at the branch channels), the flow focusing stream is getting narrow. In the experiments, the applied voltages can be easily determined by the size of the particle.

In the numerical study, to prove the theoretical analysis, the different voltages are applied at the inlet and outlet to investigate how the applied voltages can influence the focusing stream. According to the Equation (5-7), the focusing flow can be formed provided by $V_A > 2V_C$. Here, -150 V, -200 V and -300 V are applied at outlets A, B, respectively. 50 V, 75 V and 125 V are applied at inlets C, D, C', D', respectively. For a good visualization, we consider that 1000 particles (diameter is 10 μm) are released from the sample inlet. Figure 5-8 illustrates the top view of the particle's motion under three different conditions. In the previous simulations, Figure 5-4 shows that if $V_A = 2V_C$, there is no liquid flowing into or flowing out the simple inlet. From the above calculation, if $V_A = 2V_C$, the width of the flow focusing stream is 0 μm . From Figure 5-8 (a), the focusing stream occupies approximately 1/3 of 100 μm width of vertical channel. When increasing the applied voltages, the width of the focusing stream is decreasing. In Figure 5-8 (c), the width of the focusing stream is squeezed to approximately 1/6 of 100 μm width of vertical channel. The theoretical analysis is highly agreed with the simulation results.

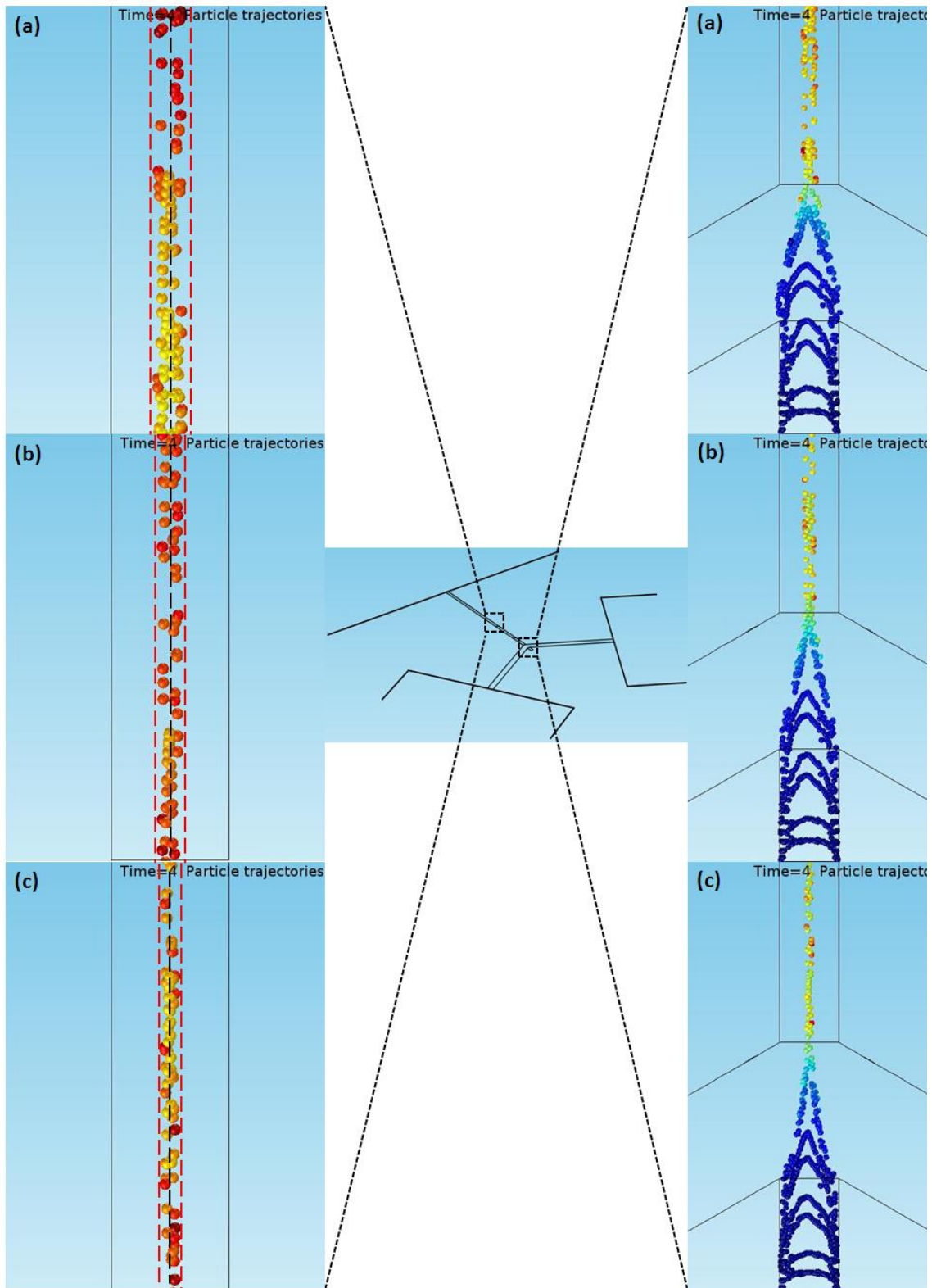


Figure 5-8 The top view of the vertical channel and the particle's motion. The red dashed lines show the focusing steam. The black dashed line is the center line of the vertical channel. (a) -150 V is applied at A, B and 0 V is applied at Point O; 50 V is applied at C, D, C', D' and 0 V is applied at Point O' and O''. (b) -200 V is applied at A, B and 0 V is applied at Point O; 75 V is applied at C, D, C', D' and 0 V is applied at Point O' and O''. (c) -300 V is applied at A, B and 0 V is applied at Point O; 125 V is applied at C, D, C', D' and 0 V is applied at Point O' and O''.

5.5 Experimental study

According to the simulation result, the novel flow focusing approach proposed has proven to be capable of focusing the particles in the T-shaped microchannel. In this section, the experimental results for verifying this novel approach is demonstrated. The experimental results have proved this method in this section. The particles are successfully focused in the microchannel based on the electrokinetically-induced pressure-driven flow.

5.5.1 Material and solution

In this experimental study, fluorescent particles and non-fluorescent particles of different sizes are used for visualizing the phenomenon: (1) 7.0 μm Dragon Green fluorescent beads (Excited Wavelength 480 nm, emission wavelength 520 nm, BD Biosciences, Fishers, IN, USA) mixed with 7.0 μm Flash Red fluorescent beads (Excited Wavelength 660 nm, emission wavelength 690 nm, BD Biosciences, Fishers, IN, USA), (2) carboxyl polymers microspheres (Bangs Laboratories Inc., Fishers, Canada) of 0.5 μm in diameter. For the flow visualization, Rhodamine B solution was used as an indicator, excitation and emission light wavelength of which are 540 and 625nm, respectively. Initially, the microchannel chip was filled with DI water.

5.5.2 Chip fabrication

A polydimethylsiloxane (PDMS) microfluidic chip is fabricated by using the soft lithography protocol (Figure 3-9). First, a master is prepared by spin coating a film of SU-8 negative photoresist onto a silicon wafer. After pre-baking, a photomask bearing the microchannel geometry is placed on the top of the film. The photoresist film covered with the mask is then exposed to UV light. After post-baking and developing, a master could be obtained. A 10:1 (w/w) mixture of PDMS polymer base and curing agent is then poured over the master and cured at 75⁰C for 3h after being degassed under vacuum. After this step, the PDMS slab is solidified on the master and then peeled off from the

master. Reservoirs are punched on the PDMS slab at the designed locations. Finally, the PDMS slab and a glass slide are bonded tightly after treating them in an oxygen plasma device for 30s to form the desired microchannel chip. In this design, the depth of the microchannels is 25 μ m.

5.5.3 Chip design

A schematic diagram and a photograph of the novel microfluidic chip for flow focusing are shown in Figure 5-9. The fluidic control system consists of ten reservoirs A, B, C, D, C', D', O, O', O'' and sample inlet, one main vertical microchannel of 100 μ m in width and 5 mm in length, and three pumping channel A-B, C-D and C'-D' of 25 μ m in width and 1cm in length, two branches of 200 μ m in width and 3 mm in length. There is a neck channel of 100 μ m in width and 100 μ m in length to connect the microchannels with reservoir O, O' and O''. The diameter of reservoirs A, B, C, D, C', D', sample inlet and O, O', O' are 3 mm, 3 mm, 3 mm, 3 mm, 3 mm, 3 mm, 3 mm and 1.5 mm, 1.5 mm, 1.5 mm, respectively. The reservoirs and the channels are initially filled with a buffer solution. The particle sample solution is added to the sample inlet finally.

5.5.4 Experimental setup and operation

The experimental workstation consisted of the following major components: the microfluidic chip, a fluorescence microscope and image system, three DC power supplies and a data acquisition system, as shown in Figure 3-11. The microfluidic chip was fixed on the observation platform of the microscope. The DC regulated power supply (CSI12001X, Circuit Specialists Inc., USA) was used to control the voltages applied to the different electrodes. A fluorescent microscope (AZ100, Nikon) with a high intensity illumination system and two kinds of the CCD camera (DS-Qi1Mc, Nikon and Retiga 2000R, Nikon) was used to visualize the motion of the liquid (dye solution) and the particles/cells inside the microchannel. The images were captured by the digital camera and digitized by the computer software (NIS-Elements BR 3.0).

The dye solution was used in the visualization experiments. Initially the reservoirs A, B, C, D, C', D' and O, O', O'' were filled with 6 μ L and 1.5 μ L of DI water, respectively. To start the experiment, 6 μ L of the sample solution was loaded to the sample inlet so that there was no pressure difference among these reservoirs. By applying different voltages at the two ends of the channel A-B, C-D, C'-D' and 0 V at O, O', O'', electro-osmotic flow was generated in the channels and consequently a pressure gradient and two sheath flows were produced in the vertical channel. All the images were obtained by a CCD camera.

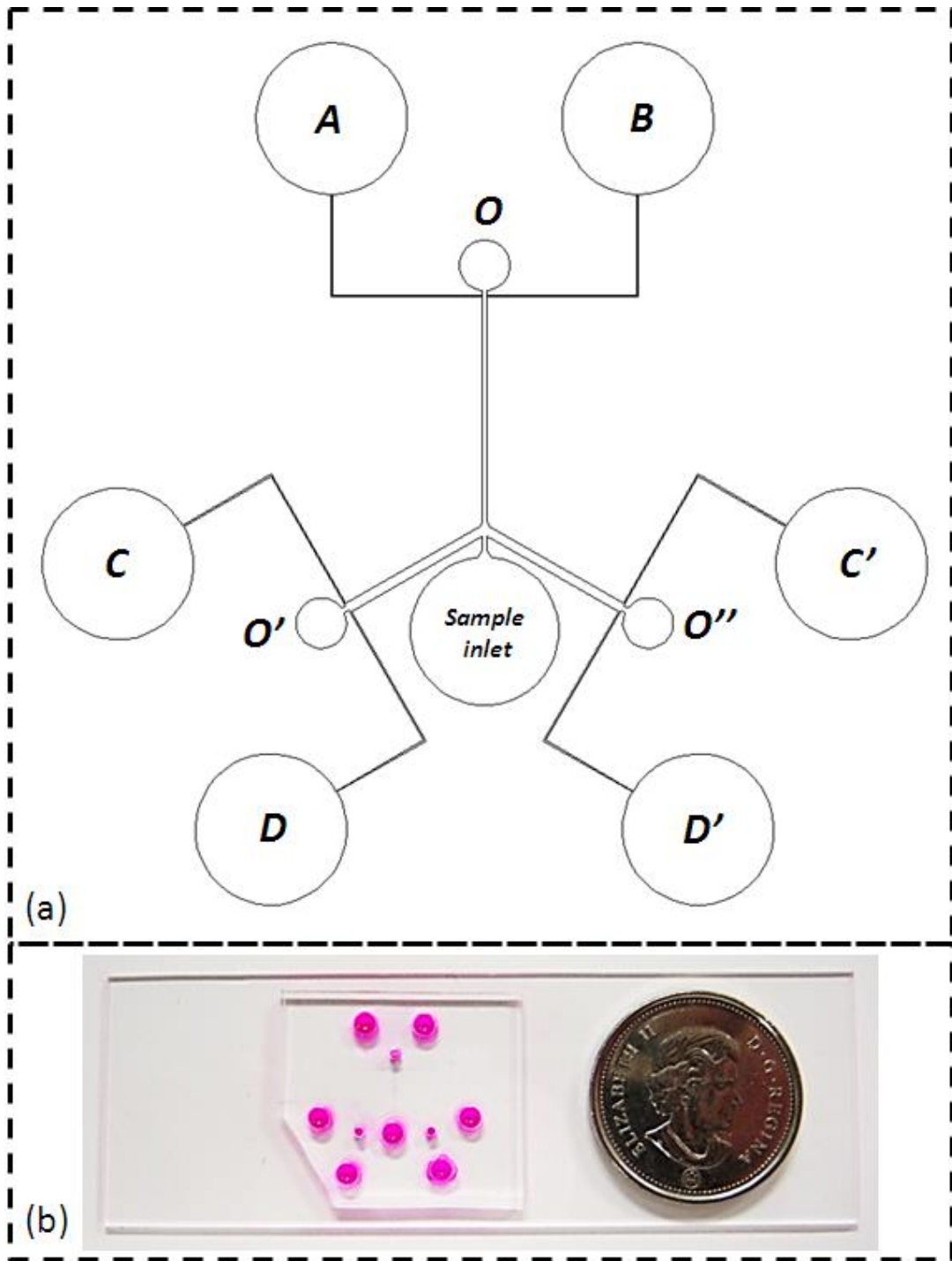


Figure 5-9 (a) Schematic diagram of a new method to generate electrokinetically-induced pressure-driven flow and two sheath flows in a microchannel. (b) A photograph of the microfluidic chip.

5.5.5 Experimental results

- *Demonstration of the focusing effect in the vertical microchannel*

To demonstrate that the liquid can be focused at the vertical channel by the applied electric fields, Rhodamine B was used as a tracer to visualize the flow field in the vertical channel. Figure 5-10 shows the fluorescent image and simulation image of the vertical channel during the dye solution traveling. As shown in Figure 5-10, the dye solution stream flows into the vertical channel due to the electrokinetic-induced pressure-driven flow and is focused by the two sheath flows. The highly close agreement is obtained between the experimentally observed fluorescent images and the simulated concentration field. This comparison is a strong evidence to prove our concept of the flow focusing.

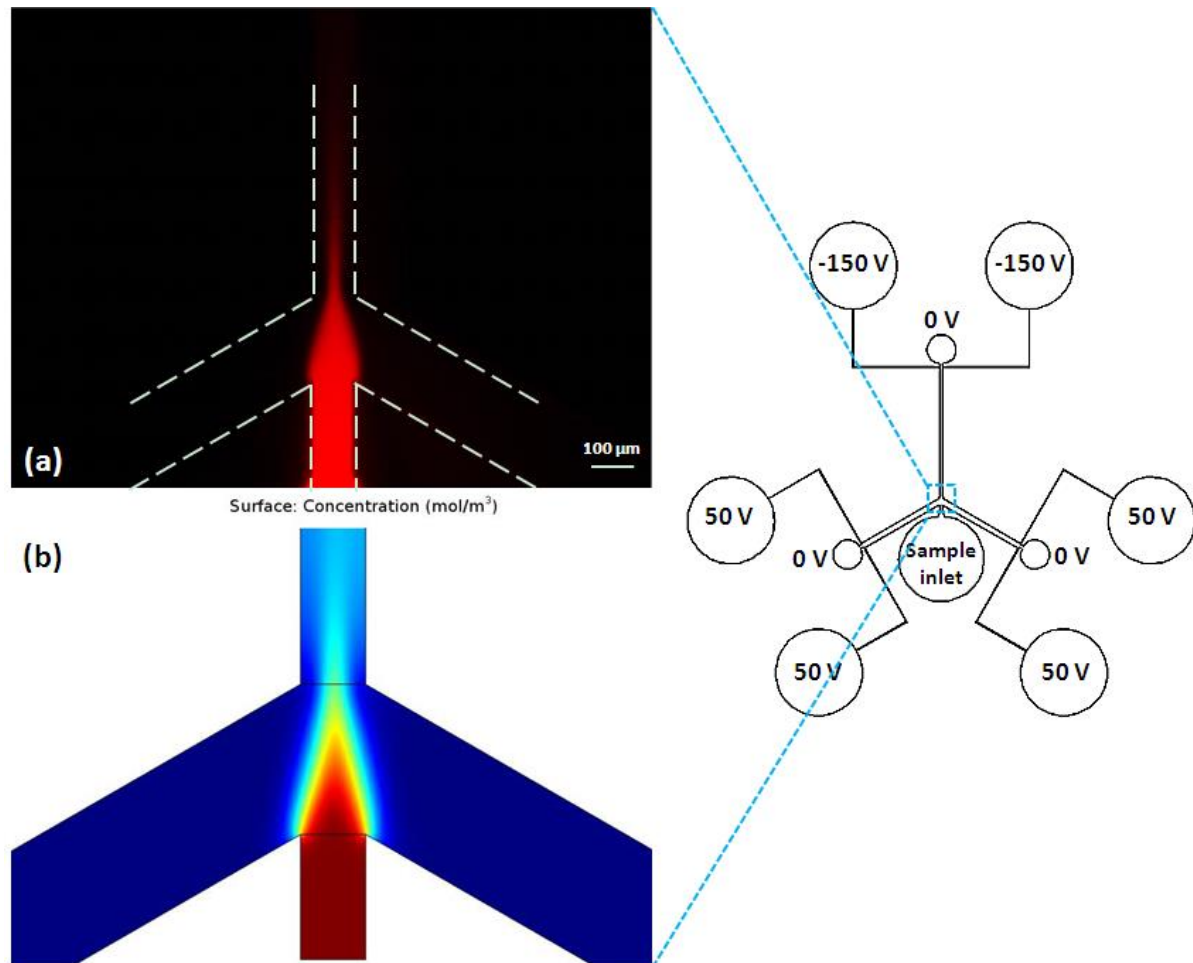


Figure 5-10 (a) A fluorescent image of flow focusing effect in the vertical microchannel. (b) A simulation image of flow focusing effect in the vertical microchannel (-150 V at A, B and 0 V at Point O; 50 V at C, D, C', D' and 0 V at Point O' and O'').

According to the Equation (5-7), the flow focusing can be formed when provided by $V_A > 2V_C$. The lower and higher limits of the voltage are applied at the inlets and outlets to investigate the flow focusing phenomena. In this experiment which is shown in Figure 5-11, the voltage V_A applied to the outlet channel was fixed at 100 V, while the voltage at the branch channel was fixed at 25 V (accordingly, $V_A > 2V_C$). From Figure 5-11, we can see that the dye solution stream is much wider than the dye solution stream which is shown in Figure 5-10 due to the decreasing of the pumping force in the horizontal channel and the pushing force in the branch channels.

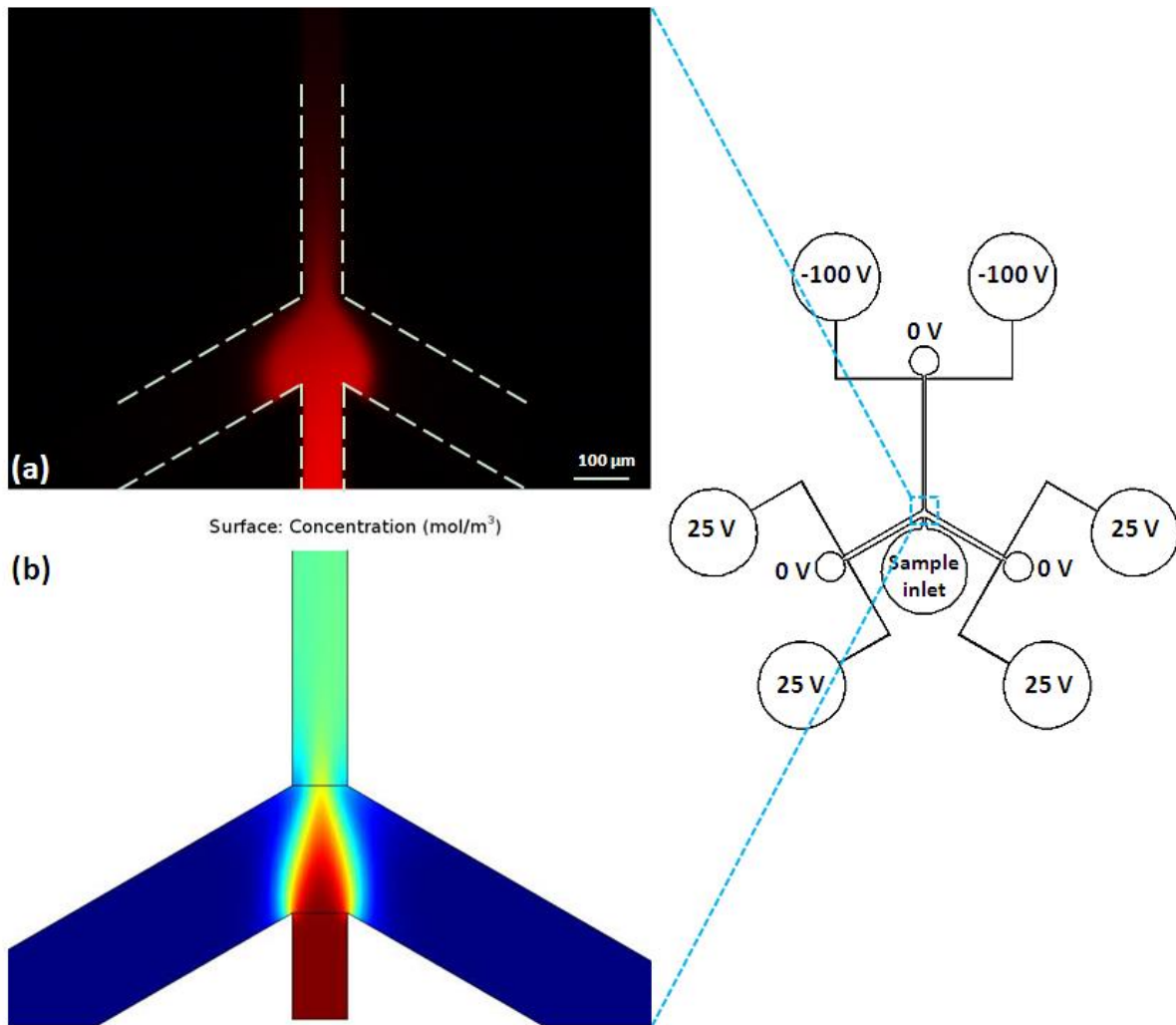


Figure 5-11 (a) A fluorescent image of flow focusing effect in the vertical microchannel. (b) A simulation image of flow focusing effect in the vertical microchannel (-100 V at A, B and 0 V at Point O; 25 V at C, D, C', D' and 0 V at Point O' and O'').

- ***Demonstration of the focusing effect of microspheres in the vertical channel***

Figure 5-12 shows the microscope images of 7 μm microspheres focused by the two sheath flows in the vertical channel. In addition, a comparison between the numerically simulated focusing process and the experimentally observed focusing process is shown in this figure. Clearly, the numerical simulation is in a good agreement with the experimental results. Figure 5-13 demonstrates the focusing effect of 7 μm diameter microspheres in the different width of vertical channel. It is obviously seen that the particle stream occupies about 1/3 of both 100 μm width of vertical channel (Figure 5-13 (a)) and 50 μm width of vertical channel (Figure 5-13 (b)) under the same voltage condition (-150 V at A, B and 0 V at Point O; 50 V at C, D, C', D' and 0 V at Point O' and O''). This result also is highly corresponding to the simulation result.

In the simulation result shown in Figure 5-8, the flow focusing effect can be improved by increasing the applied voltages at the reservoirs. In this experiment, the applied voltage at A, B is increased to 300 V and relevantly the applied voltage at C, D, C', D' is increased to 125 V, which is the same as the setup in the simulation. Obviously, as shown in Figure 5-14 (a), the particle (0.5 μm) stream is squeezed greatly by these two sheath flow, which highly agrees with the simulation result. However, when the applied voltage at C, D, C', D' is reduced to 60 V, the particle stream is much wider as shown in Figure 5-14 (b).

The flow focusing effect is determined by both the sucking force generated in the channel A-B and the pushing force generated in the channel C-D and C'-D'. The relationship between them is decided by the equation $V_A > 2V_C$. However, if the $2V_C$ is much lower than V_A , the flow focusing effect is weaker. Therefore, in the application, if we increase V_A to enhance the velocity of the particle, we must increase V_C for the best flow focusing effect.

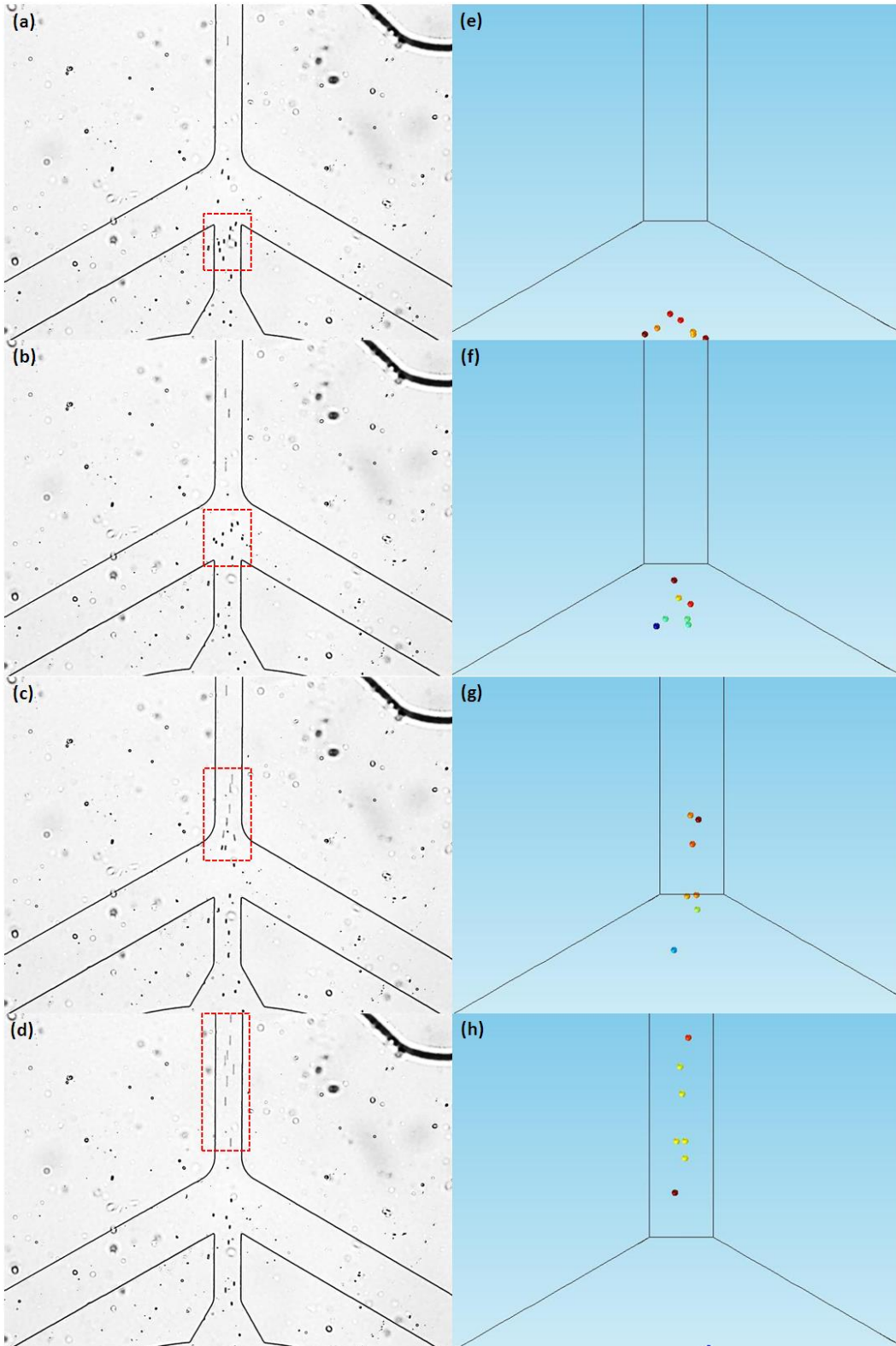


Figure 5-12 (a) - (d) A series of images of the motion of 7 μm microspheres (-150 V at A, B and 0 V at Point O; 50 V at C, D, C', D' and 0 V at Point O' and O''). (e) - (h) A series of simulation images of the motion of 7 μm microspheres (-150 V at A, B and 0 V at Point O; 50 V at C, D, C', D' and 0 V at Point O' and O'').

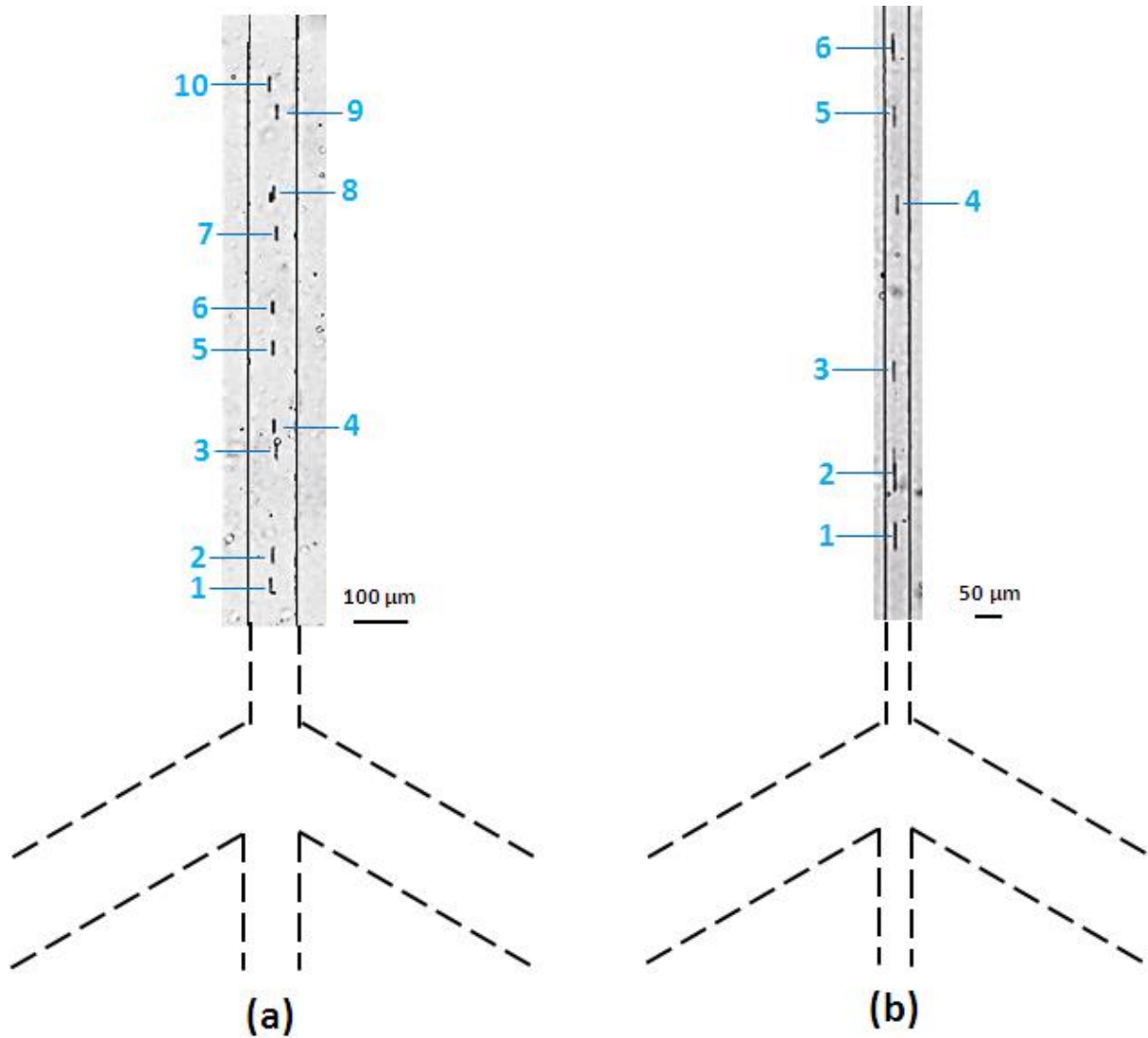


Figure 5-13 The focusing effect of 7 μm diameter microspheres in the vertical channel. (a) The width of the vertical channel is 100 μm (-150 V at A, B and 0 V at Point O; 50 V at C, D, C', D' and 0 V at Point O' and O''). (b) The width of the vertical channel is 50 μm (-150 V at A, B and 0 V at Point O; 50 V at C, D, C', D' and 0 V at Point O' and O'').

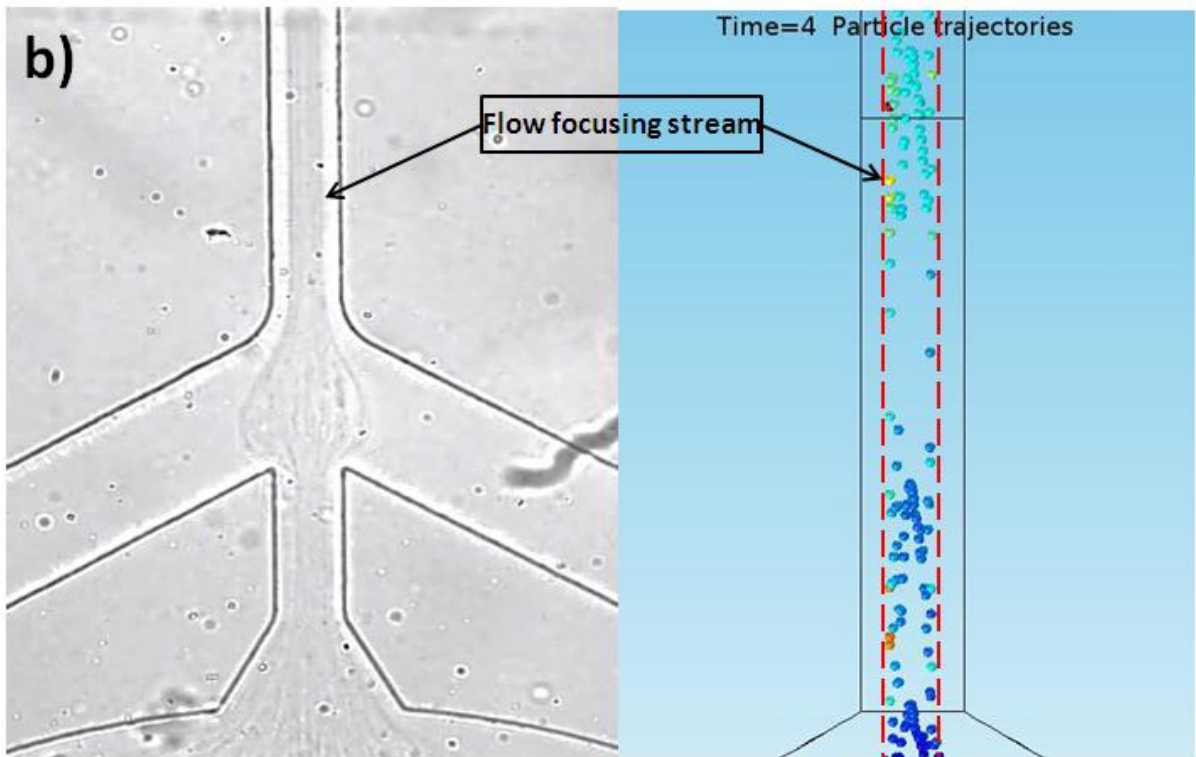
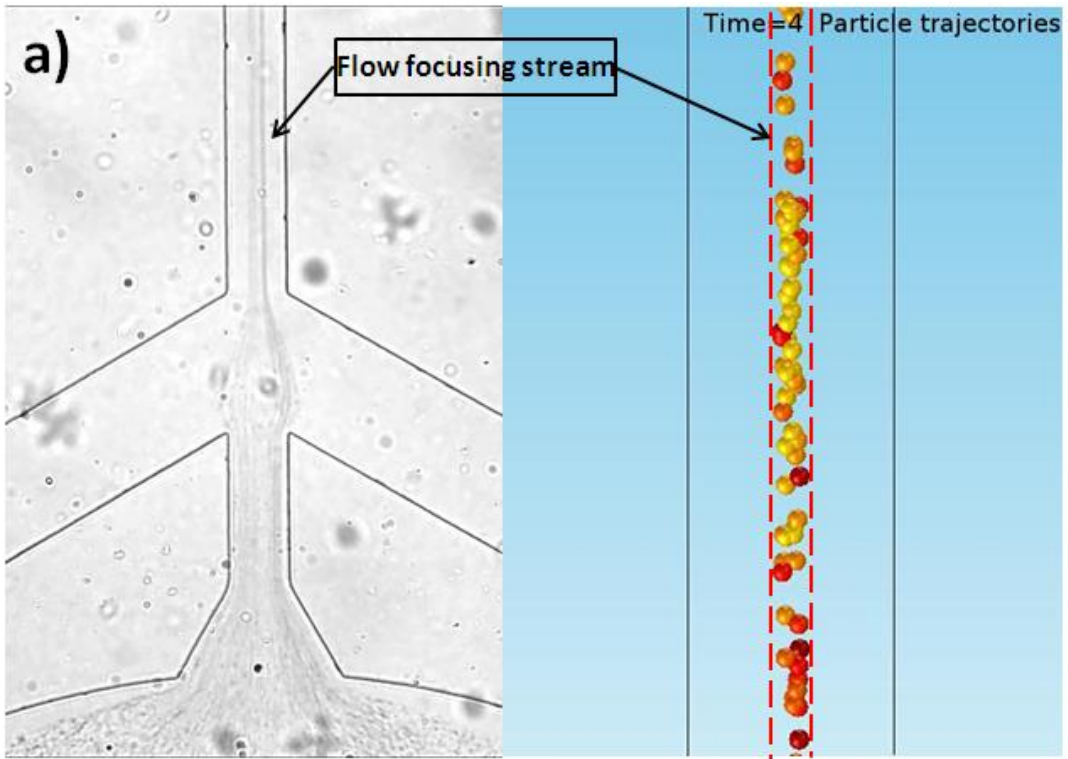


Figure 5-14 The focusing effect of 0.5 μm diameter microspheres in the vertical channel. (a) The comparison between the experimental result and the simulation result for the flow focusing effect (-300 V at A, B and 0 V at Point O; 125 V at C, D, C', D' and 0 V at Point O' and O''). (b) The comparison between the experimental result and the simulation result for the flow focusing effect (-300V at A, B and 0 V at Point O; 60 V at C, D, C', D' and 0 V at Point O' and O''). The width of the vertical channel is 100 μm .

- *The relationship between the velocity of the particle and the applied voltage at the horizontal pumping channel and the branch channels*

The motion of the particle is caused by the electrokinetic-induced pressure-driven flow. Therefore, the velocity of the particle can be controlled by the electrical field intensity. To verify this point, a series of experiments were conducted by applying different voltages at the inlets and outlets to estimate the average velocity of the particles. Figure 5-15 presents the variation of the average velocity in the vertical channel with respect to the applied electric voltages at the inlets and outlets. The electric potential at the point O, O' and O'' is kept at zero. From this figure, it is evident that the average velocity of the particle is linearly dependent on the applied voltage. By increasing the magnitude of the applied voltage, the average velocity of the particle can be increased.

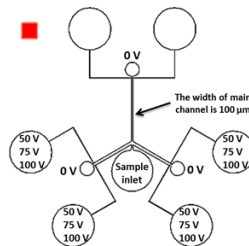
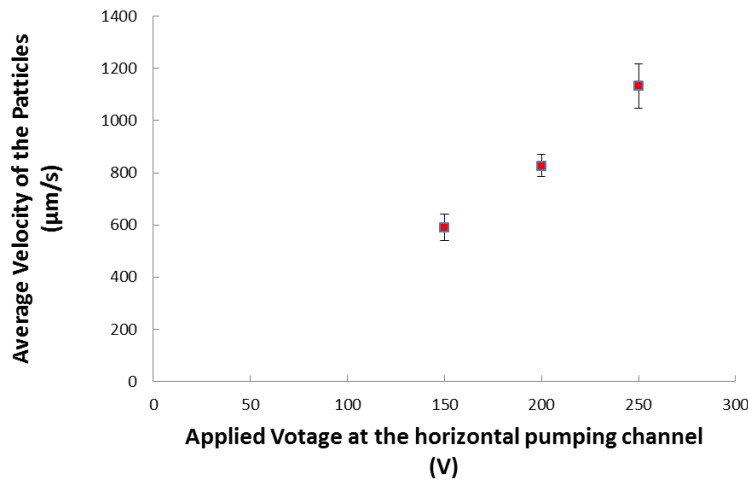


Figure 5-15 The estimation of the average velocity of the particles in the vertical channel with different applied voltages.

- *Simultaneous counting of two different fluorescent particles*

Flow focuser is a very important component in the flow cytometer. Keeping the particles/cells near the center of the channel has lots of benefits for the microfluidic flow cytometer. It can reduce the chance of channel clogging and absorption to the channel wall. It also can reduce the coincidental errors such as many particles/cells passing the interrogation area at the same moment. Besides, flow focusing can increase the speed of particle/cell in the channel, which can help to enhance the accuracy and throughput of flow cytometer. Table 5-1 displays the number of detected particles by the dual-wavelength optical detection method in the novel flow focusing microchip. Compared with the experiments mentioned in Table 4-1, the throughput of the flow focusing chip at least has a significant increasing of 50% under the same sample concentration.

Table 5-1 Comparison of the ratios of particles/cells detected by the device of this study and a commercial flow cytometer. PD stands for photo-detector. (-300 V is applied at A, B and 0 V is applied at Point O; 125 V is applied at C, D, C', D' and 0 V is applied at Point O' and O'')

		Chip1	Chip2	Chip3	Std. dev.
Exp.	PD 1, (488nm, 520nm)	88	118	126	
green/red	PD 2, (635nm, 690nm)	267	326	404	
beads	Ratio (percentage %)	32.9	36.1	31.1	2.53

5.6 Concluding remarks

In this chapter, a novel flow focusing method is demonstrated which allows for the hydrodynamic focusing in a T-shaped microchannel with two sheath flows. Sample stream and sheath flow flowing through the T-shaped microchannel are generated by the electrokinetically-induced pressure-driven flow. The sheath flow wraps the sample flow, resulting in the sample flow to be focused in the vertical channel. From the numerical simulation and experimental results, the effect of the flow focusing and the flow rate of the focusing stream can be controlled by modulating the applied voltages. Compared to other flow focusing methods, this novel approach significantly reduces the number of required components such as syringe pump, tubes and the complexity of fabrication for hydrodynamic focusing, and enables an easy integration with other microfluidic components.

Chapter 6

Conclusions and Future Work

6.1 Contributions of this thesis

This thesis dealt with the underlying concepts of the microfluidic flow cytometry system. Key contributions may be summarized as follows:

- A novel approach is firstly proposed for generating a continuous pressure-driven flow and transporting the particles or biological cells in the T-shaped microchannel by using the electrokinetically-induced pressure-driven flow method. Thus, the shortcomings of the electrokinetical force and the pressure pumping force are avoided when they are employed individually. Moreover, syringe pumps, tubing and valves for liquid handling can be avoided and it is easily to be integrated in the microfluidic device. This is one of the most important contributions of the current study.
- A novel miniaturized dual-wavelength fluorescent detection method is introduced for particle counting in microfluidic flow cytometry system. The system developed in this study can detect and count two different fluorescent particles simultaneously. The design of the two-wavelength fluorescent detection system leads to a significant reduction of the volume and the cost, in comparison with other microfluidic fluorescent detection devices reported in literature. This is the second contribution of the current study.
- Based on the electrokinetically-induced pressure-driven flow, a novel method for the flow focusing is firstly proposed and realized. This approach allows the hydrodynamic focusing in a T-shaped microchannel with two sheath flows. Compared with other flow focusing methods, this novel approach significantly reduces the number of required components such as syringe pump, tubes and the complexity of fabrication for focusing, and enables an easy integration with other microfluidic components. This is the third contribution of the current study.

6.2 Publications

- **Journal articles**

1 **Hai Jiang**, Xuan Weng, Dongqing Li. Dual-wavelength fluorescent detection of particles on a novel microfluidic chip. *Lab Chip*, 2013, 13, 843-850.

2 Xuan Weng, **Hai Jiang**, Dongqing Li. A miniaturized system for rapid and quantitative detection of Cocaine metabolite by homogeneous enzyme immunoassay. *Forensic Science International*, 2013, DOI:10.1080/10739149.2013.780251.

3 Xuan Weng, **Hai Jiang**, Dongqing Li. An electrokinetically-controlled RNA-DNA hybridization assay for foodborne pathogens detection. *Microchimica Acta*, 2012, DOI: 10.1007/s00604-012-0853-y.

4 Y. Song, J. Yang, X. Shi, **H. Jiang**, Y. Wu, R. Peng, J. Wang, N. Gong, X. Pan, Y. Sun, and D. Li, "DC dielectrophoresis separation of marine algae and particles in a microfluidic chip", *Science China – Chemistry*, 55(2012) 524-530.

5 **Hai Jiang**, Xuan Weng, Chan Hee Chon, Xudong Wu and Dongqing Li, A microfluidic chip for blood plasma separation using electro-osmotic flow (EOF) control. *Journal of Micromechanics and Microengineering*, 2011, 21 (8): 085019.

6 **Hai Jiang**, Xuan Weng and Dongqing Li, "Microfluidic Whole-blood Immunoassays", *Microfluidics and Nanofluidics*, 10 (2011) 941-964.

7 Xuan Weng, **Hai Jiang**, Junsheng Wang, Shu Chen, Honghe Cao and Dongqing Li. Automatic on-chip RNA-DNA hybridization assay with integrated phase change microvalves. *Journal of Micromechanics and Microengineering*, 2011, 22: 075003.

8 Xuan Weng, **Hai Jiang**, Chan Hee Chon, Shu Chen, Honghe Cao, Dongqing Li. An RNA-DNA Hybridization Assay Chip with Electrokinetically Controlled Oil Droplet Valves for Sequential Microfluidic Operations. *Journal of Biotechnology*, 2011, 155 (3): 330-337.

9 Xuan Weng, **Hai Jiang**, Dongqing Li. Microfluidic DNA hybridization assay. *Microfluidics and Nanofluidics*, 2011, DOI: 10.1007/s10404-011-0858-6.

10 **Hai Jiang**, Yasaman Daghighi, Chan hee Chon and Dongqing Li, "Concentration of molecules in a simple microfluidic chip", *J. Colloid Interface Sci.*, 347 (2010) 324–331.

11 Xuan Weng, Chan Hee Chon, **Hai Jiang** and Dongqing Li. Rapid detection of formaldehyde concentration in food on a polydimethylsiloxane (PDMS) microfluidic chip. *Food Chemistry*, 2009, 114: 1079–1082.

12 **Hai Jiang**, Xiaolin Zheng. System for Measuring Red Blood Cell Deformability Base on MEMS. *China Medical Device information*. 2006, 12(12): 28-31

- **Book chapter**

Hai Jiang and Dongqing Li. "Microfluidic whole-blood immunoassays", Encyclopedia of Micro- and Nanofluidics, Springer (accepted)

6.3 Suggestions for future work

From this thesis, the novel concept is found a promising way in the development of the portable microfluidic flow cytometer. The research will be continued to find out how this microfluidic system can be applied in biomedical diagnosis. More specifically, in the technological perspective, it needs to study the optimization design of the electrokinetics-based microfluidic system and make the integration design; in the application perspective, this microfluidic system could be taken as a general platform for biological detection to find out more applications for this microfluidic system. Based on the results obtained in this study, future research will be focused on the following aspects:

- 1) From the technology point of view, optimization design will be studied to improve the throughput of particle/cell the current microfluidic system. According to the current experimental result, we can count several hundred particles, which may not meet the requirement of the real application. Chip layout, flow field, electrical field, concentration field will be continuously studied to improve the performance of the microfluidic chip.
- 2) From the application point of view, the microfluidic system presented in this study must be used for the real applications. Actually, we have done some experiments for the biological cells. However, as a general platform, many other biomedical assays could be achieved by simply modifying the design of the microfluidic chip. The collaboration with the biological department or hospital is the best way for realizing the real application.

Appendix A

License Agreement for Chapter 2

This is a License Agreement between Hai Jiang ("You") and Springer ("Springer") provided by Copyright Clearance Center ("CCC"). The license consists of your order details, the terms and conditions provided by Springer, and the payment terms and conditions.

All payments must be made in full to CCC. For payment instructions, please see information listed at the bottom of this form.

License Number	3230391417601
License date	Sep 15, 2013
Licensed content publisher	Springer
Licensed content publication	Microfluids and Nanofluids
Licensed content title	Microfluidic whole-blood immunoassays
Licensed content author	Hai Jiang
Licensed content date	Jan 1, 2010
Volume number	10
Issue number	5
Type of Use	Thesis/Dissertation
Portion	Full text
Number of copies	1
Author of this Springer article	Yes and you are the sole author of the new work
Order reference number	
Title of your thesis / dissertation	Dual-wavelength Fluorescent Detection of Particles/Cells in a Novel Microfluidic Chip
Expected completion date	Nov 2013
Estimated size(pages)	130
Total	0.00 USD

License Agreement for Figure 2-1



COPYRIGHT PERMISSION LETTER

May 23, 2013

Life Technologies Corporation (LIFE) grants to:

Requesting Organization: University of Waterloo
Organization Contact: Hai Jiang (the "Requestor")
Address: Mechanical and Mechatronics Engineering
200 University Avenue West, Waterloo, ON, Canada N2L 3G1
E-mail: forestwx@gmail.com
Telephone number: 519-888-4567 ext. 35247

Authorization to use the following Copyrighted Property:

Title/description of Copyrighted Property: Introduction to Flow Cytometry Tutorial, as referenced in Exhibit A ("Copyrighted Property")

Format of the Copyrighted Property: Slide(s), Image(s), and Text.

Copyrighted Property Request Details:

Requestor would like to use the Copyrighted Property in a thesis.

Copyrighted Property location: http://probes.invitrogen.com/resources/education/tutorials/4Intro_Flow/player.html

Conditions of use:

- You may use the Copyrighted Property pursuant only to the terms set forth herein.
- You may not release and/or assign the Copyrighted Property to a third party without the written consent of LIFE.
- You must acknowledge that the Copyrighted Property is owned by Life Technologies Corporation and list the website www.lifetechnologies.com in close proximity to the Copyrighted Property (as practical). The following copyright disclaimer must accompany your use of the Copyrighted Property:


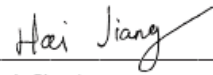
Copyright © 2013 Life Technologies Corporation. Used under permission.

Thank you for your cooperation. If you have any questions, please contact me.

Phone: 760-476-6384

Fax: 760-476-6048

Email: John.Blankenbeckler@lifetech.com

	June 6, 2013
John Blankenbeckler, Technology Transfer Senior Manager, Legal Services	Date
	June 04, 2013
Requestor's Signature	Date

License Agreement for Figure 2-2 and Figure 3-9

Dear Hai,

Thank you for your email. Please find attached a copy of the permission grant for your records.

Sample Citations:

Reproduced from Expert Review of Molecular Diagnostics, June 2011, Vol. 11, No. 5, Pages 505-519
with permission of Expert Reviews Ltd

Adapted from Expert Review of Molecular Diagnostics, June 2011, Vol. 11, No. 5, Pages 505-519
with permission of Expert Reviews Ltd

Any further queries please do not hesitate to contact me.

Many thanks,

Javonne Javonne Molloy

Publishing Administrator Future Science Group

Unitec House

2 Albert Place

Finchley Central

London

N3 1QB Tel: +44 (0)20 8371 6080

Fax: +44 (0)20 8371 6089

Email: j.molloy@futuremedicine.com

Website: www.future-science-group.com

License Agreement for Chapter 4

Dear Hai Jiang

The Royal Society of Chemistry (RSC) hereby grants permission for the use of your paper(s) specified below in the printed and microfilm version of your thesis. You may also make available the PDF version of your paper(s) that the RSC sent to the corresponding author(s) of your paper(s) upon publication of the paper(s) in the following ways: in your thesis via any website that your university may have for the deposition of theses, via your university's Intranet or via your own personal website. We are however unable to grant you permission to include the PDF version of the paper(s) on its own in your institutional repository. The Royal Society of Chemistry is a signatory to the STM Guidelines on Permissions (available on request).

Please note that if the material specified below or any part of it appears with credit or acknowledgement to a third party then you must also secure permission from that third party before reproducing that material.

Please ensure that the thesis states the following: *Reproduced by permission of The Royal Society of Chemistry* and include a link to the paper on the Royal Society of Chemistry's website. Please ensure that your co-authors are aware that you are including the paper in your thesis.

Regards

Gill Cockhead

Publishing Contracts & Copyright Executive

Dual-wavelength fluorescent detection of particles on a novel microfluidic chip

Hai Jiang, Xuan Weng and Dongqing Li

Lab Chip, 2013, 13, 843-850 DOI: 10.1039/C2LC41238A, Paper

Bibliography

- 1 A. Lehmann, S. Sørnes and A. Halstensen, *Journal of immunological methods*, 2000, 243, 229-242.
- 2 R. Nunez, *Curr. Issues Mol. Biol.*, 2001, 3, 67-70.
- 3 P. Pala, T. Hussell and P. Openshaw, *Journal of immunological methods*, 2000, 243, 107-124.
- 4 M. Roederer, J. Brenchley, M. Betts and S. De Rosa, *Clinical immunology*, 2004, 110, 199-205.
- 5 Pratip K Chattopadhyay, David A Price, Theresa F Harper, Michael R Betts, Joanne Yu, Emma Gostick, Stephen P Perfetto, Paul Goepfert, Richard A Koup, Stephen C De Rosa, Marcel P Bruchez & Mario Roederer, *Nature Medicine*, 2006, 12, 972-977.
- 6 Stephen C. De Rosa, Leonard A. Herzenberg, Leonore A. Herzenberg & Mario Roederer, *Nature Medicine*, 2001, 7, 245-248.
- 7 N. Baumgarth and M. Roederer, *Journal of immunological methods*, 2000, 243, 77-97.
- 8 Curtis D. Chin, Vincent Linder and Samuel K. Sia, *Lab Chip*, 2007, 7, 41-57.
- 9 Paul Yager, Thayne Edwards, Elain Fu, Kristen Helton, Kjell Nelson, Milton R. Tamand Bernhard H. Weigl, *Nature*, 2006, 442, 412-418.
- 10 Bernhard H. Weigl, Ron L. Bardella, Catherine R. Cabrera, *Adv. Drug Deliv. Rev.*, 2003, 55, 349–377.
- 11 Peter A. Singer, Andrew D. Taylor, Abdallah S. Daar, Ross E. G. Upshur, Jerome A. Singh, James V. Lavery, *PLoS Medicine*, 2007, 4, e265.
- 12 M. Zimmermann, E. Delamarche, M. Wolf, P. Hunziker, *Biomed. Microdevices*, 2005, 7, 99–110.
- 13 J.H. Cho, S.M. Han, E.H. Paek, I.H. Cho, S.H. Paek, *Anal. Chem.*, 2006, 78, 793–800.
- 14 H. Parsa, C.D. Chin, P. Mongkolwisetwara, B.W. Lee, J. J. Wang and S.K. Sia, *Lab Chip*, 2008, 8, 2062–2070.
- 15 P. S. Dittich, K. Tachikawa and A. Manz, *Anal. Chem.*, 2006, 78, 3887–3908.
- 16 M. Radisic, R. K. Iyer and S. K. Murthy, *Int. J. Nanomed.*, 2006, 1, 3–14.
- 17 P. S. Dittich and A. Manz, *Nature Rev. Drug Disc.*, 2006, 5, 210–218.
- 18 D. Huh, W. Gu, Y. Kamotani, J. B. Grotberg and S. Takayama, *Physiol. Meas.*, 2005, 26, R73–R98.

- 19 A. Lehmann, S. Sornes and A. Halstensen, *Journal of immunological methods*, 2000, 243, 229-242.
- 20 R. Nunez, *Current issues in molecular biology*, 2001, 3, 67-70.
- 21 P. Pala, T. Hussell and P. Openshaw, *Journal of immunological methods*, 2000, 243, 107-124.
- 22 M. Roederer, J. Brenchley, M. Betts and S. De Rosa, *Clinical immunology*, 2004, 110, 199-205.
- 23 D.A.A. Vignali, *Journal of Immunological Methods*, 2000, 243, 243–255.
- 24 P. Chattopadhyay, D. Price, T. Harper, M. Betts, J. Yu, E. Gostick, S. Perfetto, P. Goepfert, R. Koup, and S. De Rosa, *Nat. Med.*, 2006, 12, 972.
- 25 S. De Rosa, L. Herzenberg and M. Roederer, *Nat. Med.*, 2001, 7, 245.
- 26 N. Baumgarth and M. Roederer, *J. Immunol. Methods*, 2000, 243, 77.
- 27 Chin CD, Linder V and Sia SK, *Lab Chip*, 2007, 7, 41–57.
- 28 Paul Yager, Thayne Edwards, Elain Fu, Kristen Helton, Kjell Nelson, Milton R. Tam and Bernhard H. Weig, *Nat. Insight*, 2006, 442, 412–18.
- 29 Weigl BH, Bardell RL, Cabrera CR, *Adv. Drug Deliv. Rev.*, 2003, 55, 349–77.
- 30 Singer PA, Taylor AD, Daar AS, Upshur RE, Singh JA, Lavery JV, *PLoS Med.*, 2007, 4, e265.
- 31 M. Zimmermann, E. Delamarche, M. Wolf, P. Hunziker, *Biomed. Microdevices*, 2005, 7, 99–110.
- 32 J.H. Cho, S.M. Han, E.H. Paek, I.H. Cho, S.H. Paek, *Anal. Chem.*, 2006, 78, 793–800.
- 33 H. Parsa, C.D. Chin, P. Mongkolwisetwara, B.W. Lee, J.J. Wang, S.K. Sia, *Lab Chip*, 2008, 8, 2062–2070.
- 34 Scott G. Darby, Matthew R. Moore, Troy A. Friedlander, David K. Schaffer, Ron S. Reiserer, John P. Wikswa and Kevin T. Seale, *Lab Chip*, 2010, 10, 3218-3226.
- 35 Marc A. Unger, Hou-Pu Chou, Todd Thorsen, Axel Scherer and Stephen R. Quake, *Science*, 2000, 288, 113–116.
- 36 Osborn JL, Lutz B, Fu E, Kauffman P, Stevens DY and Yager P., *Lab Chip*, 2010, 10, 2659–2665.
- 37 Zimmermann M, Schmid H, Hunziker P and Delamarche E., *Lab Chip*, 2007, 7, 119–125.
- 38 Gervais L, Delamarche E., *Lab Chip*, 2009, 9, 3330–3337.

- 39 Mary Amasia and Marc Madou., *Bioanalysis*, 2010, 2, 1701-1710.
- 40 Tingjie Li, Limin Zhang, Kar Man Leung and Jun Yang, *J. Micromech. Microeng.*, 2010, 20, 105024.
- 41 Scott G. Darby, Matthew R. Moore, Troy A. Friedlander, David K. Schaffer, Ron S. Reiserer, John P. Wikswow and Kevin T. Seale, *Lab Chip*, 2010, 10, 3218–3226.
- 42 Unger MA, Chou HP, Thorsen T, Scherer A, Quake SR, *Science*, 2000, 288, 113–116.
- 43 Damien Robert, Nicole Pamme, H  ne Conjeaud, Florence Gazeau, Alexander Iles and Claire Wilhelm, *Lab Chip*, 2011, 11, 1902.
- 44 Joo S, Kim KH, Kim HC, Chung TD, *Biosensors and Bioelectronics*, 2010, 25, 1509–1515.
- 45 Werner M, Merenda F, Piguet J, Salath   RP, Vogel H, *Lab Chip*, 2011, 11, 2432.
- 46 Hu G., Gao Y., Li D., *Biosensors and Bioelectronics*, 2007, 22, 1403-1409.
- 47 Xiang Q., Hu G., Gao Y., Li D., *Biosensors and Bioelectronics*, 2006, 21, 2006-2009.
- 48 Gao Y., Hu G., Frank Y.H. Lin, Li D., *Biomedical Microdevices*, 2005, 7, 301-312.
- 49 Minerick A R, Ostafin A E and Chang H C, *Electrophoresis*, 2002, 23, 2165–2173.
- 50 Katherine A. DeBruin and Wanda Krassowska, *Biophysical Journal*, 1999, 77, 1213-1224.
- 51 Howell PB, Golden JP, Hilliard LR, Erickson JS, Mott DR, Ligler FS, *Lab Chip*, 2008, 8, 1097–1103.
- 52 Abel L. Thangawng, Jason S. Kim, Joel P. Golden, George P. Anderson, Kelly L. Robertson, Vyechi Low, Frances S. Ligler, *Anal. Bioanal. Chem.*, 2010, 398, 1871–1881.
- 53 Berger A, Talbot L, Yao LS, *Annu. Rev. Fluid Mech.*, 1983, 15, 461–512.
- 54 Lee MG, Choi S, Park JK, *Lab Chip*, 2009, 9, 3155–3160.
- 55 Xuan X, Li D, *Electrophoresis*, 2005, 26, 3552–3560.
- 56 Shi J, Mao X, Ahmed D, Colletti A, Huang TJ, *Lab Chip*, 2008, 8, 221–223.
- 57 G.R. Goddard, C.K. Sanders, J.C. Martin, G. Kaduchak and S.W. Graves, *Anal. Chem.*, 2007, 79, 8740–8746.
- 58 Di Carlo D, *Lab Chip*, 2009, 9, 3038–3046.

- 59 Chu H, Doh I, Cho Y, *Lab Chip*, 2009, 9, 686–691.
- 60 N. Demierre, T. Braschler, R. Muller and P. Renaud, *Sensors and Actuators B*, 2008, 132, 388–396.
- 61 Ekins RP, *Clin. Chim. Acta.*, 1960, 5, 453–459.
- 62 Miles LEM, Hales CN, *Nature*, 1968, 219, 186–189.
- 63 Engvall E, Perlmann P, *Immunochemistry*, 1971, 8, 871–874.
- 64 Van Weemen BK, Schuurs AH, *FEBS Lett.*, 1971, 15, 232–236.
- 65 Engvall E, *Med, Biol.*, 1977, 55, 193–200.
- 66 Marjatta Uotila, Erkki Ruoslahti and Eva Engvall, *Journal of Immunological Methods*, 1981, 42, 11–15.
- 67 Pereira SV, Messina GA and Raba J, *J Chromatogr B Analyt Technol Biomed Life Sci.*, 2010, 878, 253–257.
- 68 Kong J, Jiang L, Su X, Qin J, Du Y and Lin B, *Lab Chip*, 2009, 9, 1541–1547.
- 69 Herr AE, Hatch AV, Giannobile WV, Throckmorton DJ, Tran HM, Brennan JS and Singh AK, *Ann. N.Y. Acad. Sci.*, 2007, 1098, 362–374.
- 70 Herr AE, Hatch AV, Throckmorton DJ, Tran HM, Brennan JS, Giannobile WV and Singh AK, *Proc Natl Acad Sci U S A.*, 2007, 13, 5268–5273.
- 71 Kakehi K, Oda Y and Kinoshita M, *Anal. Biochem.*, 2001, 297, 111–116.
- 72 V.K. Yadavalli and M.V. Pishko, *Anal. Chim. Acta.*, 2004, 507, 123–128.
- 73 Tomoya Tachi, Noritada Kaji, Manabu Tokeshi and Yoshinobu Baba, *Lab Chip*, 2009, 9, 966–971.
- 74 Yang YN, Lin HI, Wang JH, Shiesh SC and Lee GB, *Biosensors and Bioelectronics*, 2009, 24, 3091–3096.
- 75 Xuhua Wang, cAuthor Vitae, Maliwan Amatongchaib, dAuthor Vitae, Duangjai NacaprichaeAuthor Vitae, Oliver Hofmannb, cAuthor Vitae, John C. de Mellob, cAuthor Vitae, Donal D.C. Bradleya, cAuthor Vitae and Andrew J. de Mello, *Sensors and Actuators B: Chemical*, 2009, 140, 643–648.

- 76 Xuhua Wang, Oliver Hofmann, Rupa Das, Edward M. Barrett, Andrew J. deMello, John C. deMello and Donal D. C. Bradley, *Lab Chip*, 2007, 7, 58–63.
- 77 Hui Huang, Zheng XL, Zheng JS, Pan J and Pu XY, *Biomed Microdevices*, 2009, 11, 213–216.
- 78 Kenji Uchiyama, Akihida Hibara, Hiroko Kimura, Tsuguo Sawada and Takehiko Kitamori, *Jpn. J. Appl. Phys.*, 2000, 39, 5316–5322.
- 79 Takehita Kitamori, Manabu Tokeshi, Akihida Hibara and Kiichi Sato, *Anal. Chem.*, 2004, 76, 52 A–60 A.
- 80 Henares, T. G., Funano, S. I., Terabe, S., Mizutani, F., Sekizawa, R. and Hisamoto, H., *Anal. Chim. Acta* 2007, 589, 173–179.
- 81 Ihara M, Yoshikawa A, Wu Y, Takahashi H, Mawatari K, Shimura K, Sato K, Kitamori T and Ueda H, *Lab Chip*, 2010, 10, 92–100.
- 82 E. Kretschmann, *Z. Phys.*, 1971,241, p. 313.
- 83 Shankaran D R, Gobi K V and Miura N., *Sensors Actuators B*, 2007, 121, 58–77.
- 84 Lippa P B, Sokoll L J and Chan D W., *Clin. Chim. Acta*, 2001, 314, 1–26.
- 85 Cooper M A., *Nature Rev.*, 2002, 1, 515–528.
- 86 Karlsson R., *J. Mol. Recognit.*, 2004,17, 151–161.
- 87 Mullett W M, Lai E P C and Yeung J M., *Methods*, 2000, 22, 77–91.
- 88 Nilsson CE, Abbas S, Bennemo M, Larsson A, Hämäläinen MD and Frostell-Karlsson A, *Vaccine*, 2010,28, 759–766.
- 89 Lee, K. H., Su, Y. D., Chen, S. J., Tseng, F. G. and Lee, G. B., *Biosens. Bioelectron.*, 2007, 23, 466–472.
- 90 Changchun Liu, Dafu Cui, HuiLi, *Biosensors and Bioelectronics*, 2010, 26, 255–261.
- 91 Krishnamoorthy G, Carlen ET, Kohlheyer D, Schasfoort RBM, van den Berg A., *Anal. Chem.*, 2009, 81, 1957–1963.
- 92 Ganeshram Krishnamoorthy, Edwin T. Carlen , Hans L. deBoer , Albert van den Berg and Richard B. M. Schasfoort, *Anal. Chem.*, 2010, 82, 4145–4150.
- 93 Dhesingh Ravi Shankaran, Norio Miura, *J. Phys. D: Appl. Phys.*, 2007, 40, 7187–7200.

- 94 Wanida Laiwattanapaisal, Tamsiri Songjaroen, Thitima Maturros, Tanom Lomas, Assawapong Sappat and Adisorn Tuantranont, *Sensors*, 2009, 9, 10066-10079.
- 95 J. Bard and L. R. Faulkner, *2nd ed. New York: Wiley*, 2001.
- 96 Yoo SJ, Choi YB, Ju JI, Tae GS, Kim HH, Lee SH, *Analyst*, 2009, 134, 2462–2467.
- 97 I-Jane Chen and Erno Lindner, *Anal. Chem.*, 2009, 81, 9955–9960.
- 98 Liu CY, Rick J, Chou TC, Lee HH, Lee GB, *Biomed Microdevices*, 2009, 11, 201–211.
- 99 Karin Y. Chumbimuni-Torres, Zong Dai, Nastassia Rubinova, Yun Xiang, Ern ö Pretsch, Joseph Wang, and Eric Bakker, *J. AM. CHEM. SOC.*, 2006, 128, 13676-13677.
- 100 Zarini Muhammad-Tahir, Evangelyn C. Alocilja, *Biosensors and Bioelectronics*, 2003, 18, 813-819.
- 101 Hongming Liua, Yadong Yangb, Ping Chena and Zhaoyang Zhong, *Biochemical Engineering Journal*, 2009, 45, 107–112.
- 102 Ke-Zhong Liang, Jun-Sheng Qi, Wei-Jun, Mu and Zheng-Xue Liu, *Bioprocess Biosyst Eng.*, 2009, 32, 353–359.
- 103 M. Hnaieina, W.M. Hassena, A. Abdelghanib, C. Fournier-Wirthc, J. Costec, F. Bessueillea, D. Leonarda, N. Jaffrezic-Renault, *Electrochemistry Communications*, 2008, 10, 1152–1154.
- 104 Madhukar Varshney, Yanbin Li, Balaji Srinivasan and Steve Tung, *Sensors and Actuators B*, 2007, 128, 99–107.
- 105 Chia-Hsien Yeh, Wei-Ting Chen, Hong-Ping Lin, Tsung-Chain Chang and Yu-Cheng Lin, *Sensors and Actuators B*, 2009, 139, 387–393.
- 106 Kuei-Ling Su, Hao-Hsuan Huang, Tsung Chain Chang, Hong-Ping Lin, Yu-Cheng Lin and Wei-Ting Chen, *Microfluid Nanofluid*, 2009, 6, 93–98.
- 107 Vasile Mihai Mecea, *Analytical Letters*, 2005, 38, 753–767.
- 108 Monika Michalzik, Ralph Wilke, Stephanus B üttgenbach, *Sens. Actuators B Chem.*, 2005, 111-112(11), 410-415.
- 109 J. Rabe, S. B üttgenbach, B. Zimmermann, P. Hauptmann, *IEEE/EIA International Frequency Control Symposium*, 2000, pp. 106–112.

- 110 Thomas Frisk, Niklas Sandström, Lars Eng, Wouter van der Wijngaart, Per Månsson and Göran Stemmea, *Lab Chip*, 2008, 8, 1648–1657.
- 111 Namsoo Kim, Dong-Kyung Kim, Yong-Jin Cho, *Sensors and Actuators B*, 2009, 143, 444–448.
- 112 Yıldız Uludağ, Ibtisam E. Tothill, *Talanta*, 2010, 82, 277–282.
- 113 J. Seo and L. P. Lee, *IEEE Transducers, Solid-State Sensors, Actuators and Microsystems*, 2003, pp. 1136–1139, 2003.
- 114 J. Seo and L. P. Lee, *Sensors and Actuators B: Chemical*, 2004, 99, 615–622.
- 115 J. A. Chediak, Z. Luo, J. Seo, N. Cheung, L. P. Lee and T. D. Sands, *Sensors and Actuators A: Physical*, 2004, 111, 1–7.
- 116 A. Pais, A. Banerjee, D. Klotzkin and I. Papautsky, *Lab Chip*, 2008, 8, 794–800.
- 117 O. Schmidt, M. Bassler, P. Kiesel, C. Knollenberg and N. Johnson, *Lab Chip*, 2007, 7, 626–629.
- 118 T. M. Chinowsky, M. S. Grow, K. S. Johnston, K. Nelson, T. Edwards, E. Fu and P. Yager, *Biosensors and Bioelectronics*, 2007, 22, 2208–2215.
- 119 E. Fu, T. Chinowsky, K. Nelson, K. Johnston, T. Edwards, K. Helton, M. Grow, J. Miller and P. Yager, *Ann. N. Y. Acad. Sci.*, 2007, 1098, 335–344.
- 120 T. M. Chinowsky, S. D. Soelberg, P. Baker, N. R. Swanson, P. Kauffman, A. Mactutis, M. S. Grow, R. Atmar, S. S. Yee and C. E. Furlong, *Biosensors and Bioelectronics*, 2007, 22, 2268–2275.
- 121 B. Feltis, B. Sexton, F. Glenn, M. Best, M. Wilkins and T. Davis, *Bioelectronics*, 2008, 23, 1131–1136.
- 122 J. Hea, W. Zhong, A. Tang, X. Yan, C. Lewis, V. Majidi and W. Hang, *Talanta*, 2007, 71, 2126–2128.
- 123 J. E. Knittle, D. Roach, P. B. V. Horn and K. O. Voss, *Anal. Chem.*, 2007, 79, 9478–9483.
- 124 C. Luo, Q. Fu, H. Li, L. Xu, M. Sun, Q. Ouyang, Y. Chen and H. Ji, *Lab Chip*, 2005, 5, 726–729.
- 125 Segyeong Joo, Kee Hyun Kim, Hee Chan Kim and Taek Dong Chung, *Biosensors and Bioelectronics*, 2010, 25, 1509–1515.
- 126 Joerg Martini, Michael I. Recht, Malte Huck, Marshall Bern, Noble Johnson and Peter Kiesel, *Lab Chip*, 2012, Accepted Manuscript.

- 127 Xiaole Mao, Ahmad Ahsan Nawaz, Sz-Chin Steven Lin, Michael Ian Lapsley, Yanhui Zhao, J. Philip McCoy, Wafik S. El-Deiry, and Tony Jun Huang, *Biomicrofluidics*, 2012, 6, 024113.
- 128 Yuejun Kanga, Xudong Wub, Yao-Nan Wangc, Dongqing Li, *analytica chimica acta*, 2008, 626, 97-103.
- 129 Cheng Frank Zhong, Jing Yong Ye, Andrzej Myc, Thommey Thomas, Anna Bielinska, James R. Baker, Jr. and Theodore B. Norris, *Proc. of SPIE*, 2004, 5700, 78-89.
- 130 Lingling Yang, Lina Wu, Shaobin Zhu, Yao Long, Wei Hang, and Xiaomei Yan, *Anal. Chem.*, 2010, 82, 1109–1116.
- 131 Yi-Chung Tung, Min Zhang, Chih-Ting Lin, Katsuo Kurabayashi, Steven J. Skerlos, *Sensors and Actuators B*, 2004, 98, 356–367.
- 132 Joel P. Golden, Jason S. Kim, Jeffrey S. Erickson, Lisa R. Hilliard, Peter B. Howell, George P. Anderson, Mansoor Nasir and Frances S. Ligler, *Lab Chip*, 2009, 9, 1942–1950.
- 133 Ganassin, R.C., Bols, N.C., *Fish Shellfish Immunol.*, 1998, 8, 457–476.
- 134 Rojas V, Galanti N, Bols NC, Jiménez V, Paredes R, Marshall SH, *J Cell Biochem.*, 2010, 110, 468-476.
- 135 D. P. Schrum, C. T. Culbertson, S. C. Jacobson and J. M. Ramsey, *Anal. Chem.*, 1999, 71, 4173–4177.
- 136 G.-B. Lee, C.-H. Lin and S.-C. Chang, *J. Micromech. Microeng.*, 2005, 15, 447–454.
- 76 J. Shi, X. Mao, D. Ahmed, A. Colletti and T. J. Huang, *Lab Chip*, 2008, 8, 221–223.
- 137 X. Mao, J. R. Waldeisen and T. J. Huang, *Lab Chip*, 2009, 9, 1583–1589.
- 138 S. Choi, S. Song, C. Choi and J.-K. Park, *Small*, 2008, 4, 634–641.
- 139 S. Choi and J.-K. Park, *Anal. Chem.*, 2008, 80, 3035–3039.
- 140 Reyes, D. R., Iossifidis, D., Aurous, P., Manz, A., *Anal. Chem.*, 2002, 74, 2623–2636.
- 141 Stone, H. A., Kim, S., *AIChE J.*, 2001, 47, 1250–1254.
- 142 Vilkner, T., Janasek, D., Manz, A., *Anal. Chem.*, 2004, 76, 2273–2285.
- 143 Stone, H. A., Stroock, A. D., Ajdari, A., *Annu. Rev. Fluid. Mech.*, 2004, 36, 381–411.

- 144 Verpoorte, E., *Lab Chip*, 2003, 3, 60N–68N.
- 145 Yamada, M., Nakashima, M., Seki, M., *Anal. Chem.*, 2004, 76, 5465–5471.
- 146 Jacobson, S. C., Culberston, C. T., Daler, J. E., Ramsey, J. M., *Anal. Chem.*, 1998, 70, 3476–3480.
- 147 Plenert, M. L., Shear, J. B., *Proc. Natl. Acad. Sci. USA*, 2003, 100, 3853–3857.
- 148 Chou, H., Spence, C., Scherer, A., Quake, S., *Proc. Natl. Acad. Sci. USA*, 1999, 96, 11–13.
- 149 Fu, Y., Spence, C., Scherer, A., Arnold, F. H., Quake, S. R., *Nature Biotech.*, 1999, 17, 1109–1111.
- 150 Lee, G., Lin, C., Chang, G., *Sens. Actuators A*, 2003, 103, 165–170.
- 151 Blankenstein, G., Larsen, U. D., *Biosens. Bioelectron.*, 1998, 13, 427–438.
- 152 Pabit, S. A., Hagen, S. J., *Biophys. J.*, 2002, 83, 2872–2878.
- 153 Wang, M. M., Tu, E., Raymond, D. E., Yang, J. M., et al., *Nature Biotech.*, 2005, 23, 83–87.
- 154 Wolff, A., Perch-Nielsen, I. R., Larsen, U. D., Friis, P., et al, *Lab Chip*, 2003, 3, 22–27.
- 155 Knight, J. B., Vishwanath, A., Brody, J. P., Austin, R. H., *Phys. Rev. Lett.*, 1998, 80, 3863–3866.
- 156 Jacobson, S. C., Ramsey, J. M., *Anal. Chem.*, 1997, 69, 3212–3217.
- 157 Schrum, D. P., Culbertson, C. T., Jacobson, S. C., Ramsey, J. M., *Anal. Chem.*, 1999, 71, 4173–4177.
- 158 McClain, M. A., Culbertson, C. T., Jacobson, S. C., Ramsey, J. M., *Anal. Chem.*, 2001, 73, 5334–5338.
- 159 Dittrich, P. S., Schwille, P., *Anal. Chem.*, 2003, 75, 5767–5774.
- 160 Fu, L., Yang, R., Lee, G., *Anal. Chem.*, 2003, 75, 1905–1910.
- 161 Fu, L., Yang, R., Lin, C., Pan, Y., Lee, G., *Anal. Chem.*, 2004, 507, 163–169.
- 162 Xiangchun Xuan and Dongqing Li, *Electrophoresis*, 2005, 26, 3552–3560.
- 163 Ackerson BJ, *Phys A*, 1991, 174, 15–30.
- 164 <http://www.columbia.edu/cu/biology/courses/w3150/lecture2.pdf>